Search for Low-Mass Dark Matter with the CRESST-II Experiment

Dissertation

der Mathematisch-Naturwissenschaftlichen Fakultät
der Eberhard Karls Universität Tübingen
zur Erlangung des Grades eines
Doktors der Naturwissenschaften
(Dr. rer. nat.)

vorgelegt von
Dipl.-Phys. Christian Strandhagen
aus Heilbronn

Tübingen
2016

Gedruckt mit Genehmigung der Mathematisch-Naturwissenschaftlichen
Fakultät der Eberhard Karls Universität Tübingen.

Tag der mündlichen Qualifikation:	09. 12. 2016
Dekan:	Prof. Dr. Wolfgang Rosenstiel
1. Berichterstatter:	Prof. Dr. Josef Jochum
2. Berichterstatter:	Prof. Dr. Tobias Lachenmaier

Zusammenfassung

Zahlreiche astrophysikalische Beobachtungen legen nahe, dass der größte Teil der Materie im Universum in Form von Dunkler Materie vorliegt. Die zugrunde liegende Natur dieser Dunklen Materie bleibt jedoch eines der bedeutenden ungelösten Rätsel der Physik unserer Zeit. Eine Hypothese ist die Existenz schwach wechselwirkender, massiver Teilchen (WIMPs, weakly interacting massive particles). Das CRESST Experiment zielt auf den Nachweis solcher Teilchen ab. Es setzt Tieftemperaturdetektoren ein um nach Kernrückstößen zu suchen, die durch elastische Streuung dieser Dunkle-Materie-Teilchen an den Atomkernen, aus denen der Detektor besteht, hervorgerufen werden. Diese Detektoren sind in der Lage sehr niedrige Rückstoßenergien nachzuweisen ($\lesssim 1\,\mathrm{keV}$). Dadurch sind sie besonders geeignet um nach leichten Dunkle-Materie-Teilchen zu suchen ($\lesssim 5\,\mathrm{GeV}/c^2$), die für andere Experimente mit höheren Energieschwellen nicht nachweisbar sind.

Im Rahmen dieser Arbeit werden Daten analysiert, die zwischen Juli 2013 und August 2015 vom CRESST Experiment aufgezeichnet wurden. Der Schwerpunkt hierbei liegt insbesondere auf leichten Dunkle-Materie-Teilchen. Dies bedarf neuartiger Methoden Untergrundereignisse bei niedrigen Energien zu entfernen. Eine solche Methode, die Untergrundereignisse aufgrund ihrer Pulsform mittels Techniken des Maschinellen Lernens identifiziert, wird vorgeführt. Als Ergebnis konnten Obergrenzen für den spin-unabhängigen Wirkungsquerschnitt von Dunkler Materie mit Nukleonen ermittelt werden, die den Parameterbereich, der von direkten Suchen nach Dunkler Materie abgedeckt wird, auf Massen unterhalb $1\,\mathrm{GeV}/c^2$ erweitern. Zusätzlich konnten Modelle Asymmetrischer Dunkler Materie mit impulsabhängigen Kopplungen eingegrenzt werden. Abschließend wird der Einfluss verschiedener Detektorparameter auf die Sensitivität künftiger Erweiterungen des CRESST Experiments untersucht.

Dunkle Materie, WIMP, Astroteilchen Physik

Abstract

There is plenty of evidence from various astrophysical observations suggesting that most of the matter in the universe comes in the form of dark matter. Yet the underlying nature of this dark matter remains one of the important unsolved puzzles in physics today. One hypothesis is the existence of weakly interacting massive particles (WIMPs). The CRESST experiment aims at the detection of such particles. It employs cryogenic particle detectors to search for nuclear recoils induced by the elastic scattering of those dark matter particles off the nuclei composing the detectors. These detectors are able to detect very low recoil energies ($\lesssim 1\,\mathrm{keV}$), which makes them especially suited to search for light dark matter particles ($\lesssim 5\,\mathrm{GeV}/c^2$) not accessible to other experiments with higher energy thresholds.

In this work, data taken with the CRESST experiment between July 2013 and August 2015 are analyzed, focusing in particular on light dark matter particles. This requires novel methods to reject backgrounds at low energies. One such method which identifies background events based on their pulse shape using machine learning techniques is presented. As a result, limits could be set on the spin-independent dark matter-nucleon cross section extending the parameter space covered by direct detection searches to masses below $1\,\mathrm{GeV}/c^2$. Additionally, momentum-dependent asymmetric dark matter models could be constrained. Finally, the influence of various detector parameters on the sensitivity of future upgrades to the CRESST experiment is investigated.

dark matter, WIMP, astroparticle physics

Contents

Chapter 1

Dark Matter

1.1 Observational Evidence

First evidence for the existence of large amounts of non-luminous matter in the universe stems already from the 1930s. In 1932, Jan Hendrik Oort studied the motion of stars perpendicular to the local galactic plane. The mass of the galactic plane he inferred with his method exceeded the value obtained by previous observations [1]. One year later, Fritz Zwicky used the virial theorem to estimate the mass of the Coma cluster of galaxies. He claimed that the total mass of the cluster exceeds the luminous mass by a factor of 400 and attributed the missing mass to what he called *dark matter* [2].

In the 1960s, studies of the radial velocities of stars in spiral galaxies by Vera Rubin showed that the observed velocities remain almost constant when going to the outer parts of the galactic disc, whereas one would expect the velocities to decrease due to the decreasing mass density of the luminous matter. These observations again showed the need for additional non-luminous or dark matter [3]. Fig. 1.1 shows an example of a measured rotation curve which illustrates the necessity of an additional dark matter halo [4].

Today, the existence of dark matter is generally accepted and supported by a multitude of observations. In addition to the evidence due to the dynamics of galaxies and galaxy clusters, as mentioned above, the observation of the cosmic microwave background (CMB) and the study of large scale structure in the universe lead to the precise determination of the dark matter density in the universe.

The CMB radiation we can observe today was created ~ 400.000 years after the big bang. Before that time, the universe was a hot and dense plasma, where matter and radiation were in thermal equilibrium. Around that time, the universe had cooled enough through expansion (to about 3000 K) that electrons and protons recombined to neutral hydrogen, thus making the universe

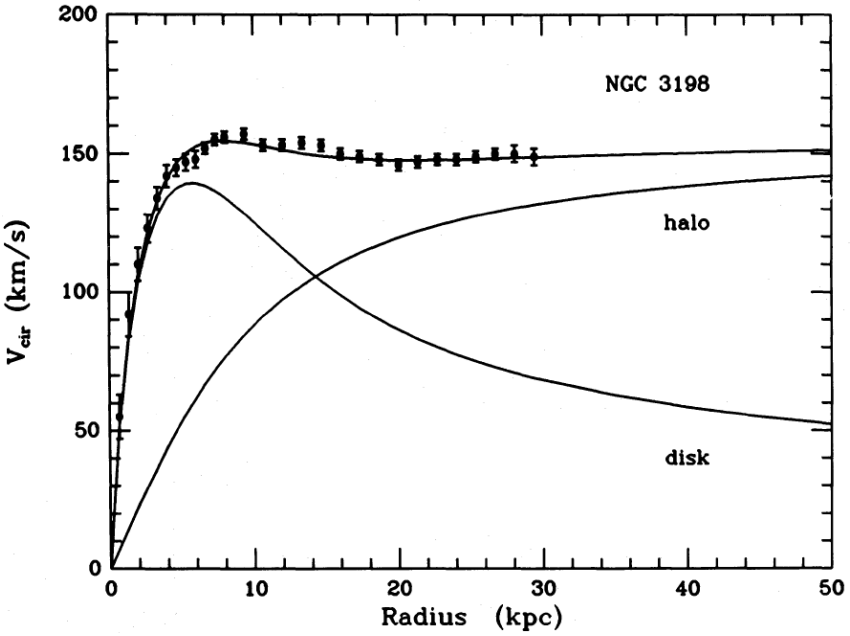

Figure 1.1: Rotation curve (dots with error bars) of NGC 3198 together with fitted model (black curve passing through data points) consisting of a contribution from normal matter (disk) and a dark matter halo. The rotation curve is based on the measurement of the circular velocity v_{cir} of the hydrogen disk at different radii. Taken from [4].

transparent to photons. These photons should accordingly follow a black body spectrum with a temperature of 3000 K. The expansion of the universe leads to a red shift of these photons of $z \approx 1100$, lowering the temperature of the CMB to 2.7 K today. Although the earliest predictions of such a background radiation already appeared in the 1930s and 1940s [5, 6], the first observation in 1964 by Penzias and Wilson came as an accident during the test of a new microwave antenna [7].

Most of the information relevant to cosmology is encoded in the tiny fluctuations of the temperatures which are of the $\mathcal{O}(10^{-4}\,\mathrm{K})$.[1] The most precise measurement of the CMB today comes from the Planck satellite [9, 10] and is usually presented as an all sky map which visualizes these temperature fluctuations (see Fig. 1.2). The angular correlations of these fluctuations can be decomposed into spherical harmonics and displayed as an angular power spectrum (see Fig. 1.3). From this, one can tell that the dominant angular scale of the CMB anisotropies is $\sim 1\,^\circ$.

The peaks in the power spectrum originate from acoustic oscillations in the primordial plasma, where radiation pressure acts as the restoring force. Odd

[1] For an in-depth review of the physics related to the CMB see [8].

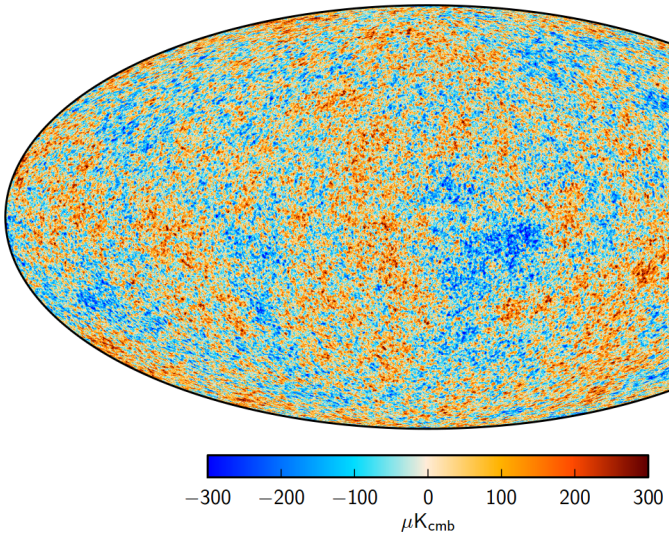

Figure 1.2: Full sky map of the CMB intensity fluctuations as published by the Planck collaboration [10].

numbered peaks correspond to compressions of the photon-baryon fluid, even numbered peaks to rarefactions. Adding baryons to the plasma enhances the compression peaks, which makes the relative heights of the first and second peak sensitive to the baryon density. Higher order peaks are sensitive to the ratio of radiation to total matter in the early universe since they originate from the early, radiation dominated era. The time at which the universe became matter dominated obviously depends on the matter density and affects the shape of the CMB power spectrum. Notably, an increased height of the third peak corresponds to a large matter density. Since the baryon density is fixed independently, the enhancement of the third peak in the power spectrum yields a precise measurement of the dark matter density at the time of recombination [11].

The density fluctuations which cause the CMB anisotropies are considered the seeds for large scale structure formation in the universe. Large N-body simulations have been performed which trace the evolution of the dark matter in the universe originating from these seeds [12, 13, 14]. The results of these simulations agree remarkably well with the large scale structure observed in large sky surveys such as SDSS [15] or the Lyman-α forest [16] if one assumes non-relativistic or cold dark matter. In the cold dark matter scenario the baryons follow the dark matter, which clusters much earlier than ordinary matter since it feels no force opposing gravitation. Structure formation thus happens in a hierarchical fashion, where smaller structures form first and then aggregate into larger ones, until the structure consisting of filaments and voids we can observe today is formed.

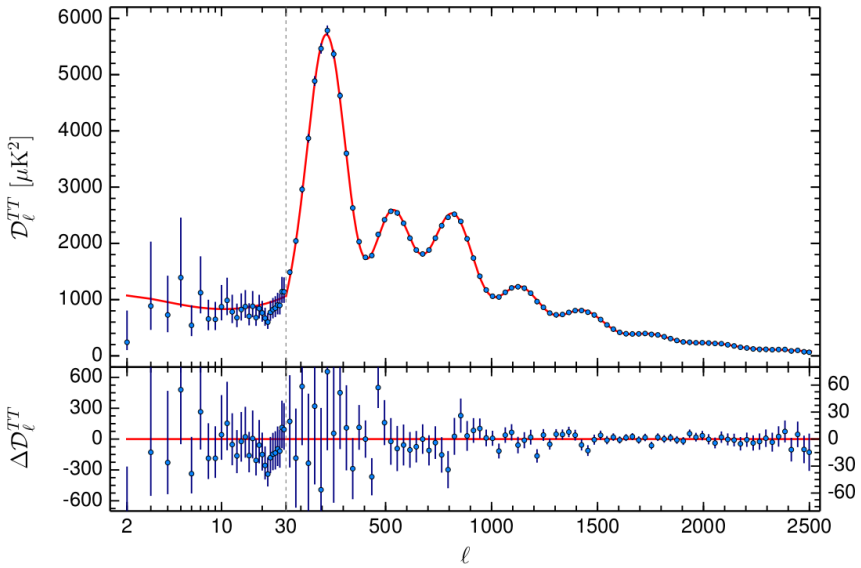

Figure 1.3: The Planck 2015 temperature power spectrum. Shown in blue are the data points together with the 1σ error bars, the red line corresponds to the best fit ΛCDM model. The bottom panel shows the residuals with respect to this model. Figure taken from [9].

The other extreme case is the so-called hot dark matter, which means the dark matter is composed of highly relativistic particles. Hot dark matter prevents the formation of small scale structures since the large kinetic energy of the dark matter particles prevents clustering in the early universe. Since this is in disagreement with observations, it is ruled out that hot dark matter contributes significantly to the dark matter density in the universe. This is an important result, because the only standard model particles which act as dark matter are neutrinos which, due to their tiny masses, belong to the hot dark matter, thus requiring new physics beyond the standard model to explain the nature of dark matter.

These astrophysical observations, among others, have led to the so-called ΛCDM model, which today is considered the standard model of cosmology. With only six independent parameters it can explain the expansion history of the universe, the CMB measurements and is in general agreement with all the cosmological data. The Λ in ΛCDM represents the cosmological constant or dark energy, which is needed to explain the accelerated expansion of the universe as inferred from surveys of distant supernovae of type Ia [17, 18]. CDM on the other hand stands for cold dark matter. One of the main results of the ΛCDM model is the composition of the universe with 68.3 % dark energy, 4.9 % baryonic matter and 26.8 % dark matter (based on the most recent data from Planck [9]).

1.2 Dark Matter Models

Among the most popular dark matter particle candidates is the so-called weakly interacting massive particle (WIMP). Its appeal arises mainly from the fact that a particle with an annihilation cross section comparable to that of the weak interaction which is thermally produced in the early universe naturally reproduces the dark matter relic density. This coincidence is often referred to as the *WIMP miracle*. In addition, there are well motivated WIMP candidates from extensions to the standard model of particle physics (SM) like e.g. supersymmetry (SUSY). SUSY tries to solve the hierarchy problem in the SM by relating each bosonic particle with a fermionic one and vice versa. This introduces a so-called superpartner for each SM particle, doubling the number of particles. To guarantee baryon and lepton number conservation also in SUSY, a conserved quantum number, the so-called R-parity, has to be introduced which is +1 for SM particles and -1 for SUSY particles. The conservation of R-parity prevents the lightest SUSY particle (LSP) from decaying into SM particles, making it stable. If the LSP is neutral, e.g. the so-called Neutralino, which is a mixture of the superpartners of the electroweak gauge bosons, this would be an ideal WIMP candidate.

Another scenario for the creation of dark matter in the early universe would be the so-called asymmetric dark matter (ADM) [19]. In ADM the asymmetry between matter and antimatter in the baryon sector is connected to a similar asymmetry in the dark sector. Either by transferring the initial asymmetry in the baryonic sector to the dark sector or vice versa, depending on the actual model. The initial amount of dark matter and anti dark matter in the universe is not constrained by the observed relic density and also the annihilation cross section can be arbitrarily large, since it is usually assumed that the symmetric component quickly annihilates and only the remaining asymmetric part survives and has to obey the relic density constraint. One consequence of this is the complete absence of annihilation signals in ADM models. The favored mass scale from ADM is $\mathcal{O}(\sim 5\,\mathrm{GeV}/c^2)$. The argument for this is that if the asymmetry in the baryonic and dark sector are indeed the same, also the number densities of matter and dark matter should be similar. Since the energy density of dark matter is about 5 times that of the baryonic matter, the dark matter particles should consequently be about 5 times heavier than the average matter particle, the proton.

For direct detection experiments there exists no practical difference between WIMP dark matter and ADM, except the different preferred mass scale. The complete absence of annihilation has, however, a strong impact on indirect searches.

Chapter 2

Direct Dark Matter Searches

The term *direct detection* generally refers to experiments searching for scattering of WIMP-like particles from the galactic halo in particle detectors operated on Earth. Although the number density, and thus the flux, of these particles is very large, the tiny cross sections involved lead to extremely low scattering rates. In combination with the low recoil energies caused by these scatterings, this makes the observation of a direct detection signal experimentally challenging. In the following, the experimental signature of dark matter-induced scattering, in particular the expected event rates and spectra, are discussed and a brief overview of the experimental techniques used in different experiments and their results is given.

2.1 Expected Signal

2.1.1 Recoil Energies

The mass of the dark matter particles searched for in direct detection experiments is assumed to be $\mathcal{O}(\mathrm{GeV}/c^2\text{- }\mathrm{TeV}/c^2)$, which is more similar to the mass of atomic nuclei than the mass of the electronic shell. One therefore expects the dark matter particles to dominantly scatter off the nuclei in the detectors. The recoil of the nucleus caused by such an elastic scattering has an energy of the $\mathcal{O}(\mathrm{keV})$ which can be roughly estimated by putting approximate values into the equation for the non-relativistic recoil energy:

$$E_R = \frac{|\vec{q}|^2}{2m_N} = \frac{\mu^2 v^2}{m_N}(1-\cos(\theta)) \lesssim \frac{\mu^2 v^2}{m_N} \tag{2.1}$$

where q is the transferred momentum, m_N is the mass of the target nucleus, v is the relative velocity of the two particles, θ is the scattering angle and μ is the reduced mass which is defined as

$$\mu = \frac{m_\chi m_N}{m_\chi + m_N} \tag{2.2}$$

where m_χ is the mass of the dark matter particle. Using a value of $100\,\mathrm{GeV}/c^2$ for the mass of the dark matter particle as well as the target nucleus and a typical velocity of $300\,\mathrm{km\ s^{-1}}$ results in a maximum recoil energy of 25 keV, a typical value for direct detection experiments. This value becomes smaller for lower dark matter masses.

2.1.2 Event Rates

In a simplified picture, the total event rate depends on the number of target nuclei N, the interaction cross section σ and the dark matter particle flux, which in turn depends on the average velocity $< v >$ of the dark matter particles relative to the detector and their number density, given by the local energy density of dark matter ρ_χ and the dark matter mass m_χ:

$$R \propto N \frac{\rho_\chi}{m_\chi} \sigma < v > \tag{2.3}$$

Direct measurements of the local dark matter density ρ_χ rely on the knowledge of the proper motions of stars in the solar neighborhood. A recent value obtained in [20] is

$$\rho_\chi = 0.39 \pm 0.03 \frac{\mathrm{GeV}}{\mathrm{cm}^3} \tag{2.4}$$

A comprehensive review of the efforts to determine ρ_χ is presented in [21]. Direct detection experiments have traditionally adopted a value of $0.3\,\mathrm{GeV}/c^2$, slightly lower than the value quoted above but still in line with other results discussed in [21]. To keep results comparable with other experiments, this work uses the canonical value of $0.3\,\mathrm{GeV}/c^2$ unless explicitly stated otherwise.

The exact expression for the cross section depends on the nature of the coupling. In direct detection experiments one generally distinguishes between spin-independent (SI) and spin-dependent (SD) interactions. For SI interactions the scattering can be assumed to be coherent because the wavelength of the dark matter particles is usually large compared to the size of the nuclei. In the most simple case, where the coupling for protons and neutrons is identical, this leads to A identical scattering amplitudes which are added in phase, giving a cross section which is proportional to A^2, where A is the atomic mass number of the target nucleus. Therefore, for the SI case, one quotes the results concerning the cross section in terms of the dark matter-nucleon cross section $\sigma_{\chi n}$, which is related to the total cross section σ via

$$\sigma = \sigma_{\chi n} A^2 \tag{2.5}$$

For heavier nuclei like xenon or tungsten, there is a noticeable loss of coherence for large transferred momenta q due to the finite size of the nucleus. This is quantified by the nuclear form factor $F(q)$, which makes the total cross section dependent on the recoil energy $E_R = q^2/(2m_N)$:

$$\sigma(E_R) = \sigma_{\chi n} A^2 |F(q)|^2 \tag{2.6}$$

For the form factor the parametrization by Helm [22] is used, which gives an analytical expression.

For SD interactions only those nuclei can contribute which have a non-vanishing nuclear spin. The cross section then is not proportional to the mass number of the nucleus but its spin J:

$$\sigma \propto (a_p \langle S_p \rangle + a_n \langle S_n \rangle)^2 \, \frac{(J+1)}{J} \tag{2.7}$$

where a_p, a_n are the effective couplings to protons or neutrons and $\langle S_p \rangle$, $\langle S_n \rangle$ are the expectation values of the proton and neutron spin in the nucleus.

There are three naturally occurring isotopes in $CaWO_4$, which is used as the target material in CRESST-II, with non-vanishing nuclear spin: ^{17}O, ^{43}Ca and ^{183}W. The low natural abundances of ^{17}O (0.038 %) and ^{43}Ca (0.135 %) lead to a negligible signal from SD interactions. And while the abundance of ^{183}W is quite high with 14.3 %, the nuclear spin of $J = 1/2$ originates from its unpaired neutron which has a very small value for $< S_n >= -0.031$ compared to e.g. $< S_p >= 0.441$ for ^{19}F (see [23] for a compilation of the spin values for the relevant isotopes). Thus SD interactions play no relevant role for a $CaWO_4$ target and are generally ignored for CRESST-II.

2.1.3 Energy Spectrum

The interpretation of experimental results requires the differential rate of nuclear recoils as a function of recoil energy. For this, one needs to replace the average velocity of the dark matter particles in Eq. 2.3 with their velocity distribution. This yields the following expression:[1]

$$\frac{dR}{dE_R} \propto \frac{\rho_\chi}{m_\chi} \frac{1}{2\mu^2} \sigma_{\chi n} A^2 |F(q)|^2 \int_{v_{min}}^{v_{esc}} \frac{f(\vec{v})}{v} d^3\vec{v} \tag{2.8}$$

The integration runs from v_{min}, the minimum velocity to produce a recoil with energy E_R, to v_{esc}, the galactic escape velocity. The canonical value for

[1] A detailed derivation of the formula for the recoil spectra can be found e.g. in [24].

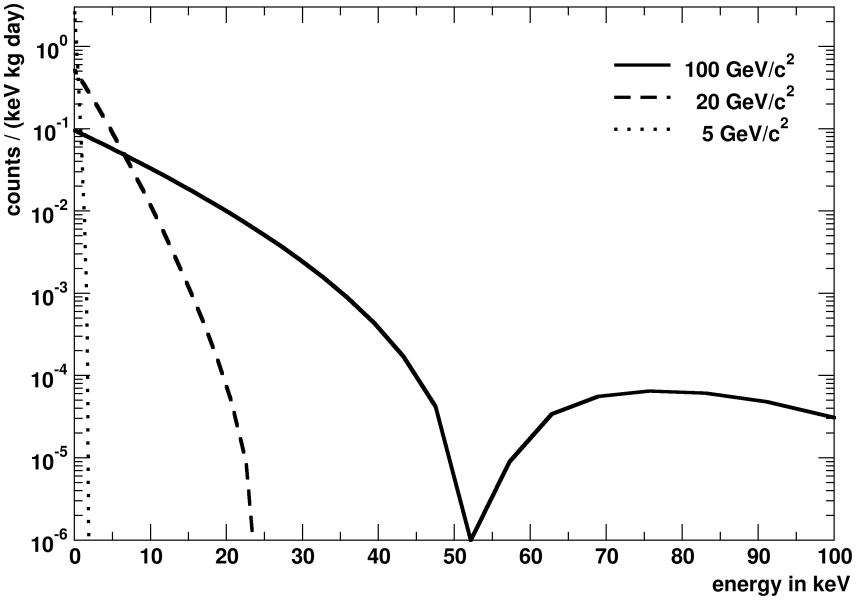

Figure 2.1: Recoil spectra for dark matter particles with masses of 5, 10 and 100 GeV/c^2 scattering off tungsten. For lower dark matter masses the recoil energies become smaller since lighter particles have less kinetic energy. Also the total rate increases because the number density of dark matter particles increases with decreasing mass.

the escape velocity is 544 km s^{-1} which is taken from [25] where it is determined as $v_{esc} = 544^{+64}_{-46}$ km s^{-1}. The more recent estimate from [26] gives a slightly lower value of $v_{esc} = 533^{+54}_{-41}$ km s^{-1} but is still in agreement with the canonical value above within the quoted uncertainty.

Since the exact velocity distribution is a priori not known, usually an isothermal halo is assumed (the so called *Standard Halo Model*). This leads to a Maxwellian velocity distribution, where the RMS velocity can be expressed in terms of the orbital velocity of the Local System at Earth's position in the galaxy $v_0 = 220$ km s^{-1}.

$$f(\vec{v}) = e^{-(\vec{v})^2/v_0^2} \tag{2.9}$$

Since the detectors are located on Earth, the motion of the earth through the galaxy has to be taken into account. The solar system moves with a velocity of $v_{sun} = 232$ km s^{-1} with respect to the Local System. Performing the coordinate change thus yields:

$$f(\vec{v}) = e^{-(\vec{v}+\vec{v_{sun}})^2/v_0^2} \tag{2.10}$$

In addition, the orbital motion of the earth around the sun can be considered. This leads to potential signatures for a dark matter signal discussed

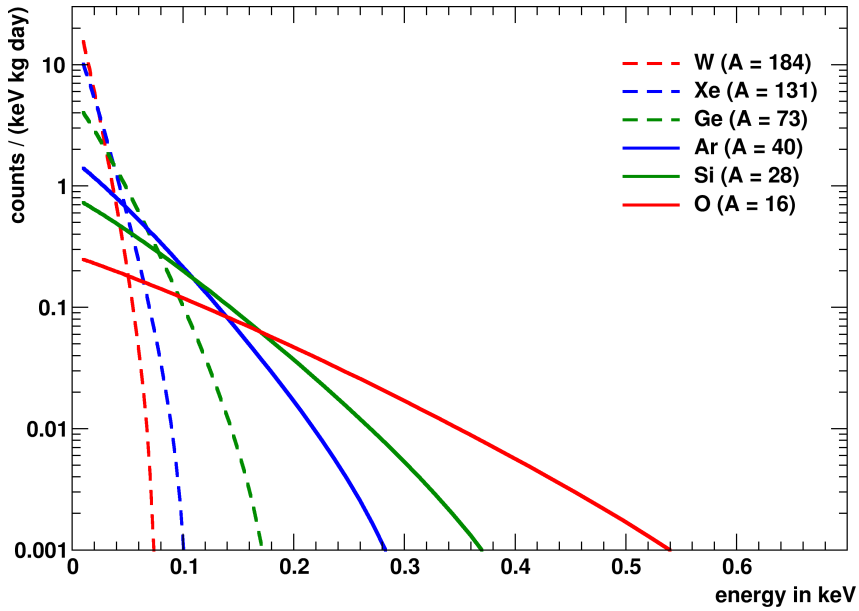

Figure 2.2: Recoil spectra for a $1\,\mathrm{GeV}/c^2$ dark matter particle scattering off different target nuclei. The total rate increases with increasing target mass due to the expected A^2 scaling of the cross section. The recoil energies, however, become smaller with increasing target mass, making it more difficult to observe these events in a real detector with finite energy threshold. Thus light target nuclei like oxygen are preferred when searching for dark matter particles with lowest masses.

below (cf. Sec. 2.1.4) which can be exploited by experiments.

Fig. 2.1 illustrates how the recoil spectrum changes with the mass of the dark matter particle. Increasing the mass leads to higher kinetic energies, since the velocity distribution of dark matter particles is independent of their mass. This in turn leads to higher recoil energies, making them easier to observe. On the other hand, the number density of dark matter particles decreases linearly with increasing mass, lowering the total rate for a given cross section. The dip in the recoil spectrum for $100\,\mathrm{GeV}/c^2$ particles scattering off tungsten is an effect of the nuclear form factor, which suppresses recoils with energies around 50 keV.

In Fig. 2.2 the influence of the mass number A of the target nucleus is shown. A higher A leads to a higher total rate due to the A^2-scaling of the spin-independent cross section. The recoil energies, however, become smaller for increasing A which makes the events harder to detect. This is why, for the lowest dark matter masses, targets with low A, like e.g. oxygen, are preferred, since for targets with higher A the entire spectrum remains below the energy threshold.

2.1.4 Modulation Effects

The orbit of the earth around the sun gives rise to an annual modulation of the observable recoil spectra. In summer, when the earth moves in the same direction as the sun, the recoil spectrum is shifted towards higher energies, whereas in winter the shift occurs in the opposite direction. Since a real detector has a finite energy threshold, this usually leads to a higher observed rate in summer and a lower rate in winter. This annual modulation signature should be observable in any dark matter signal. However, since the magnitude of the modulation is predicted to be only a few percent of the total rate, a large amount of dark matter events is required in order to resolve this modulation signature. Since most of the current experiments don't see a large dark matter signal, the annual modulation is usually ignored in the calculation of the recoil spectrum and instead an average spectrum (over the entire year) is used in the analysis.

In addition to the annual modulation of the recoil spectrum, there should be a diurnal modulation of the incoming direction of dark matter particles due to the rotation of the earth around its own axis [27, 28]. Yet, this effect is even more difficult to observe since in addition to a large amount of events it also requires novel detectors, capable to resolve the direction of the nuclear recoils. So far only prototype detectors exist which try to exploit this effect [29].

2.1.5 Presenting Results

The results are usually shown in the dark matter-nucleon cross section versus dark matter mass plane, since all other parameters in the formula for the expected recoil spectrum (Eq. 2.8) are fixed. Indications for a signal are usually displayed as contours enclosing the parameter space compatible with the data at a given confidence level. Null results are interpreted as upper limits on the cross section for a given mass, usually at the 90 % confidence level. The parameter space above the exclusion curve is excluded by the data. At high masses the exclusion curve is $\propto 1/m_\chi$ reflecting that the number density of dark matter particles decreases for larger dark matter masses. At the low mass end the exclusion curve rises sharply. This is an effect of the finite energy threshold, because only a small fraction of the recoil spectrum for light dark matter particles is observable above the threshold. A lower threshold causes the rise to shift towards lower masses (see Fig. 2.3).

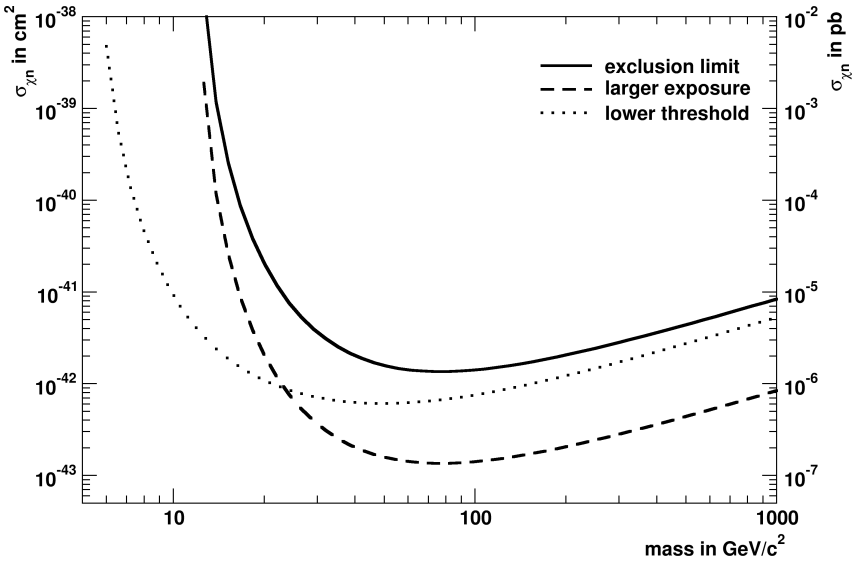

Figure 2.3: Examples for exclusion curves in the dark matter mass vs. dark matter-nucleon cross section plane. The parameter space above the respective curve is excluded. The solid curve shows the typical shape of an exclusion curve. The sharp rise at low masses is an effect of the energy threshold whereas the continuous rise towards higher masses is caused by the decreasing number density of dark matter particles. Lowering the threshold shifts the curve towards lower masses (dotted curve). Increasing the exposure (without observing additional events of course) shifts the exclusion limit downwards.

2.2 Experimental Techniques

To maximize the signal to background ratio, one can obviously try to increase the signal or reduce the backgrounds. Since the flux of dark matter particles is given, one can only try to optimize the detectors in order to detect as many of these particles as possible. This can be done by choosing suitable target nuclei to exploit e.g. the A^2-dependence in coherent SI scattering, lowering the energy threshold to be sensitive to a larger fraction of the recoil spectrum or increasing the number of target nuclei, i.e. the target mass.

Since the options to increase the signal rate are limited, most of the efforts in designing direct detection experiments are directed at the reduction of backgrounds. Ample shielding against environmental radioactivity and excessive screening of construction materials to avoid radioactive contaminations are mandatory in order to achieve competitive sensitivities. Also it is unavoidable to build the experiment in a deep underground laboratory to reduce the flux of cosmic ray particles, especially muons which can cause cascades of secondary particles that can mimic a dark matter signal.

To reach the best sensitivities, additional background reduction methods

beyond passive shielding are required. Most experiments focusing on SI interactions record multiple signals to discriminate nuclear recoil events, which comprise the expected signal events, from electronic recoils, which originate from the dominant radioactive backgrounds.

For SI dark matter searches, two main classes of experiments have evolved over the past years: experiments based on liquid noble gases and others based on cryogenic particle detectors. Current liquid noble gas experiments use either xenon or argon as their target material. They consist of a single monolithic detection volume which can reach masses of several 100 kg. The main signal recorded in these experiments is the scintillation light produced in a particle interaction. This is recorded by an array of photomultiplier tubes (PMT) which usually enables some sort of position reconstruction. This position reconstruction ability makes it possible to exploit the self shielding due to the target liquid by defining a fiducial volume in the center of the detector.

Among the liquid noble gas experiments one further distinguishes single phase experiments, like XMASS [30] or DEAP/CLEAN [31, 32], from dual phase experiments like Xenon100 [33], LUX [34], PandaX [35] or DarkSide [36]. Single phase experiments completely rely on the self shielding for background reduction and have no additional signal to discriminate nuclear and electronic recoils. Dual phase experiments, however, are operated as a time projection chamber (TPC). In a TPC an external electric field is applied to the detection volume which separates the electron-hole pairs created in a particle interaction. The electrons are then drifted through the detection volume in z-direction until they reach the gaseous phase on top of the liquid (hence the name dual phase). In the gaseous phase the electrons are accelerated by a second electric field, producing proportional scintillation light. A single particle interaction thus causes two signals the prompt scintillation from the liquid noble gas and - delayed by the drift time of the electrons - a secondary scintillation signal which is proportional to the ionization. Both signals are read out by PMT arrays on the top and bottom of the detector giving the x-y-coordinates of the event from the hit pattern. The z-coordinate can be inferred from the drift time. The ratio of the ionization signal and the prompt scintillation signal can be used to discriminate nuclear and electronic recoils. Dual phase experiments based on liquid xenon currently achieve the best sensitivity to dark matter particles with masses above $\sim 10\,\mathrm{GeV}/c^2$.

Cryogenic experiments use detectors where the signal is based on the phonons created in a particle interaction to reconstruct the deposited energy. The main advantage of these detectors is the excellent energy resolution and sensitivity to low energies, since most of the energy deposited in the detector is eventually converted into phonons and the tiny excitation energy needed for phonons

($\mathcal{O}$(meV)) means that the energy resolution is not limited by statistics like in scintillation or semi-conductor detectors, where excitations are on the $\mathcal{O}$(eV). However, this method only works at very low temperatures ($\mathcal{O}$(mK)) requiring the use of dilution refrigerators. This is due to the fact that the signal in these detectors is inversely proportional to their heat capacity which scales as $\propto T^3$ at temperatures close to absolute zero.

CRESST, which is described in more detail in the following chapter, is one of the experiments which pioneered this technology. Currently scintillating absorber crystals are used to provide discrimination of nuclear recoil events. The two other notable cryogenic experiments, EDELWEISS [37] and CDMS [38], both use germanium or silicon as material for their detectors. Their detectors are simultaneously operated as diodes and they are using the additional ionization signal for discrimination. Currently, cryogenic experiments do not reach the same low background levels as the liquid noble gas experiments. However, the lower energy threshold gives them a decisive advantage for detecting dark matter particles with masses $\lesssim 10\,\mathrm{GeV}/c^2$.

Recently the CDMS collaboration has demonstrated a way to lower the energy threshold of their detectors by applying a higher bias voltage to the charge electrodes [39]. The drifting of the electron-hole pairs due to this bias voltage creates secondary phonons - the so-called Neganov-Luke phonons [40, 41]. This effect can be exploited to increase the phonon signal by increasing the bias voltage.[2] The downside of this approach is that the discrimination ability due to the additional charge signal has to be sacrificed and so the sensitivity which can be obtained is limited by the e^-/γ -background. Nonetheless, recent results from the CDMS collaboration are competitive for masses around 1-10 GeV/c^2 [39].

A novel approach to search for light dark matter particles is pursued by the DAMIC collaboration. They employ a silicon CCD with 4.2 million pixels to search for dark matter induced nuclear recoils using the hit pattern to discriminate backgrounds. First results show competitive sensitivity for low dark matter masses [43].

Another notable class of experiments tries to exploit the annual modulation signature due to the motion of the earth around the sun. The most prominent representative of these experiments is the DAMA dark matter search [44] which is operating a large array of NaI scintillation detectors in the Gran Sasso underground laboratory. They claim to have observed an annual modulation signal compatible with a dark matter interpretation with very high statistical significance. Attempts to reproduce this result with similar setups, e.g. by

[2] This is also being studied within the CRESST collaboration to increase the sensitivity of the light detectors [42]

the KIMS experiment [45] which uses CsI crystals or the DM-Ice experiment [46] which uses NaI detectors buried in the antarctic ice at the south pole, have so far not been able to confirm the DAMA result. The standard dark matter interpretation of this modulation signal is in strong tension with the null results of other experiments which sparked numerous attempts to reconcile these conflicting results in more exotic models of dark matter.

The CoGeNT experiment [47], which uses a single high-purity p-type point-contact germanium detector with a low energy threshold of $\sim 0.5\,\mathrm{keV}$ for electronic recoils (corresponding to $\sim 2-3\,\mathrm{keV}$ for nuclear recoils), reported an excess of events at low energies which can be attributed to light dark matter particles. In $\sim 16\,\mathrm{months}$ of data taken at the Soudan underground laboratory they found a $2.8\,\sigma$ evidence for annual modulation consistent with a dark matter origin. In a more recent publication [48] using three years of data, this significance decreased, however, to $2.2\,\sigma$ and the reported amplitude of the modulation is inconsistent with a standard Maxwell-Boltzmann halo. Another analysis [49] shows that the low energy excess seen by CoGeNT can be explained by misidentified surface events.

2.3 Recent Results

Figs. 2.4 and 2.5 show the most recent published results on the spin-independent dark matter-nucleon cross section from direct detection experiments. To improve readability, the results primarily relevant for masses $\lesssim 10\,\mathrm{GeV}/c^2$ are omitted in Fig. 2.4 and shown separately in Fig. 2.5 instead.

The orange region shows the parameter space compatible with the long-standing dark matter interpretation from the annual modulation observed by the DAMA experiment. By now, the interpretation in the framework of weakly interacting SI dark matter, however, is ruled out by almost all other direct detection experiments.

The blue curves show the 90 % upper limits from the liquid noble gas experiments. Currently PandaX (dotted blue) and LUX (solid blue) set the most stringent limits for SI dark matter above $\sim 7\,\mathrm{GeV}/c^2$ followed by Xenon100 (dashed blue). First results from the liquid argon experiment DarkSide50 (dash-dotted blue) suffer from a rather high energy threshold introduced by the pulse-shape discrimination between nuclear and electronic recoils possible in liquid argon and are limited to masses $\gtrsim 20\,\mathrm{GeV}/c^2$.

The results from semi-conductor based experiments are shown in green. Two possible signal regions can be seen: in light green the 95 % C.L. region compatible with an excess seen in the silicon detectors of CDMS-II and in dark green the 99 % C.L. region corresponding to an annual modulation signal seen

in data from the CoGeNT experiment. While the CoGeNT region is already fully excluded by LUX, PandaX and Xenon100, the CDMS-Si region is also fully excluded by first results from a low threshold analysis of SuperCDMS (dotted green in Fig. 2.4 and solid green in Fig. 2.5).

The regions shaded in light red stem from an excess of events observed in run 32 of CRESST-II (cf. Sec. 3.4). These excess events are, however, most likely caused by backgrounds as will be discussed in this work. First results from run 33 of CRESST-II (dashed red in Fig. 2.5), which are also a topic of this work, rule out almost all of the parameter space compatible with the run 32 excess. Further results from run 33 (solid red in Fig. 2.5) extend the parameter space covered by direct dark matter searches to the sub-GeV/c^2-regime.

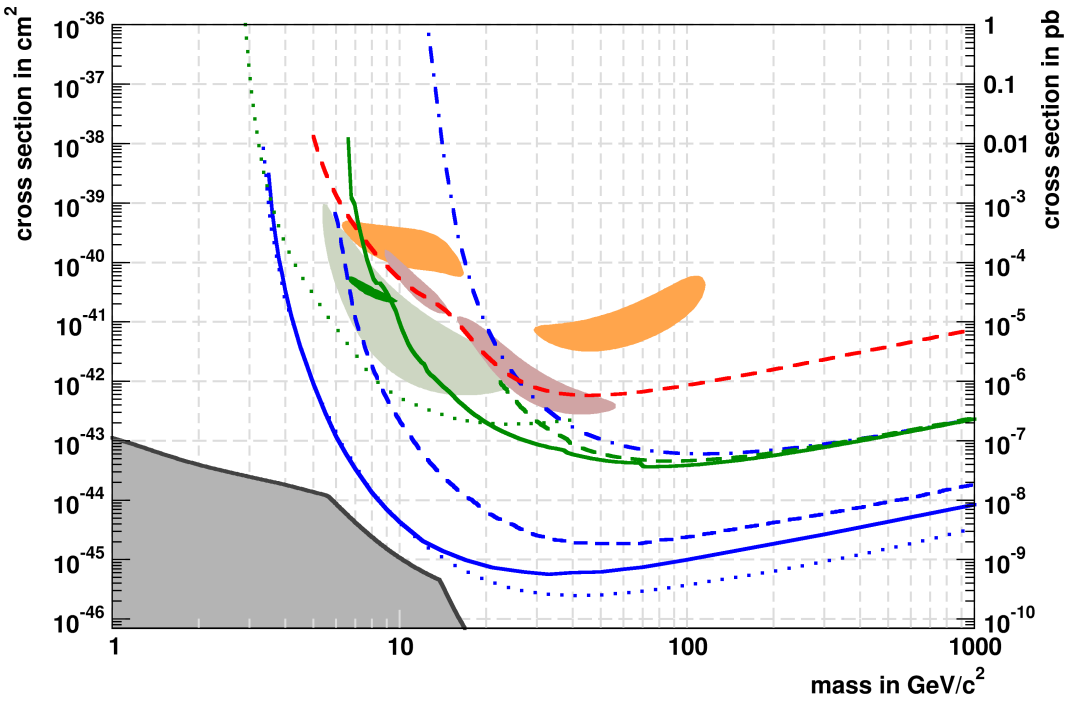

Figure 2.4: Parameter space for spin-independent dark matter-nucleon scattering focusing on masses $\gtrsim 10\,\mathrm{GeV}/c^2$. The shaded regions indicate the parameter space favored by DAMA [50] (orange, $3\,\sigma$, as interpreted by Savage et. al. [51]), CDMS-II-Si [52] (light green, 95 % C.L.), CoGeNT [47] (dark green, 99 % C.L.) and CRESST-II (run 32) [53] (light red, $2\,\sigma$). The lines indicate the 90 % C.L. upper limits from LUX [54] (solid blue), PandaX [55] (dotted blue), Xenon100 [56] (dashed blue), DarkSide 50 [57] (dash-dotted blue), CMDS-II [38] (solid green), EDELWEISS-II [58] (dashed green), SuperCDMS [59] (dotted green) and a re-analysis of the CRESST-II commissioning run [60] (dashed red). The gray region indicates the region in the parameter space where coherent scattering of solar and atmospheric neutrinos becomes a background for a $CaWO_4$ based dark matter experiment [61].

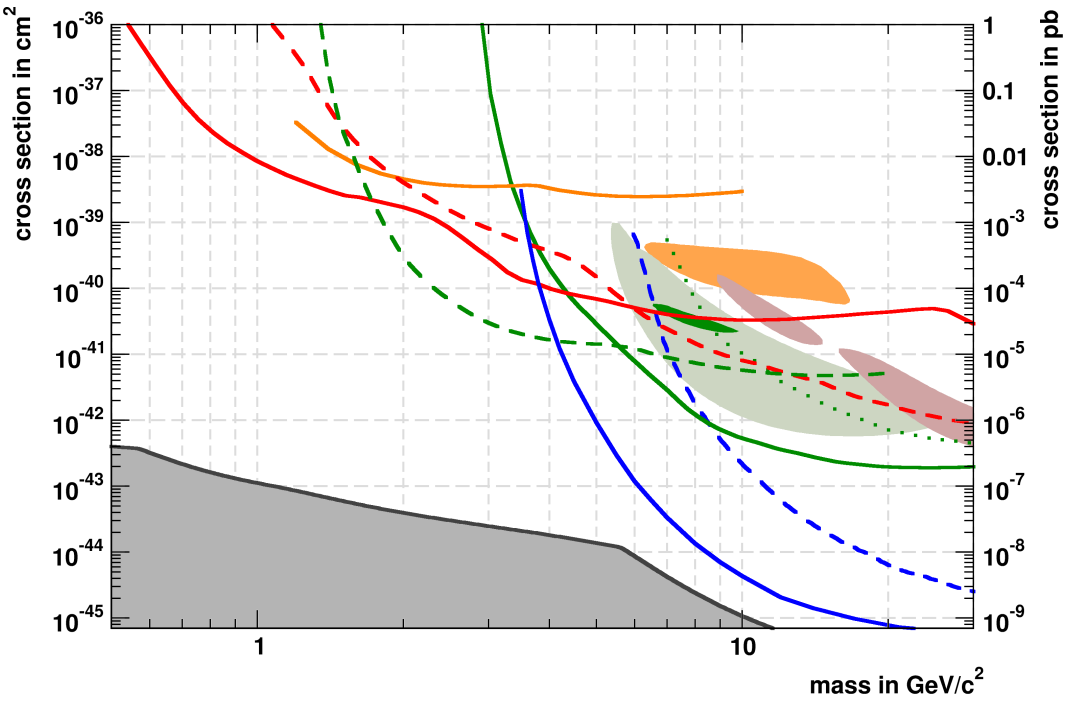

Figure 2.5: Parameter space for spin-independent dark matter-nucleon scattering focusing on masses $\lesssim 10\,\mathrm{GeV}/c^2$. The shaded regions indicate the parameter space favored by DAMA [50] (orange, $3\,\sigma$, as interpreted by Savage et. al. [51]), CDMS-II-Si [52] (light green, 95 % C.L.), CoGeNT [47] (dark green, 99 % C.L.) and CRESST-II (run 32) [53] (light red, $2\,\sigma$). The lines indicate the 90 % C.L. upper limits from LUX [62] (solid blue), Xenon100 [56] (dashed blue), SuperCDMS [59] (solid green), CDMSlite [63] (dashed green), EDELWEISS-II [64] (dotted green) and DAMIC [43] (solid orange). The two red curves correspond to recent results from phase 2 of CRESST-II using detectors Lise [65] (solid red) and TUM40 [66] (dashed red) which are discussed in this work. The gray region indicates the region in the parameter space where coherent scattering of solar and atmospheric neutrinos becomes a background for a $CaWO_4$ based dark matter experiment [61].

Chapter 3

The CRESST Experiment

CRESST is an acronym which stands for Cryogenic Rare Event Search with Superconducting Thermometers. It is an experiment searching for nuclear recoil events induced by weakly interacting dark matter particles scattering off the nuclei composing the detector material. In the early stages of CRESST, cryogenic particle detectors made of sapphire (Al_2O_3) were used, which allow a very precise reconstruction of the energy deposited in the absorber crystal. These detectors are read out by tungsten transition edge sensors (TES) directly evaporated on the absorber crystals. The operating temperature of these TES is $\sim 10 - 20\,\mathrm{mK}$, requiring the use of a dilution refrigerator.

Since the expected event rate due to dark matter particles is very low, much care has to be taken to prevent exposure of the detectors to environmental radiation by proper shielding and selection of radio-pure materials. To mitigate the impact of ionizing background radiation, detectors using scintillating absorbers have been developed in the past. The additional signal from the scintillation light is recorded by a second cryogenic detector made of a thin disc of silicon (again read out by a TES). In combination with the signal from the absorber crystal (the so-called phonon signal), the light signal can be used to discriminate different types of interactions. This is possible, since a nuclear recoil produces less scintillation light than an electron or gamma event of the same energy. Out of several materials which have been studied, $CaWO_4$ has emerged as the material of choice for the current generation of detectors.

3.1 CRESST Detectors

3.2 Detector Module

A CRESST-II detector module consists of a scintillating absorber crystal (phonon detector) made of $CaWO_4$ and a separate light detector made of silicon or sap-

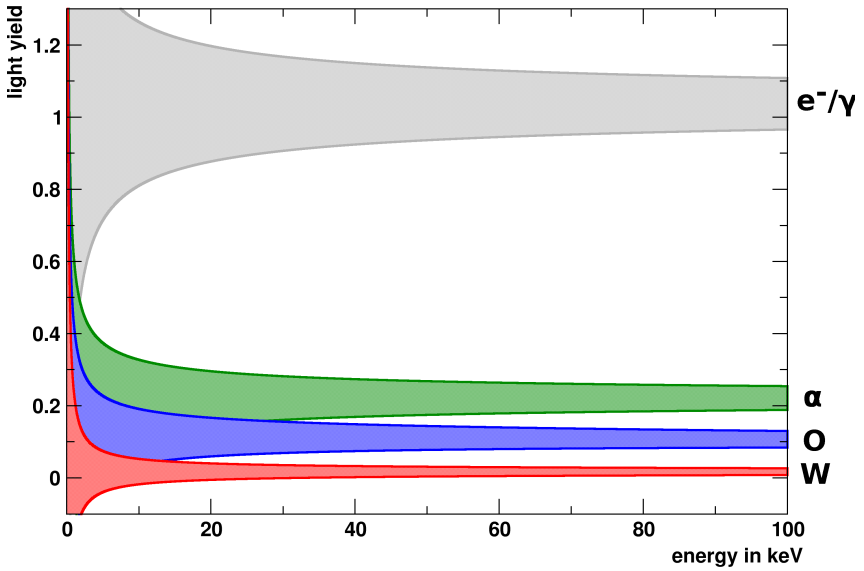

Figure 3.1: Illustration of the event distribution in $CaWO_4$ for different types of interactions in the energy-light yield plane. The light yield of e^-/γ -events (gray) is set to 1 at high energies. Compared to that, the light output for α-particles (green) and nuclear recoils is reduced. The recoils off the lighter oxygen nuclei (blue) appear at higher light yields than those off the heavier tungsten nuclei (red). The calcium band, which lies between the oxygen and tungsten bands, is omitted for clarity.

phire, coated with a thin film of silicon (SOS - silicon on sapphire). The amount of light produced in the absorber for a given energy deposit depends on the type of the particle which is interacting. The light output for electrons and γ-rays at room temperature has been found to be 15,000-20,000 photons/MeV [67] and is further increased by a factor of ~ 2 at mK temperatures [68, 69]. For heavier particles interacting with the crystal, the light output is reduced. This can be explained in a simplified picture by the increased ionization density of heavier particles compared to that of electrons. This leads to a higher probability of non-radiative decay of the initially produced excitons, before they can reach a luminescence center. This effect is called *quenching*. A detailed model of the light production in $CaWO_4$ including temperature dependent effects and light quenching can be found in [70].

This light quenching can be exploited to separate nuclear recoils from e^-/γ -events on an event-by-event basis based on the light yield $LY = \frac{E_L}{E_P}$, which is defined as the ratio of the energy E_L detected in the light detector and the energy E_P detected in the phonon detector (cf. Sec. 4.5.2). The different classes of events are then expected to cluster in bands around their mean light yield defined by the so-called quenching factor (QF), which quantifies the

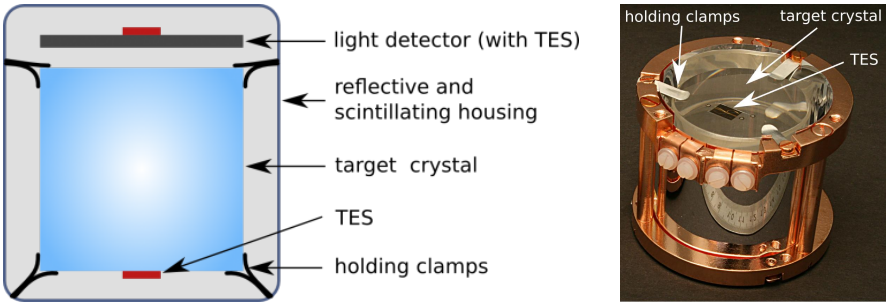

(a) Schematic drawing of conventional detector design.

(b) Picture of a conventional detector module.

Figure 3.2: Schematic drawing and picture of conventional module design. (credit: CRESST collaboration)

reduction of light output relative to e^-/γ -events. The width of these bands is determined by the energy resolutions of the phonon and light detectors (cf. Sec. 4.5.2). As one can see from Fig. 3.1, it is even possible to separate nuclear recoils off different nuclei to some extent.

In the conventional design discussed here (see Fig. 3.2), the $CaWO_4$ crystal is cylindrical with a diameter and height of $\sim 4\,\mathrm{cm}$ which leads to a mass of $\sim 300\,\mathrm{g}$ per detector. Both absorber and light detector are equipped with a TES (see below) to measure the energy deposited by the particle interactions in the absorber or the scintillation light in the light detector. The crystal is held in place inside its copper housing by bronze clamps which remain flexible even at mK temperatures. This is important to reduce the influence of mechanical vibrations due to e.g. the cryostat. To improve light collection the entire module is surrounded by a highly reflective polymeric foil, which has close to 100 % reflectivity for optical photons.

In addition to being highly reflective, the foil also scintillates. This can be exploited to veto a certain class of backgrounds related to α-decays on the crystal surface or surfaces surrounding the absorber crystal. After an α-decay not only the emitted α-particle may be detected, but also the recoiling daughter nucleus (see Fig. 3.3). Such a nucleus emitted in an α-decay will produce a nuclear recoil signal in the absorber which is basically indistinguishable from recoils off tungsten. For typical α-emitters with energies $\mathcal{O}(5\,\mathrm{MeV})$ and mass numbers $A \gtrsim 150$ the daughter nuclei have kinetic energies $\mathcal{O}(100\,\mathrm{keV})$, only slightly above the energy range relevant for dark matter search. If the nucleus loses part of its energy before being absorbed in the detector, e.g. when it is implanted just below the surface facing the absorber, it may well end up in the acceptance region for dark matter and pose a dangerous background as could

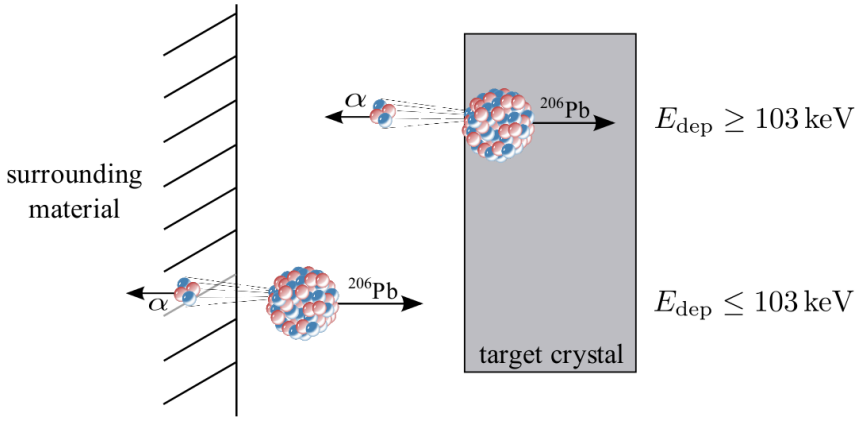

Figure 3.3: Illustration of background events from nuclei in α-decays using the example of ^{210}Po. If the decay happens on the crystal surface (top), the energy deposited in the absorber is $\gtrsim 103\,\mathrm{keV}$ (the kinetic energy of the ^{206}Pb daughter nucleus). If the decay happens on a surface facing the absorber (bottom), the deposited energy is $\lesssim 103\,\mathrm{keV}$, since part of the energy can be lost before the absorber is reached. Taken from [53].

be seen in the previous run 32 (cf. Sec. 3.4).

If such a decay happens on a scintillating surface like the foil, the α-particle, which is emitted in the opposite direction of the nucleus, produces additional light when absorbed in the scintillator. This additional light shifts the event upwards in the energy-light yield plane, making it possible to identify and reject these events.

3.2.1 Thermometers and Read Out

As mentioned in the introduction, CRESST uses cryogenic detectors to record the energy deposited by particle interactions. In a cryogenic detector, the phonons created in a particle interaction are collected in a thermometer which then outputs an electrical signal that can be digitized. The advantage of cryogenic detectors lies in the low excitation energy of the individual phonons $\mathcal{O}(\mathrm{meV})$, so phonon statistics does not limit the achievable energy resolution (and thus energy threshold) as e.g. photon statistics does in scintillation detectors. This is demonstrated in TES based microcalorimeters which achieve the best energy resolutions in x-ray detectors with $1.8 \pm 0.16\,\mathrm{eV}$ at $\sim 6\,\mathrm{keV}$ [72].

Similar TESes are used as thermometers for CRESST detectors. They exploit the sharp transition between the superconducting and normal conducting state of a material, translating small temperature changes $\mathcal{O}(\mu\mathrm{K})$ into a measurable change of resistance (see Fig. 3.4). In order to reach the low transition

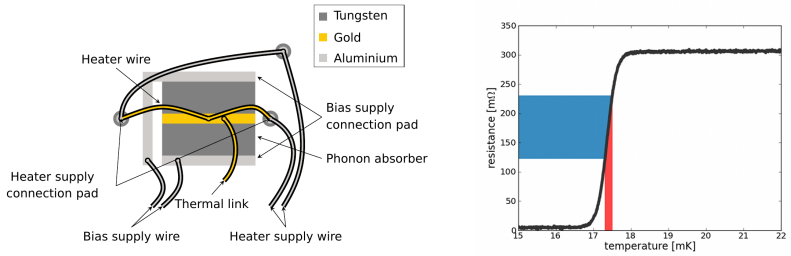

(a) Schematic drawing of the TES design. Taken from [71].

(b) Working principle of a TES: a small temperature increase (red) is converted into a large increase in resistance (blue).

Figure 3.4: Schematic drawing and working principle of a TES.

temperatures, which are desired to lower the heat capacity of the absorber crystals, thereby increasing the sensitivity of the detector, the TES are made of thin films of tungsten, which can be produced with a critical temperature around 15 mK. In addition to the tungsten film, the sensor consists of a gold bond pad, which provides the thermal link to the heat bath, and an ohmic heater, which is used to stabilize the detector at its operating temperature in the transition curve independently of the bath temperature by injecting pulses of defined energy into the TES. In addition these heater pulses are also used to calibrate the response of the detector (cf. Sec. 4.2.2).

The resistance change of the thermometer is read out by a circuit based on a SQUID (super-conducting quantum interference device), which can precisely measure magnetic flux. The TES is therefore connected in parallel to the input coil of the SQUID which in turn is connected in series to a shunt resistor (see bottom right of Fig. 3.5). The entire circuit is biased with a constant current which is $\mathcal{O}(\mu\text{A})$. A change in resistance of the TES causes a change in the branching of the bias current. This alters the magnetic flux in the input coil which can then be measured by the SQUID and further read out by a digitizer.

3.2.2 Data Acquisition System

A schematic view of the data acquisition system (DAQ) is presented in Fig. 3.5. The components of the three different circuits are shown color coded together with the temperature stage each component is located at. The red circuit is responsible for generating the input current for the TES heater. The DAC generates a constant current which can be adjusted to keep the TES in its desired operating point. The pulser can add short pulses on top of the constant current which are used to probe the operating point and to calibrate the de-

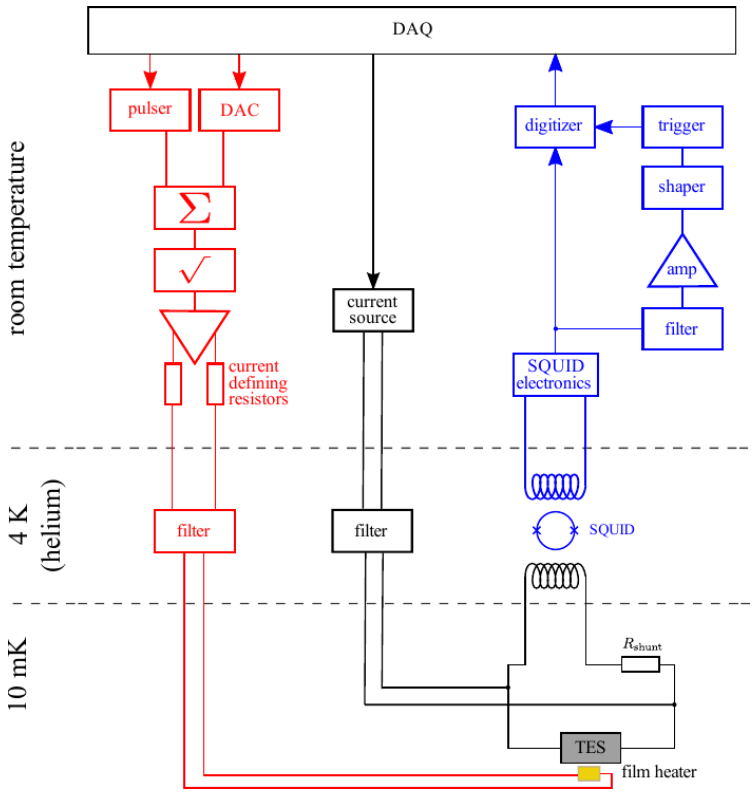

Figure 3.5: Schematic view of the DAQ system for one channel. Figure taken from [73].

tector response. The analog square root circuit is needed to keep the injected pulse height proportional to the injected energy (which is proportional to the current squared).

The black circuit contains the source for the bias current and the parallel circuit described above. The TES and the shunt resistor are mounted at the mixing chamber temperature level, whereas the SQUID is mounted at helium bath temperature. The SQUID is then connected to the blue circuit which does the triggering and digitization. For this the output of the SQUID electronics is split in two. One of these signals is shaped and amplified and sent to the trigger unit which sends a trigger signal to the digitizer if the shaped signal is above an adjustable threshold. If the digitizer receives a trigger signal, it samples the unshaped signal with a timebase of 40 μs and a record length of 8192 samples with 16 bit resolution. The record consists of the pre-trigger region - the first quarter of the trace (2048 samples) which occurred before the trigger and contain mostly information about the baseline - and the post-trigger region - the remaining trace (6144 samples) which contain the pulse.

The phonon and light detector of a module are always read out together when at least one of them has a valid trigger. Other modules are only read

out simultaneously if they have a valid trigger themselves. Each digitizer used has 8 channels, so up to four modules can be connected to one digitizer and all channels on a digitizer have to be read out in parallel. This leads to problems if a second trigger occurs on a digitizer within the post-trigger time of the first record. If such a trigger happens close to the end of the record, not enough information is recorded to evaluate the pulse. To avoid this, the trigger for the other detectors connected to a digitizer is blocked after half the post-trigger time. To identify which detector on a digitizer caused the initial trigger the trigger delay parameter is set by the DAQ. It counts, for every detector that is read out, the number of samples since the initial trigger. For detectors that did not cause a trigger, the parameter is set to an overflow value. This allows to select e.g. events that happened only in the light detector of a module.

After a complete record has been sampled, the digitization is paused during the transfer of the data to disk. To ensure a complete pre-trigger region for the next record, the triggers are not immediately re-activated after the data transfer is finished and an additional waiting time of one pre-trigger length is introduced. The DAQ dead time due to the times where the trigger is blocked is calculated by the DAQ system and stored together with each record. It has to be removed from the live time when the exposure is calculated.

3.3 Setup at Gran Sasso

The experiment is located at the Laboratori Nazionali del Gran Sasso (LNGS) in Italy. The Gran Sasso mountains provide ample shielding against cosmic muons with a rock overburden of at least 1,400 m in each direction. This lowers the muon rate from 100-200 m^{-2} s^{-1} at sea level to $\sim 1\,\mathrm{m}^{-2}$ h^{-1} in the underground lab (see Fig. 3.6). This is very important since firstly, the overall event rate would be too high to operate the rather slow W-TES detectors at sea level and secondly, muon induced neutrons are one of the most relevant backgrounds for direct dark matter search experiments and can only be avoided by going deeply underground.

The central piece of the setup (see Fig. 3.7) is the dilution refrigerator which provides a base temperature of $\sim 10\,\mathrm{mK}$. The carousel, which is coupled via a cold finger to the mixing chamber of the cryostat, is designed to house up to 33 detector modules, each module requiring two SQUID readout channels. Since currently only 36 out of 66 readout channels are operational, only 18 detector modules can be operated at a time.

The shielding follows the usual layered approach: the innermost parts of the shielding are made of ultra pure copper and small amounts of Plombum and Boliden lead, which have a reduced U/Th content, to avoid contamination from

radio-impurities within the shielding itself. This is surrounded by ordinary lead and together the lead and copper shielding basically remove the environmental e^-/γ -background, leaving only contributions from within the shielding. The lead and copper shielding is surrounded by a layer of polyethylene (PE), which substantially reduces the flux of neutrons from the rock surrounding the experiment. For the most recent run 33 an additional PE shield was put between the carousel and the IVC of the cryostat. GEANT4 [75] simulations have shown that this should further reduce the expected neutron rate at the detectors.

Another dangerous source of background is radon emanating from the rock surrounding the experiment. In order to prevent the accumulation of radon within the shielding, an airtight box surrounds the experiment which is constantly flushed with nitrogen boiling off from the liquid nitrogen shield. To avoid radio frequency induced noise, the entire setup is put in a Faraday cage.

In addition to the passive shielding, the experiment is enclosed by an active muon veto which consists of 20 plastic scintillator panels read out by photomultipliers. The purpose of the muon veto is to identify the remaining muons which manage to pass through the rock of the Gran Sasso mountain, so events in the cryogenic detectors which are coincident with muons can be discarded.

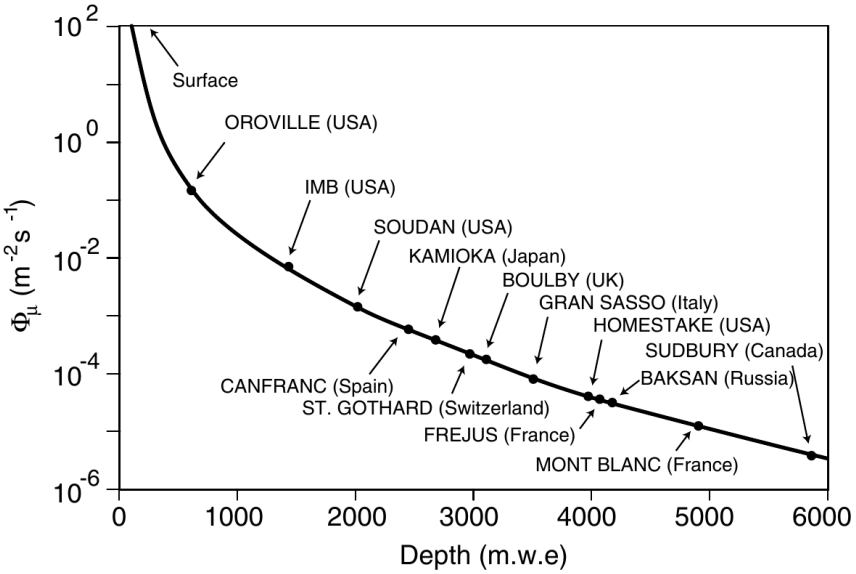

Figure 3.6: Muon flux vs. depth for various underground laboratories. Figure taken from [74].

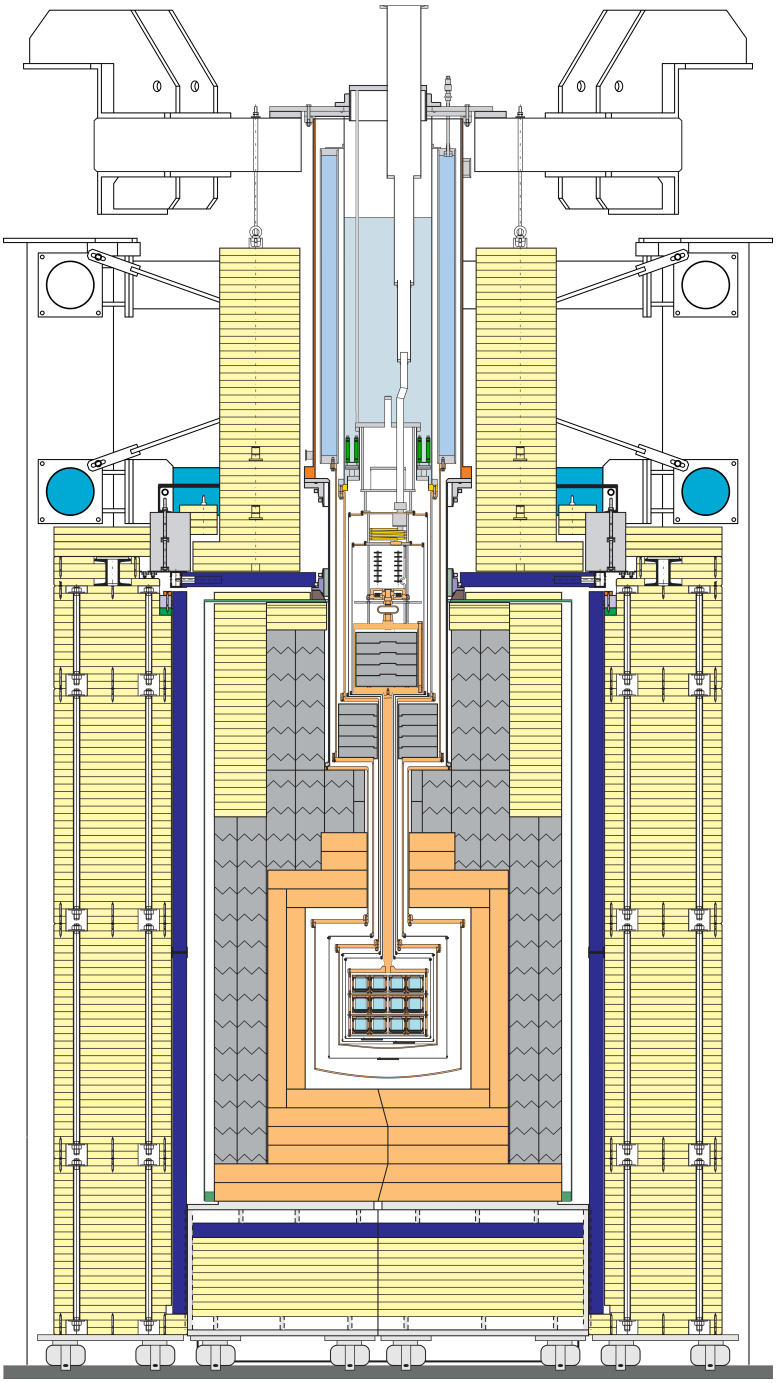

Figure 3.7: Schematic drawing of the CRESST setup at LNGS. Shown in the top center is the cryostat which is connected via a copper cold finger to the carousel containing the detectors in the bottom center. This is surrounded by the PE shielding (light yellow), the copper shielding (orange) and the lead shielding (gray). The plastic scintillator panels of the muon veto detector are drawn in dark blue. (credit: CRESST collaboration)

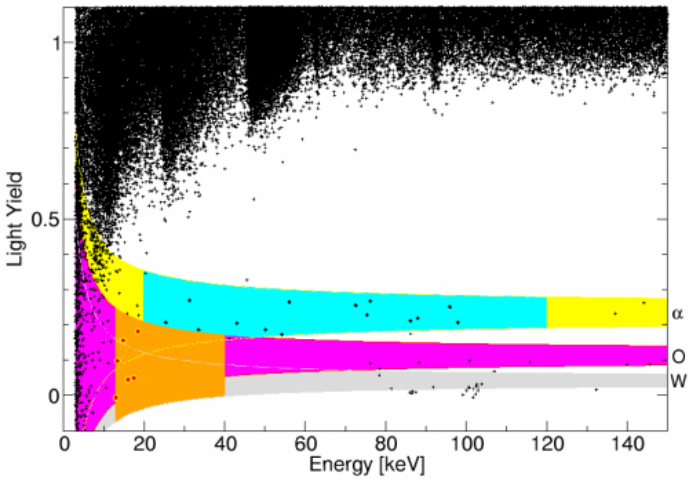

Figure 3.8: Data from one of the modules in run 32 in the energy-light yield plane (black dots). The acceptance region for dark matter candidates is highlighted in orange, the events lying therein are highlighted in red. The oxygen and tungsten bands are drawn in magenta and gray respectively. The yellow band contains the α-events, the green region depicts the side-band used to constrain the rate of degraded α-particles. Taken from [53].

3.4 Recent Results from Run 32

In run 32 of the CRESST-II experiment an exposure of 730 kg days was collected between July 2009 and March 2011 using 8 detector modules with a mass of 300 g each [53]. In the final dataset, a total of 67 events were observed in the acceptance regions for dark matter candidates which were chosen such that for each detector one background event due to leakage from the e^-/γ -band was expected. Besides this e^-/γ -background, additional sources of background events were determined and an attempt was made to model these backgrounds in order to include them in a maximum-likelihood analysis.

One of the background sources which was considered are neutrons. In contrast to dark matter particles, neutrons have a non-negligible probability to cause a signal in more than one detector. The exact ratio of multiple to single scatter events can be used to estimate the rate of neutron events. For this, simulations based on GEANT4 were performed where the entire setup of the experiment was irradiated with neutrons [76]. In these simulations two classes of neutrons were considered which exhibit different behavior: radiogenic neutrons from radioactive contaminations the surrounding materials and muon-induced neutrons. Muon-induced neutrons cause higher multiplicities compared to radiogenic neutrons, which provides a handle to identify muon-induced events missed by the muon veto.

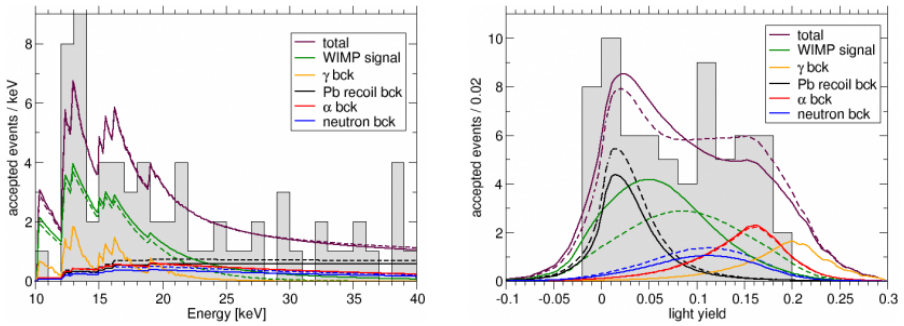

(a) Best fit energy spectrum for M1 (solid) and M2 (dashed).

(b) Best fit light yield distribution for M1 (solid) and M2 (dashed).

Figure 3.9: Best fit energy spectrum and light yield distribution for M1 and M2 obtained by the likelihood analysis of run 32 data. In gray a histogram of the energies/light yields of all accepted events is drawn. The colored curves correspond to the energy/light yield distributions of the different background components at the best fit points. Taken from [53].

Another dangerous source of background events is related to α-decays on surfaces facing the absorber crystal (cf. 3.2). Usually α-particles from radioactive contaminations have energies in the MeV range, far above the energies relevant for dark matter searches. However, if the α-decay happens just beneath the surface, the emitted α-particle will lose part of its energy inside the material. These so called degraded α-particles could be observed in run 32 data with energies leaking into the acceptance regions. The spectral shape of these events appeared to be flat at energies below $\sim$ 100 keV and the rate was estimated from an overlap-free side-band between $\sim$ 20 and $\sim$ 120 keV.

In addition to these degraded α-particles, also the daughter nuclei from α-decays could be observed in the data, causing nuclear recoil events at low energies. A peak around 103 keV was attributed to ^{206}Pb nuclei from α-decays of ^{210}Po. Again energy loss in the surrounding material causes leakage of these events into the acceptance region. Simulations of ^{210}Po nuclei implanted in the surrounding material with different implantation profiles were performed using the SRIM package [77] which can calculate the energy loss and range of ions in matter. The shape of the spectrum close to the 103 keV peak was used to select the most suitable implantation profile, which then was used to model this background in the likelihood analysis.

Both the degraded α events as well as the recoil background can be vetoed if the α-decay happens on a scintillating surface. Then the additional light produced by the particle not hitting the absorber crystal but the scintillator shifts the corresponding event to higher light yields and out of the acceptance region. In the modules used for run 32 most of the surfaces facing the absorber

Table 3.1: Best fit results from maximum likelihood analysis of run 32, reproduced from [53].

	M1	M2
e^-/γ -events	8.00 ± 0.005	8.00 ± 0.005
α-events	$11.5^{+2.6}_{-2.3}$	$11.2^{+2.5}_{-2.3}$
neutron events	$7.5^{+6.3}_{-5.5}$	$9.7^{+6.1}_{-5.1}$
Pb recoil events	$15.0^{+5.2}_{-5.1}$	$18.7^{+4.9}_{-4.7}$
signal events	$29.4^{+8.6}_{-7.7}$	$24.2^{+8.1}_{-7.2}$
WIMP mass in GeV/c^2	25.3	11.6
cross section in cm^2	$1.6 \cdot 10^{-42}$	$3.7 \cdot 10^{-41}$
stat. significance	4.7σ	4.2σ

crystal already were scintillating since the reflective foil surrounding the entire detector emits scintillation light. Only small areas, notably the bronze clamps holding the absorber crystal in place, were not covered with scintillating material and thus presented a possible origin of these backgrounds.

The number of background events for each type was fitted separately for each detector, taking into account the constraints from the side-band data. In addition, a common dark matter signal was added to the likelihood with $\sigma_{\chi n}$, the dark matter-nucleon cross section, as a free parameter. The likelihood exhibited two maxima denoted M1 and M2 with a (local) statistical significance of $4.7\,\sigma$ and $4.2\,\sigma$ respectively for the contribution of a dark matter signal, compared to the considered backgrounds alone. The presence of two regions in the parameter space compatible with a dark matter signal stems from the fact that the distribution of background events and dark matter signal in the light yield coordinate is not unambiguous.

3.5 Detectors installed in Run 33

In total, 18 modules are installed in run 33 (see Tab. 3.2): 12 of them are of the same design as was used in the previous runs and that is described in Sec. 3.2. They are either denoted as *conventional* when the TES is directly evaporated on the absorber crystal, or *composite*, where the TES is evaporated on a small carrier crystal which is then glued onto the absorber. The other 6 modules have one of three different new designs (*carrier*, *beaker* and *stick*). These novel designs have been developed with the goal to provide a fully active veto for surface backgrounds related to α-decays (cf. Fig. 3.3), since it has been pointed

Table 3.2: List of installed modules in run 33. Some of the light detectors are equipped with an ^{55}Fe source, so the response of the detector can be measured in absolute energy. Except for the light detector of module Rita/Steven all detectors are operational.

name	mass in g	type	comments
Daisy/Donald	307	conventional	—
Verena/Q	306	conventional	—
VK31/Kurt	307	conventional	—
VK32/Anders	308	conventional	—
VK33/Franz	310	conventional	—
VK34/Leon	304	conventional	^{55}Fe source
Wibke/X	308	conventional	—
Anja/Claudius	308	composite	—
Zora/Yoichiro	302	composite	—
Frederika/Gabriel	266	composite	—
Lise/Enrico	306	composite	^{55}Fe source
Rita/Steven	310	composite	not working
TUM40/Michael	248	stick	—
TUM45/Oliver	248	stick	^{55}Fe source
TUM29/Thomas	299	carrier	^{55}Fe source
TUM38/Petrus	299	carrier	^{55}Fe source
VK27/Diogenes	197	beaker	^{55}Fe source
VK28/Zam	194	beaker	^{55}Fe source

out that by considering the surface roughness of materials in the simulations of these backgrounds, the resulting energy spectrum can mimic a dark matter signal [78].

The first two designs use a large carrier disc glued to the main absorber. The non-scintillating clamps then hold only the carrier crystal avoiding any direct line of sight between clamps and main absorber. One of those designs uses a standard SOS light detector and scintillating foil (*carrier*, see Fig. 3.10a) whereas the other employs a silicon beaker as light detector (*beaker*, see Fig. 3.10c) which completely covers the main absorber making the entire surface facing the absorber active. Both designs rely on the ability to discriminate events occurring in the carrier disc from events in the main absorber. The third design uses cubic crystals which are held by scintillating $CaWO_4$ sticks (*stick*, see Fig. 3.10e) which are pressed onto the crystal by bronze clamps outside the scintillating housing [79].

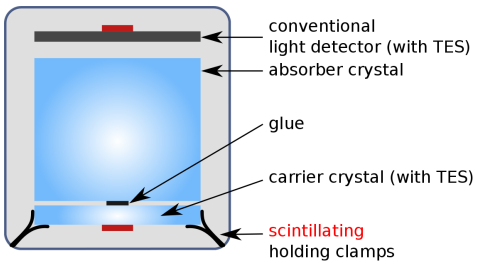

(a) Schematic drawing of the carrier design.

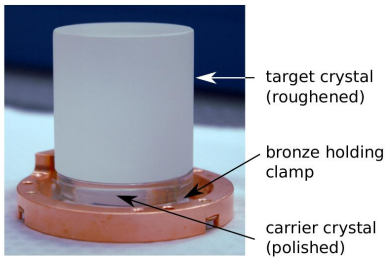

(b) Picture of a carrier design module.

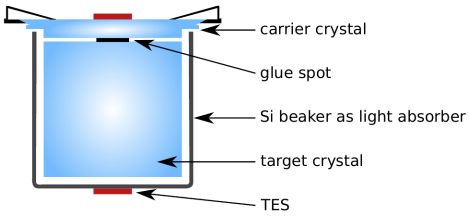

(c) Schematic drawing of the beaker design.

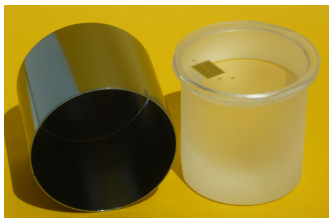

(d) Picture of a beaker design module.

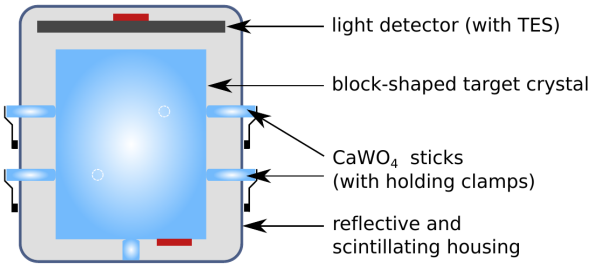

(e) Schematic drawing of the stick design.

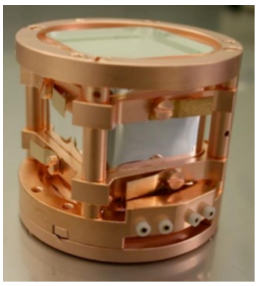

(f) Picture of a stick design module.

Figure 3.10: Schematic drawings and pictures of the novel detector designs used in run 33. (credit: CRESST collaboration)

Chapter 4

Data Analysis

In this chapter all necessary steps to arrive from the binary data recorded by the DAQ to the final calibrated data which can be used to extract physical parameters are explained. As a first step, the raw data is converted to a more convenient format. Then, several parameters are calculated for each pulse which can be used to classify them. A central part of the data reconstruction is of course the energy calibration, which involves fitting the pulses with signal templates to extract the amplitudes and linearizing the amplitude response with the help of pulses injected into the TES heater.

Finally, it has to be assured that the final data set contains only valid pulses by removing e.g. electronic artifacts and other pulses where an energy reconstruction is not possible. A special class of events which have to be removed are those originating in the small TES carriers. These events have a slightly different pulse shape compared to absorber events and machine learning methods are investigated to efficiently identify and reject these events. Also time periods where a stable operation of the detectors can not be guaranteed have to be removed. All cuts which remove unwanted events, might of course also remove some potential signal events. Therefore, in order to have an unbiased analysis, the energy-dependent signal acceptance for all cuts has to be estimated.

Another crucial parameter for low mass dark matter searches is the energy threshold of the phonon detectors, which can be determined from the trigger efficiency of heater pulses.

As explained in the previous chapter, the light yield of an event can be used to discriminate signal and background. To do so, the distribution of events in the energy-light yield plane has to be modeled. In this model, events belonging to each class of events are distributed in bands defined by the energy-dependent resolutions of the light and phonon detectors and the specific light output for the event class. The description of this model and the method for extracting

its parameters are presented.

Finally, the optimum interval method to calculate an upper limit in the presence of unknown background, which is used to set limits on the dark matter-nucleon cross section in the following chapter, is explained.

Most of the methods described in this chapter are also covered in previous work e.g. [73, 80, 81, 82]. Methods developed for the current run are in part also covered in [83, 84].

4.1 Raw Data Conversion

The DAQ system writes data to several binary files. The information and data relevant to a dark matter analysis are stored in the following files: RDT-files hold the pulse traces of the individual detectors, QDC files hold the pulse height data from the muon veto panels, CON-files store the control pulse heights and PAR-files store meta data about the corresponding RDT-file. At the start of each analysis the information in these files is read and converted to the HDF5 [85] format using PyTables [86], an open source package for Python providing additional indexing and compression features.

4.1.1 RDT-File

The RDT-file contains the pulse traces of the phonon and light detectors in a binary format. Each pulse record contains some additional information about the pulse which is stored together with the actual trace. The layout of these pulse records is described in the PAR-file where the number of signed integers, unsigned integers and floats in the header of each pulse record as well as the number of samples in each trace are defined. In run 33, which is analyzed in this work, each trace consists of 8192 samples recorded with a sampling rate of 25 kHz and a resolution of 16 bits for inputs ranging from -10 V to +10 V. This leads to a trace length of ~ 330 ms. The layout of a pulse record for run 33 is shown in Fig. 4.1. Besides the actual pulse trace, the information relevant for the analysis are the channel number which identifies the detector, the trigger delay which can be used to tell if a detector has triggered or not, the timestamp which is mainly used to search for coincident events in other detectors or the muon veto, the DAQ dead time which is needed to calculate the exposure and the test pulse amplitude (TPA) which identifies each pulse as particle pulse (TPA $= 0$), random trigger (TPA $= -1$) or test pulse (TPA > 0).

As can be seen in Fig. 4.1, there are two different timestamps for each record: one is defined as the UNIX timestamp of the DAQ computer (CPU time) and has a resolution of 1 μs, the other is derived from a 10 MHz clock

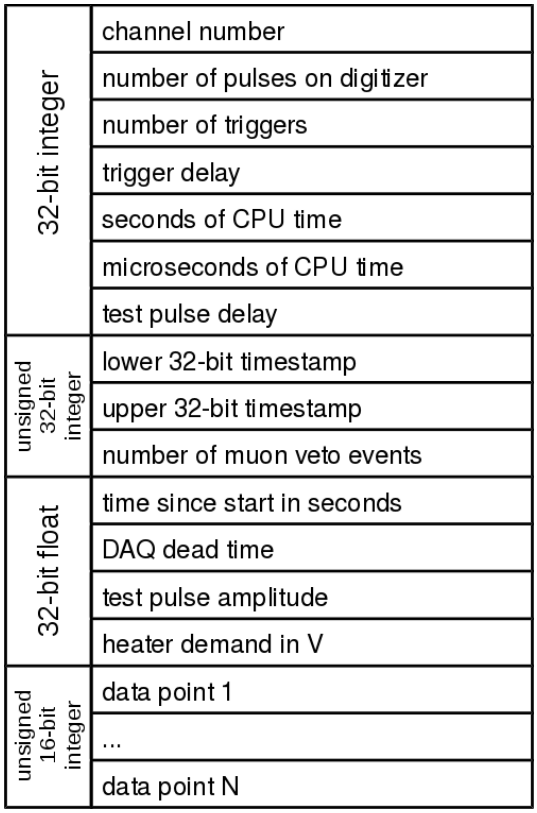

Figure 4.1: Structure of a pulse record in the binary RDT file which contains the data from the cryogenic detectors.

which synchronizes the different DAQ components and counts the number of clock cycles since the start of the file (with a resolution of 0.1 μs). For the relative timing of events in different detectors, the latter definition provides the higher precision and is thus used whenever this work refers to timestamps.

4.1.2 QDC-File

The QDC-file contains the data from the muon veto in binary format. Each veto record consists of a header and the actual veto data (see Fig. 4.2). The header contains the timestamp (derived from the 10 MHz clock) and the number of panels that are read out. For each of these panels a record containing the panel ID and the QDC reading follows the header. In addition to the 20 panels, there is also an analog sum which is read out every time.

4.1.3 CON-File

The CON-file contains the data from the control pulses in binary form. Unlike for particle and test pulses where the full pulse trace is recorded, only the

uint 32	lower 32-bit timestamp
	upper 32-bit timestamp
int 16	number of records (N)
uint 16	QDC value 1
	...
	QDC value N
	panel number 1
	...
	panel number N

Figure 4.2: Structure of a pulse record in the binary QDC file which contains the data from the muon veto.

int 32	channel number
float 32	pulse height
uint 32	lower 32-bit timestamp
	upper 32-bit timestamp
float 32	DAQ dead time
int 32	trigger delay

Figure 4.3: Structure of a pulse record in the binary CON file which contains the data from control pulses.

pulse height is stored for control pulses. In addition each control pulse record (see Fig. 4.3) consists of the channel number which is the same as in the RDT-file, the timestamp (derived from the 10 MHz clock), DAQ dead time and the trigger delay parameter which can be used to identify valid control pulses.

4.1.4 PAR-File

The PAR-file contains meta data about the corresponding RDT-file such as the start and stop times of the file, number of pulses recorded for each detector, information about which detectors are paired as a module as well as DAQ settings or names and masses of the individual detectors. The information is stored as a human-readable text file and can easily be parsed for the relevant information.

4.2 Energy Calibration

The most important parameter for any analysis is the energy deposited in the detectors, which can be derived from the signal amplitude. The first step in determining the energy is to fit a signal template to each pulse record which yields the amplitude of the pulse. The amplitudes are then linearized by evaluating a low order polynomial fitted to the amplitude response of heater pulses with different injected energies. Finally, the energy scale is set by determining the linearized amplitudes of events obtained by irradiating the detectors with a calibration source. Typically 122 keV γ-rays from a ^{57}Co source are used for the energy calibration. In the following, each step will be discussed in detail.

4.2.1 Determination of the Pulse Amplitude

For a TES, the amplitude response follows the shape of its transition curve. For small signals, where the transition curve is approximately linear, the pulse height is proportional to the deposited energy and the pulse shape is independent of the energy. For higher energies, the transition curve flattens and thus the pulse shape changes with energy and the pulse height no longer is proportional to the energy. This saturation effect limits the energy range of a TES if one uses only the pulse height to reconstruct the energy. One can, however, recover a much wider energy range by using not only the pulse height but the entire pulse shape and fitting a signal template to the data.

This method uses a signal template which is representative of the pulse shape in the linear regime of the TES (where the pulse shape is independent of the energy). These signal templates are generated by averaging a large number of pulses ($\mathcal{O}(100)$) selected by hand from the linear region of the TES to reduce the amount of noise. One has to take care to select only pulses with the same pulse onset, so the pulse shape does not get distorted. Therefore, usually pulses with the same amplitude are selected to minimize the influence of trigger-walk. Finally, the pulse height of the average pulse is normalized to one and the baseline is set to zero.

A linear least squares fit of this signal template $T(t)$ together with a baseline model $B(t;\vec{p})$ is then performed to the measured pulse data $S(t)$. The fit minimizes the RMS (cf. Eq. 4.1) and yields the amplitude A and the baseline parameters $\vec{p}$. Since the measured pulse may have a different onset than the signal template, a shift parameter t_0 is introduced which shifts the signal template relative to the measured pulse and the fit is performed for different values of t_0. The best fit is then obtained for the shift parameter which gives the lowest RMS value. To reduce computation time an efficient algorithm to find this minimum is used: the so-called golden section search, which is the

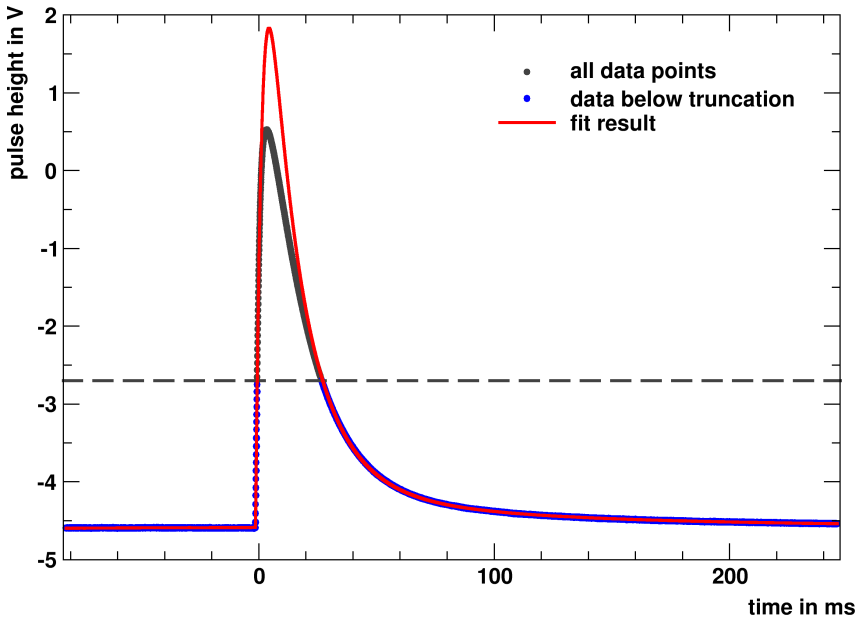

Figure 4.4: Data points (gray) of a particle pulse together with the result of the truncated template fit (red). Only data below the truncation level of 1.9 V above the baseline (dashed line) is used for the fit. The data points used for the fit are highlighted in blue.

optimal version of the Fibonacci Search [87, 88]. Shifting the pulse and template relative to each other reduces the number N of data points used for the fit because only the overlapping region can be used.

$$RMS = \sqrt{\frac{1}{N}\sum_{i=1}^{N}(S(t_i - t_0) - (A \cdot T(t_i) + B(t_i;\vec{p})))^2} \tag{4.1}$$

The baseline model $B(t;\vec{p})$ can in principle have any functional form. For this work, a third degree polynomial is used because it significantly improves the energy resolution at low energies compared to a constant or linear background model used in previous works.

In order to have a meaningful amplitude reconstruction also for larger signals, one can define a voltage above which the response is not considered linear any more and use only those data points for the fit which lie below this threshold (see Fig. 4.4).[1] This procedure is then called *truncated template fit* and effectively estimates the amplitude from the duration of the pulse. This method works well as long as the decaying part of the pulse fits in the predefined record length and is essential for the analysis of MeV events, e.g. α-decays. To determine the truncation level one can for example look at the

[1] This reduces the number of data points N in Eq. 4.1.

RMS values as a function of fitted amplitude for a fit without truncation. For amplitudes still in the linear regime, the RMS values remain approximately constant and there will be a sudden increase in the RMS once the amplitude response becomes non-linear.

Since the majority of the energy is detected in the phonon channel, the determination of the shift parameter is usually more accurate for the phonon detector. This is especially true for the lowest energies where the light signal might even become too small to detect. For this reason, the pulses of the two detectors in a module are usually not fitted independently of each other but a correlated fit is performed: one can either search for the shift parameter which minimizes the combined RMS of the two detectors, or - as done in this work - use the shift parameter determined for the phonon detector as input for the light detector fit.

Finally, some basic checks are performed for each fit to determine if the minimization of the RMS with respect to the shift parameter t_0 converged properly. This is done by looking at the RMS values obtained for the different shift parameters which are tested during the golden section search. There are three requirements which have to be fulfilled:

- the minimum RMS must not be found at the edges of the region in which the minimum is searched
- the minimum must be deep enough (minimum RMS must be less than 10 % of maximum RMS value)
- there must be a single minimum in the covered region

If one of these empirical criteria is not fulfilled, the fit is marked as bad and the corresponding event is discarded.

4.2.2 Heater Pulses

As pointed out before, the response of the TES can not be assumed to be linear. To correct for these non-linearities, signals with known energy are required. The standard procedure for radiation detectors would be to use different radioactive sources with energies spanning the relevant energy range, i.e. 0-40 keV. However, sources with such energies cannot penetrate the walls of the cryostat and would have to be positioned inside the cryostat, which is not an option. To circumvent this, each TES is equipped with an ohmic heater into which pulses with a predefined energy and pulse shape can be injected (cf. Sec. 3.2.1).

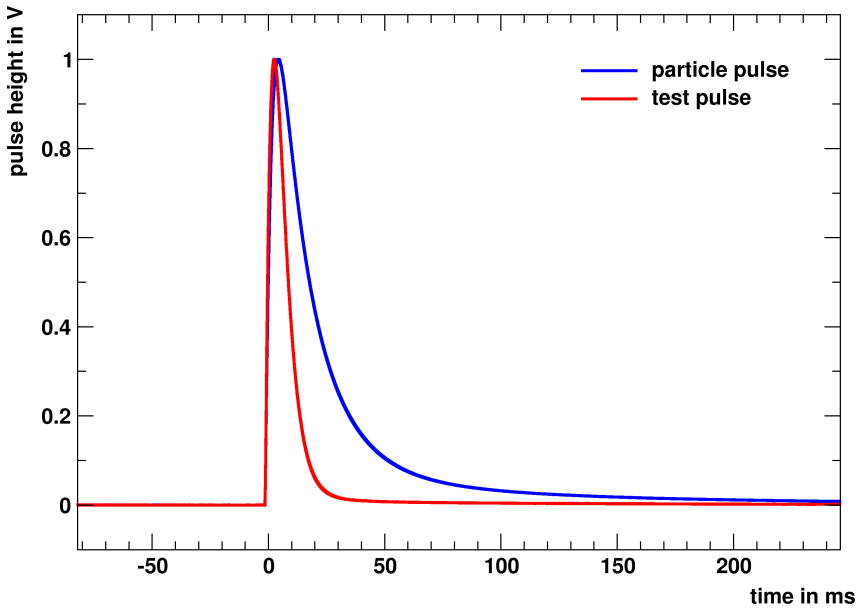

Figure 4.5: Pulse shape of a particle pulse (blue) and a test pulse (red). Test pulses have a deliberately shorter decay time which reduces the probability of pile-up with subsequent particle pulses, especially for large test pulse amplitudes.

Throughout the entire data taking period pulses with different amplitudes (the so-called test pulses) are injected into the heater. The DAQ system records the injected amplitude of these test pulses (the so-called test pulse amplitude or TPA) together with the pulse trace, which allows to identify test pulse events. The TPAs range from 0.002 V to 3 V which corresponds to energies between $\sim$ 400 eV and $\sim$ 600 keV (depending on the calibration factor of the detector which is typically around 200 keV/V). The full list of injected TPAs is compiled in Tab. 4.1. This list is cycled periodically with test pulses being injected in 30 s intervals (i.e. 6 minutes for a complete cycle).

The pulse shape of these events is chosen to be as similar as possible to that of particle events. Differences, however, remain (see Fig. 4.5) and so the test pulse events have to be fitted with a different signal template than particle events. This template is generated from test pulse events with a pulse height close to those events used to create the particle template. The relationship between fitted amplitude and TPA can then be used to linearize the detector response by fitting a low order polynomial to the data. The same response function is then applied to the fitted amplitudes of the particle events, which yields the so-called test pulse equivalent amplitudes (see Fig. 4.7).

The response of the detector is sensitive to changes in its operating point. Despite being stabilized with control pulses (cf. Sec. 4.3.2), the operating

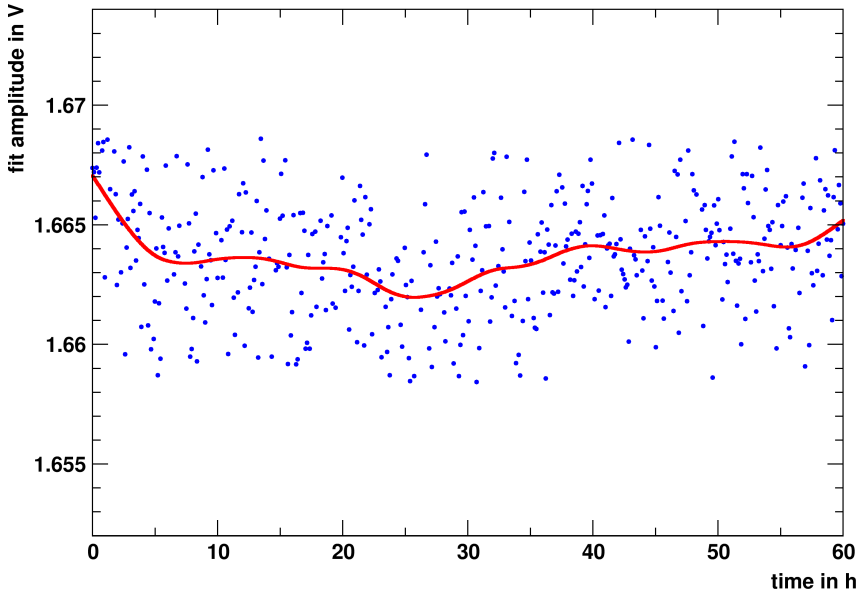

Figure 4.6: Smoothing spline (red curve) fitted to the amplitudes of test pulse events (black) over time for a single test pulse amplitude.

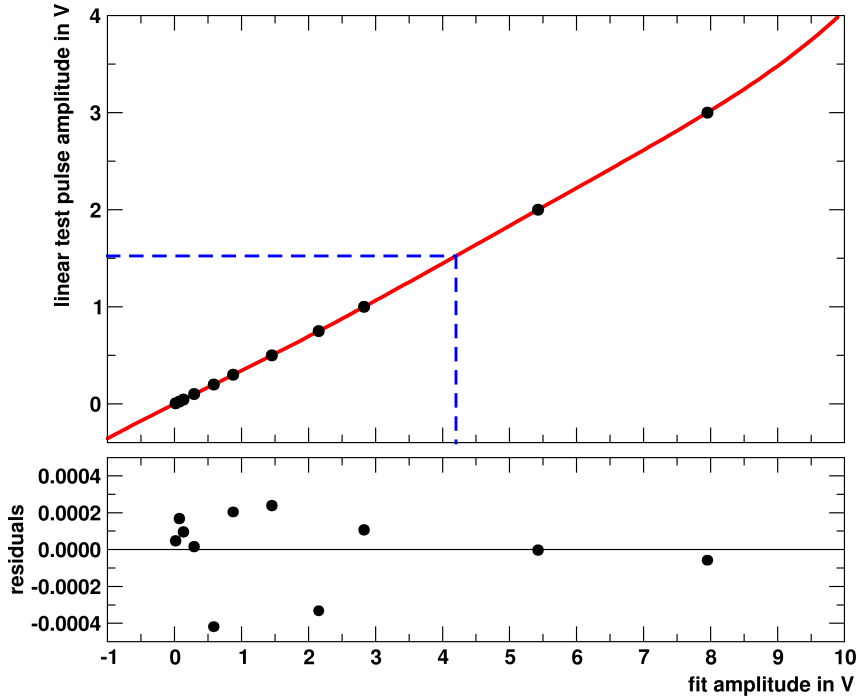

Figure 4.7: The top panel shows the amplitude of test pulse events (as extracted from the fitted splines) plotted against the value of the test pulse amplitude (black dots). A polynomial fitted to these points (red curve) is used to convert the reconstructed amplitude of a particle event into a linearized scale as indicated by the dashed blue lines. This linearized scale is finally multiplied with a calibration factor to get the deposited energy. In the bottom panel, the residuals of the fit are displayed.

Table 4.1: List of injected test pulse amplitudes and corresponding energies for a typical detector with a calibration factor of $\sim 200\,\mathrm{keV/V}$.

TPA in V	E_{inj} in keV
0.002	0.4
0.003	0.6
0.005	1
0.025	5
0.045	9
0.1	20
0.2	40
0.3	60
0.5	100
0.75	150
1	200
2	400
3	600

point may drift slightly over time. To correct for such possible drifts, one can exploit the time information of the test pulse events. This is done by fitting a smoothing spline to the fitted amplitudes of each TPA over time (see Fig. 4.6) and evaluating these splines at the time of each particle event to obtain the calibration polynomial at the given time. This method is only able to correct small drifts of the operating point, larger excursions will lead to a wrong energy reconstruction and have to be identified and removed from the data set (see Sec. 4.3.2).

4.2.3 ^{57}Co Calibration

To convert the test pulse equivalent amplitudes, which should now be linear, to the deposited energy one needs only one reference point. Ideally one would like that reference to be close to the energies of interest (below 40 keV). This is, however, not feasible because the cryostat can not be penetrated by γ-rays with such low energies. As a compromise, the 122 keV line of ^{57}Co has been chosen. At the beginning of each data taking period, dedicated calibration data are taken with one or more ^{57}Co sources in different positions to acquire sufficient statistics for each detector module. The fitted position of the 122 keV line A_{122} - in units of test pulse equivalent amplitude A - is then used to convert to deposited energy according to the following relation:

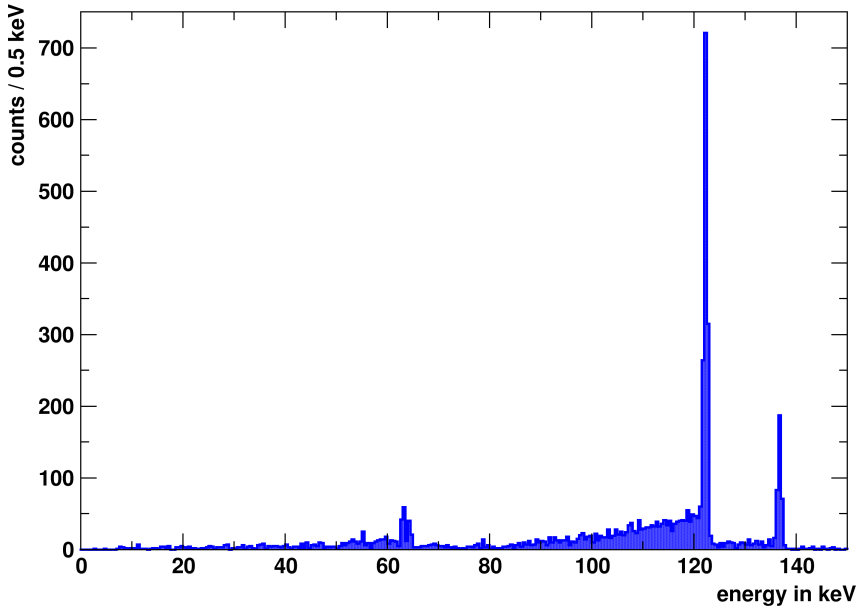

Figure 4.8: Energy spectrum of a calibration run with a ^{57}Co source for TUM40. Clearly visible are the γ-lines at 122 keV and 136.5 keV. The feature around 60 keV is due to tungsten x-rays escaping the detector.

$$E_{dep} = \frac{122 \text{ keV}}{A_{122}} \cdot A = c \cdot A \tag{4.2}$$

where c denotes the calibration factor. A calibrated spectrum of one of the detectors is shown in Fig. 4.8.

4.2.4 Correlation Between Phonon and Light Energy

There exists a small correlation between the measured phonon and light energies which makes mono-energetic γ-lines appear tilted in the energy-light yield plane (see Fig. 4.9). This leads to a degraded energy resolution in the phonon channel which is of course undesirable. The reason for this effect is that the total deposited energy E_{tot} is shared between the phonon and the light channel with most of the energy going in the phonon channel E_p and only a small fraction η in the light channel E_l:

$$E_l = \eta E_{tot} \tag{4.3}$$

and

$$E_p = (1 - \eta) E_{tot} \tag{4.4}$$

The energy scale is set with events that have a light yield of 1. For events with a lower light yield, more energy is deposited in the phonon channel which

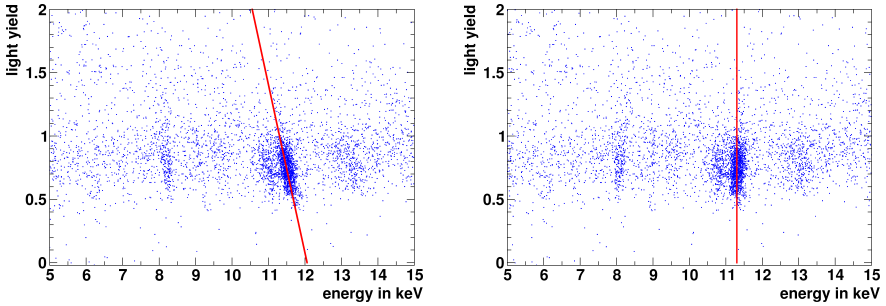

(a) Energy-light yield plot before correction. The line at 11.3 keV appears tilted. The red line indicates a tilt with $\eta = 0.067$.

(b) Energy-light yield plot after correction. The line at 11.3 keV now appears straight. The red line indicates zero tilt.

Figure 4.9: Illustration of the effect of the correlation between energy detected in the phonon and light channels.

leads to a higher energy assigned by the energy calibration. The energy assigned by the calibration procedure can be written as

$$E_{tot} = c_p E_p \Rightarrow E_p = \frac{E_{tot}}{c_p} \tag{4.5}$$

and

$$E_{tot} = c_l E_l \Rightarrow E_l = \frac{E_{tot}}{c_l} \tag{4.6}$$

with the calibration factors c_p and c_l.

Comparing the two sets of equations, one finds that

$$c_p = \frac{1}{1-\eta} \tag{4.7}$$

and

$$c_l = \frac{1}{\eta} \tag{4.8}$$

Requiring that $E_{tot} = E_p + E_l$ leads to the following relation which can be used to correct the reconstructed energies:

$$E = \eta E_l + (1-\eta)E_p = [1 - \eta(1 - LY)]E_p \tag{4.9}$$

where LY denotes the light yield of the event.

The value of η for a specific detector can be obtained by fitting the tilt of the observable γ-lines. Typical values obtained by this method are $\mathcal{O}$(1-10 %). The validity of this approach can be cross-checked by looking at the energies of α-events, which have a light yield of ~ 0.25 [89].

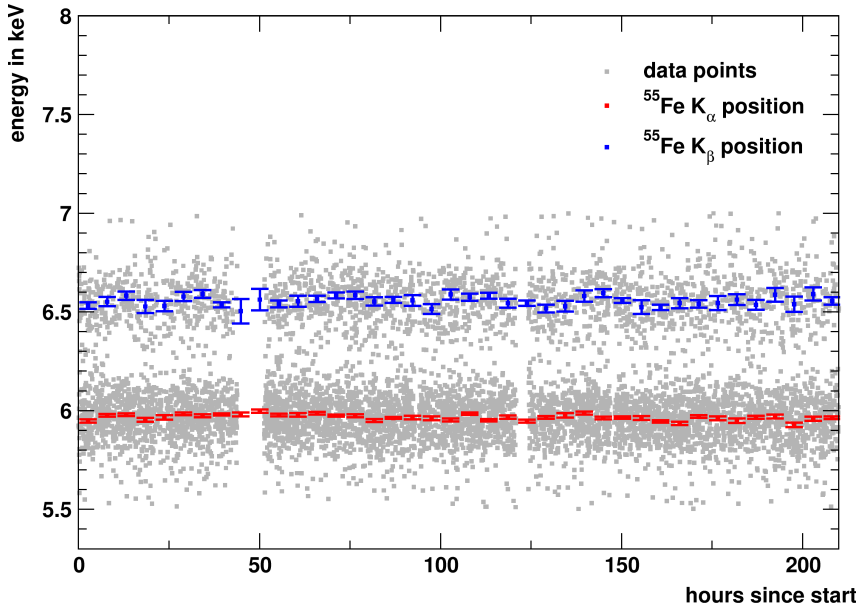

Figure 4.10: Fitted peak positions of the K_α (red) and K_β (blue) lines of an ^{55}Fe source over time for detector Lise. Shown in gray is a scatter plot of all data points in the relevant energy range. The constant width of the distribution of these events demonstrates the stability of the energy resolution.

4.2.5 Longterm Stability

Since data is taken over the period of almost two years, the longterm stability of the energy calibration has to be guaranteed. One way to check this is to repeat the ^{57}Co calibration during the run. Since this is a rather complicated procedure which involves the opening of the shielding, this is only done once at the end of the run. Another option is to use γ-lines visible in the background spectra. Here the problem is that the intensity has to be large enough so sufficient statistics can be acquired in small time periods. In this run, the misalignment of an ^{55}Fe source intended to calibrate one of the light detectors led to the accidental illumination of the phonon detector Lise. The fitted peak positions of the K_α and K_β lines can be used to check the longterm stability of the energy calibration at low energies. The result is shown in Fig. 4.10 where one can see that the positions of both lines remain constant (within $<1\,\%$) over the entire time. In addition to the fitted peak positions, which are shown in red and blue, also a scatter plot of all data points in the relevant energy range is shown. The constant width of their distribution demonstrates that also the energy resolution remains stable over time.

4.3 Data Selection

4.3.1 Data Quality Cuts

For some recorded pulses a correct energy reconstruction is not possible, thus they have to be discarded. Fig. 4.12 shows exemplary pulses of different classes of such events. To clean the dataset from these unwanted pulses, a set of parameters such as peak position, pulse height, etc. are calculated from the pulse traces. These parameters are then used to define cuts which remove unwanted events. In the following, the parameters relevant for the dark matter analysis are discussed.

The *pulse height* and *peak position* are calculated as the maximum and its position of the pulse trace after applying a moving average filter with a length of 50 samples (corresponding to 2 ms). The *peak onset* is found by going backwards from the position of the maximum until the signal is below the FWHM of the baseline, which is calculated from the pre-trigger region of the pulse trace (i.e. the first 25 % of the trace). The difference between *peak position* and *peak onset* is called *peak position minus onset* or *PMO* and is a measure of the rise time of the pulse. For low energies it is usually more accurate than the 10-50 % or 10-70 % rise times which are also calculated.

Another parameter which is useful to detect e.g. SQUID resets, flux quantum losses or decaying baselines (see Fig. 4.12) is the *baseline difference* parameter, which is simply the difference between the average of the last 50 samples and the average of the first 50 samples of a pulse trace. These events can be removed by requiring that the baseline levels at the beginning and end of the trace are similar. For small signals the baseline difference of valid pulses is close to zero. When the signals become larger the pulses do not fully decay within the record length anymore leading to a positive difference which depends linearly on the pulse height (see Fig. 4.13c).

Although the trigger rate is rather low, there is still a finite probability to observe two pulses in one trace. Reconstructing the amplitude of these pile-up events is complicated and since the removal of pile-up events introduces negligible dead time they are simply removed. In order to detect pile-up events the so-called *pile-up voltage* parameter is calculated. For this the global maximum of the trace is considered to be the main pulse of the event. Starting from the position of this global maximum obtained above, the algorithm searches for the largest difference between a local minimum and any following local maximum (see Fig. 4.11).[2] If there is only a single pulse, the calculated difference

[2]This assumes that the main pulse occurs first. Since in the case of pile-up, the main pulse can also occur later in the trace, the algorithm searches also for the largest difference between a local minimum and any preceding local maximum before the main pulse.

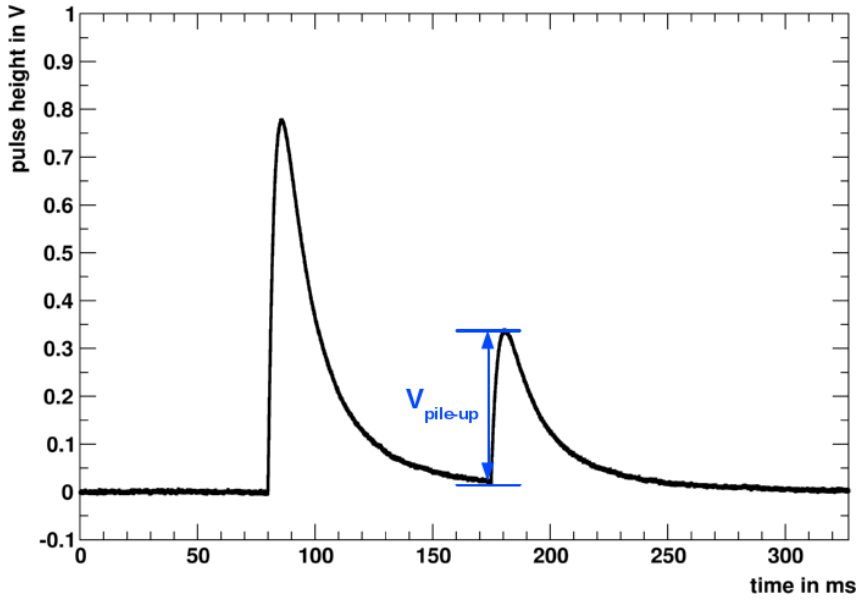

Figure 4.11: Illustration of the pile-up voltage parameter $V_{pile-up}$.

will be very small (on the order of the baseline fluctuations). In the case of pile-up, however, the difference will be large (approximately the pulse height of the second pulse). This allows to efficiently remove pile-up events.

Occasionally, sharp negative spikes occur in the data which are caused by interferences in the electronics. These may affect the reconstructed amplitude and thus have to be discarded. To reject these spikes resembling a delta function, the so-called *delta voltage* parameter is calculated. It is defined as the difference of the minimum pulse height and the pulse height of the sample just before. Occasionally the rise time of these spikes spans two data samples, so if the difference to the pulse height two samples before the minimum is larger, this is taken instead.

The remaining unwanted events are removed by a cut on the *template RMS* (cf. Sec. 4.2.1) which is large for pulses with a pulse shape different from the signal template. For large signals, the RMS increases with pulse height requiring an energy dependent cut. In Fig. 4.13 the energy dependent cut limits for the four parameters are shown using the example of the phonon detector TUM40.

4.3.2 Stability Cut

For a correct energy reconstruction it is essential that the detector remains in its specified operating point. The calibration procedure manages to correct for small drifts in the operating point by taking the test pulse response over time into account. Significant short term departures from the operating point, due

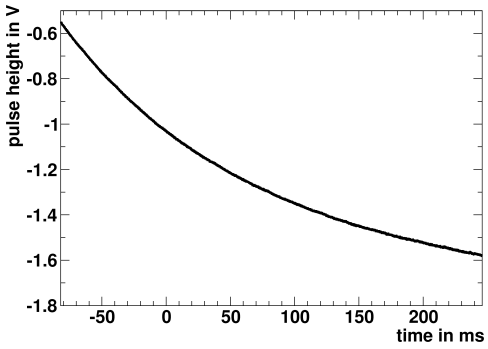

(a) Decaying baseline. These occur when the decaying part of a large pulse is still large enough to cause a trigger if it is unblocked after readout.

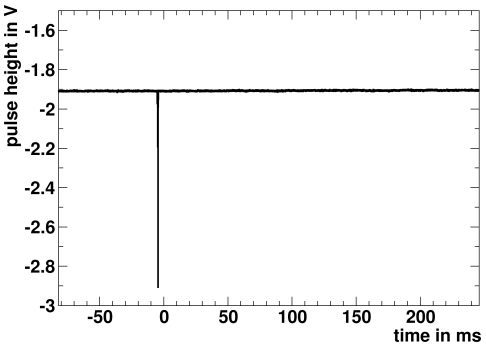

(b) Delta spike. These are caused by electrical interference and can easily be removed.

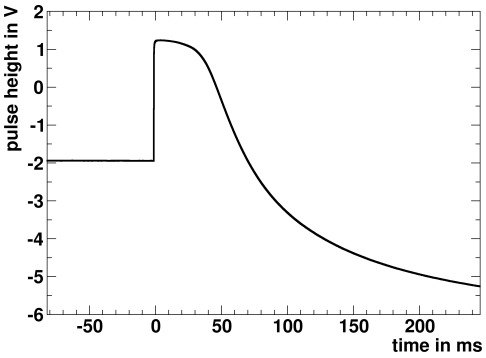

(c) Flux quantum loss. If the signal rise time is too fast, the SQUID readout can not follow quickly enough and a flux quantum is lost resulting in a lower baseline.

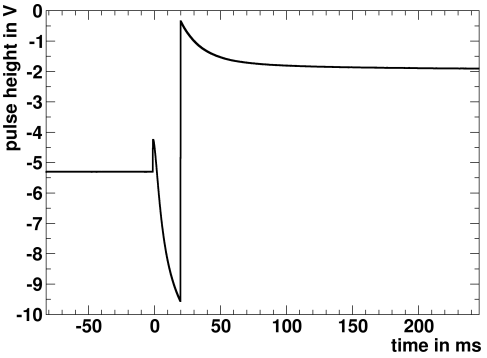

(d) SQUID reset. If the SQUID output is outside the dynamic range of -10 to 10 V, the baseline is reset to a predefined value.

Figure 4.12: Example of unwanted pulses which do not allow a correct energy reconstruction and have to be removed.

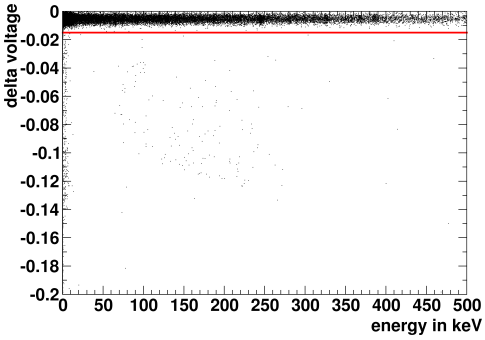

(a) Delta voltage vs. energy (black dots). Events between the red lines are accepted as valid pulses.

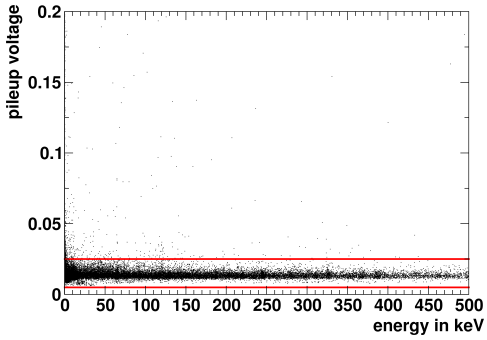

(b) Pile-up voltage vs. energy (black dots). Events between the red lines are accepted as valid pulses.

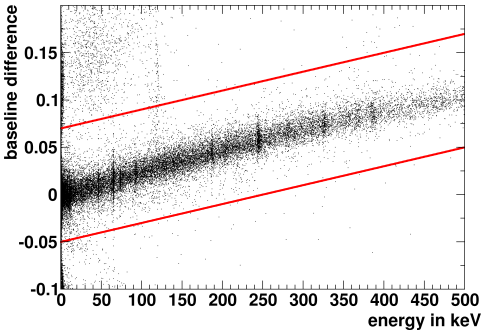

(c) Baseline difference vs. energy (black dots). Events between the red lines are accepted as valid pulses.

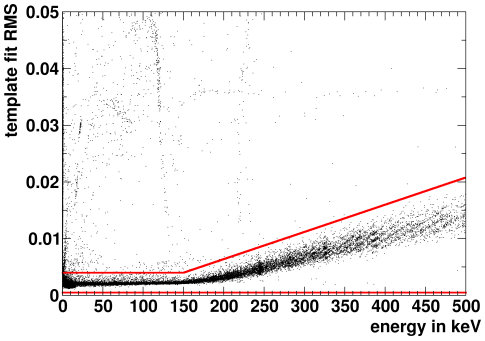

(d) RMS of template fit vs. energy (black dots). Events between the red lines are accepted as valid pulses.

Figure 4.13: Energy dependent cut limits for detector TUM40.

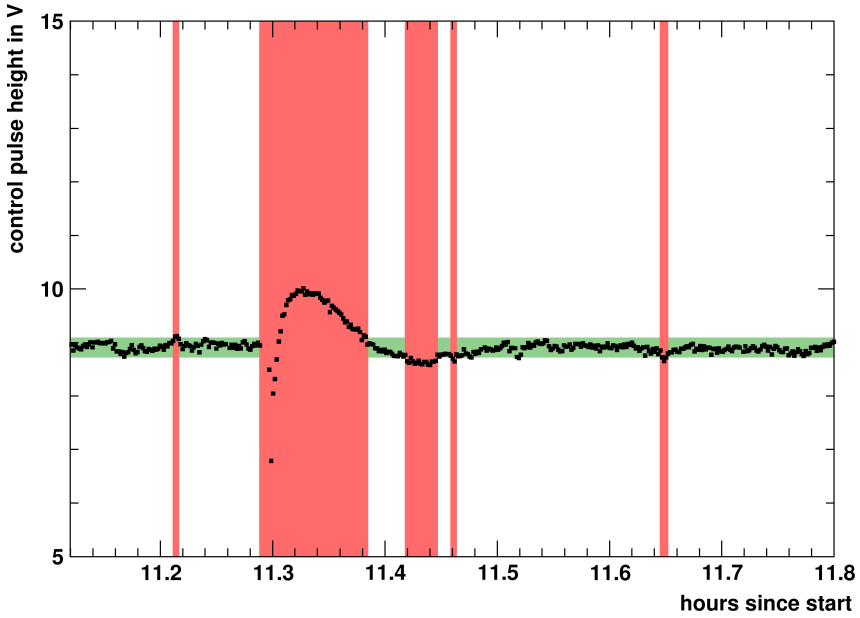

Figure 4.14: Control pulse height data plotted against time (black dots). The green band indicates the range of control pulse heights which is considered stable. The time periods shaded in red are removed by the stability cut since the control pulse heights lie outside the stable region.

to mechanical vibrations e.g., however, can lead to mis-reconstructed energies which has to be avoided. To detect these deviations, one can look at the pulse height of the control pulses. Control pulses are essentially test pulses with a large amplitude guaranteed to saturate the TES thus measuring the distance of the operating point to the top of the transition curve. The temperature of the TES is regulated such, that this control pulse height corresponds to a predefined set point. If the detector is not in its correct operating point the control pulse height differs from this set point value. Such periods are detected by the so-called stability cut and events in these periods are flagged as unstable and discarded. This is illustrated in Fig. 4.14.

First, one has to check if the pulse height belongs to a valid control pulse. This can be done by looking at the trigger delay parameter which measures the time between injecting the control pulse and the firing of the trigger. If this is not within the main distribution the pulse height might be affected by a particle pulse occurring simultaneously and the control pulse has to be discarded. Then a window is defined by looking at the distribution of valid control pulse heights which defines the range for stable control pulses. Pulses outside this window are considered unstable. In order to consider a period as unstable, at least two consecutive control pulses are required to lie outside the stable range. This condition makes the cut more robust, since single excursions

can happen quite frequently (e.g. due to pile-up or electronic artifacts) and might not be connected to a shift in the operating point. In addition, periods with no valid control pulses are also discarded since it can not be guaranteed that the detector is in its correct operating point.

Once one of these conditions is fulfilled, the entire period between the last stable pulse before and the next stable pulse after it is declared unstable. All recorded pulses in this time period are flagged as unstable and the entire time is added to the dead time. When calculating the dead time one has to be careful to not double count the DAQ dead time which is already considered by the DAQ system.

4.3.3 Anti-Coincidence Cuts

The low interaction probability of dark matter particles rules out the possibility that such a particle deposits energy in more than one detector module. This can be exploited to remove background events which cause coincident signals in more than one module. Also signals coincident with the muon veto can be discarded. To do so, a time window has to be defined where true coincident events are expected. This can be done by looking at the time difference between events in different detectors: if the events are uncorrelated, the distribution of these time differences is flat, if there are true coincidences, one observes a peak. The width and position of this peak then defines the coincidence time window (see Fig. 4.15). For the anti-coincidence cut all events with a time difference between -10 and 10 ms are discarded, the time window for the muon cut spans from -4 to 1 ms.

The anti-coincidence and muon cuts introduce additional dead time, since for every trigger of the muon veto or other detector modules a coincident event would be discarded. As an estimate of this dead time, the probability for a random coincidence between an event in one detector and events in the muon veto or in any of the other detectors is calculated. This probability is then taken as the fraction of the live time which is removed by the respective cut. Assuming the events are uncorrelated, the probability p_{random} for random coincidences follows from Poisson statistics as

$$p_{\text{random}} = \left(1 - e^{-\Delta T \cdot R}\right) \tag{4.10}$$

where ΔT is the length of the coincidence time window and R is the rate of the potentially coincident pulses (muon veto or other detectors). Taking $\Delta T = 20\,\text{ms}$ and $R = 1.2\,\text{s}^{-1}$ for the anti-coincidence cut leads to a dead time fraction of 2.4 %. For the muon cut taking $\Delta T = 5\,\text{ms}$ and $R = 25.4\,\text{s}^{-1}$ yields a dead time fraction of 11.9 %. This rather high value for the muon cut is a

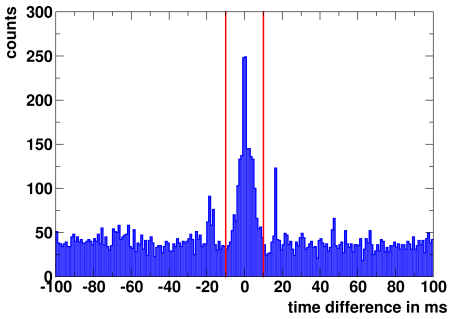

(a) Histogram of time differences between pulse onset in one detector module and pulse onset in other detector modules. The red lines indicate the time window chosen for the coincidence cut.

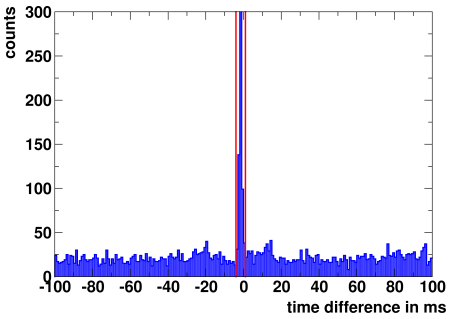

(b) Histogram of time differences between pulse onset in one detector module and timestamp of events in the muon veto. The red lines indicate the time window chosen for the muon veto cut.

Figure 4.15: Selection of time windows for coincidence and muon veto cut.

consequence of the high trigger rate of the muon veto in this run. The trigger rate was deliberately increased compared to previous runs by lowering the trigger thresholds of the individual panels so that they occasionally trigger in the baseline noise. Since the panels are read out by a QDC, which integrates the charge over a predefined time window, the position of the noise peak (sometimes called pedestal) is needed to compare the values between different panels and monitor the gain of the system. Since the total rate of $\sim 25\,\mathrm{s}^{-1}$ is much higher than the expected muon rate underground, the vast majority of coincidences are expected to be random and not caused by a muon. The dead time due to the muon cut could thus be reduced by selecting only muon events in the muon veto data. Such a selection would, however, potentially lower the efficiency of detecting muons and since most of the analyses in this work are not limited by the accumulated exposure, but by the residual background, the higher dead time is deliberately accepted in favor of removing muon coincident events with higher certainty.

4.3.4 Estimation of Cut Acceptances

Unlike the cuts which remove entire time periods, like the stability cut and the anti-coincidence cut mentioned above, cuts removing individual events may introduce systematic effects. Notably a dependency of the cut acceptance on the deposited energy. These effects must be studied and quantified in order to have an unbiased analysis. The method to determine the energy dependent cut acceptance, which was developed for this run, is based on artificial pulses

generated by superimposing the respective signal template - scaled to correspond to the desired energy - onto an empty baseline recorded by a random trigger.

The pulses obtained by this method are then processed by the same data analysis steps as real pulses, calculating the same parameters and performing the identical template fits. The resulting parameter distributions are then compared to those from real data. It has been found that the distributions agree very well for smaller energies, where the detectors are operated in the linear regime. At higher energies where non-linearities start to play a role the distributions show a poorer agreement since these non-linearities are not taken into account when generating the artificial pulses.

The energy-dependent cut acceptance is then determined by applying the same cuts used for the real data to the artificial data[3] and counting the number of artificial events surviving all cuts and comparing them to the number of generated events at any given energy.

4.3.5 Events induced in the TES carrier

In the earlier phases of the CRESST experiment, the TES have been directly evaporated on the absorber crystals. This, however, leads to difficulties in the production process due to the extended height of the crystals. In addition, the optical properties, especially the light output of the $CaWO_4$ crystals, suffer from the high temperatures needed for evaporation of the tungsten films. To alleviate these problems, the TES are now mostly evaporated on smaller carrier crystals which are subsequently glued to the absorber crystals. The increased light output and ease of manufacturing come, however, with the downside that events induced in the carrier crystal need to be discriminated from events in the absorber crystal. Also, two of the novel designs (the *beaker* and *carrier* designs, cf. Sec. 3.2) rely on the ability to identify events in the large carrier crystals to veto backgrounds related to α-decays on non-active surfaces. A potentially dangerous issue is the occurrence of events without associated light production due to stress relaxations at the carrier absorber interface. Such events would pose a serious background for dark matter searches, since they are indistinguishable from recoils off tungsten nuclei at low energies.

Events induced in the carrier generally feature faster rise and decay times due to the smaller dimensions of the carrier. This difference in the pulse shape (see Fig. 4.16) can be exploited to discriminate carrier and absorber events. This discrimination is usually very efficient. Only for the lowest energies $\lesssim 5\,\mathrm{keV}$ the efficiency degrades, posing a problem for low mass dark

[3] If applicable.

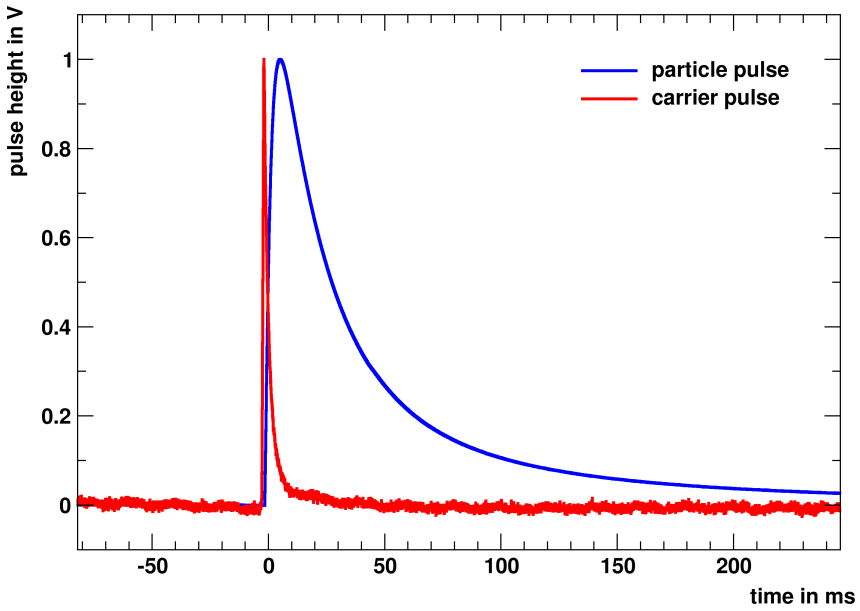

Figure 4.16: Pulse shape of particle event (blue) and carrier event (red).

matter searches.

If the carrier pulses rise significantly faster than the absorber pulses it can be sufficient to do a cut on the rise time of the pulse to remove carrier-like events. To improve the discrimination efficiency there exist additional, more sophisticated methods. One of them is to perform a template fit with a signal template generated from carrier pulses, which are selected by eye, in addition to the absorber template fit. One can then look at the fit parameters, especially the respective RMS values, to separate the two event classes.

Wavelet Decomposition

Another method, developed in this work, is based on the wavelet decomposition of the recorded signal and is based on the ideas in [90]. The wavelet transform is somewhat analogous to the Fourier transform in that it decomposes a time-series signal into its frequency contents. The wavelet transform, however, also conserves some timing information, whereas the Fourier transform dismisses the timing information completely to achieve the optimal frequency resolution. Retaining both frequency and timing information is impossible due to the uncertainty principle. The way the wavelet transform achieves to cover both timing and frequency information is to decompose the original signal with varying frequency resolution at different time-scales, where the frequency resolution gets worse for shorter time scales. This is done by scaling and shifting the original mother wavelet. For a mathematical introduction to wavelet transforms see e.g. [91].

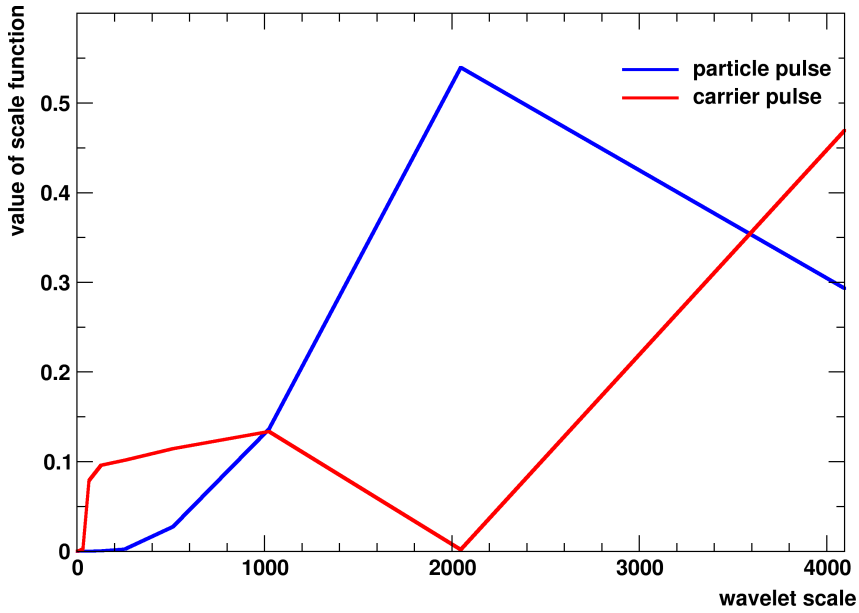

Figure 4.17: Value of scale function at different scales for particle template (blue) and carrier template (red).

For digitally sampled signals one applies the Discrete Wavelet Transform (DWT) which uses a discrete set of scaling factors[4]. In [90] a so-called scale function is defined which can be interpreted as the signal content at a given scale. Signals with different rise and/or decay times have different values for the scale function at different scales. As an example, the scale functions of the particle and carrier templates depicted in Fig. 4.16 are shown in Fig. 4.17. The distributions of these scale function values at different scales can be used to discriminate signals with differing pulse shapes. This is illustrated in Fig. 4.18 where the two event classes can be well separated using only two wavelet scales.

4.3.6 Carrier-like Events in TUM40

In the sample of events in the module TUM40/Michael surviving all data quality cuts, there is a huge population of events at low energy and low light yield which exhibit a phonon pulse shape similar to carrier events. The total rate of these events, however, is much larger than expected from the volume ratio between carrier and absorber crystal, which is unlike in other detectors where these ratios usually agree. The exceptionally high rate of these events indicates an origin different from the carrier crystal. Possible sources could be mechanical stress at the stick-absorber interface or stress relaxation at the glue spot of the small carrier. Similar events without light emission have

[4]This work uses the DWT implementation included in the PyWavelets package [92].

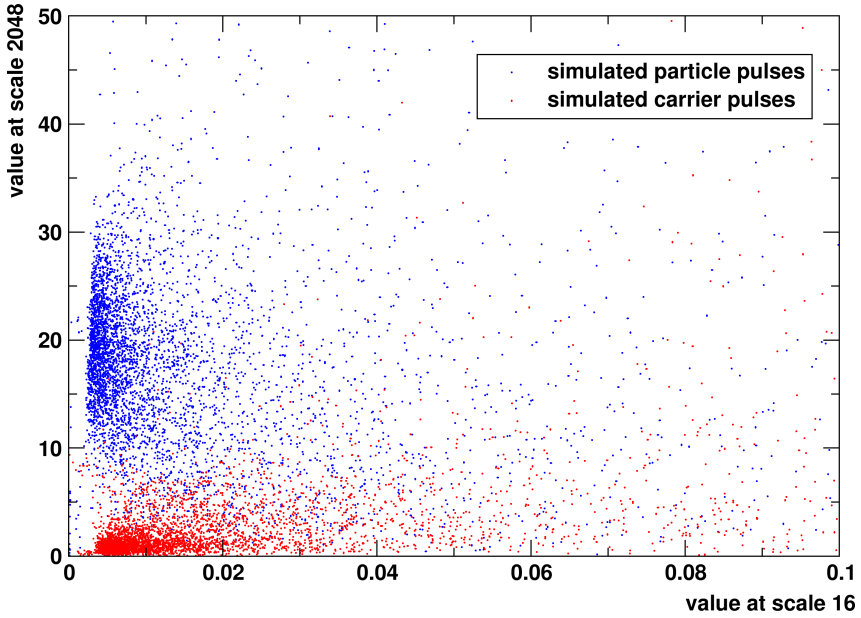

Figure 4.18: Values of the scale function at two different scales (16 and 2048) plotted against each other for a number of artificially generated particle (blue) and carrier (red) pulses. This shows the ability to already discriminate the two pulse shapes using only two different wavelet scales.

been observed in the past when the absorber crystal was in contact with non-metallic surfaces. This assumption is supported by the time structure of these carrier-like events which shows a rate which initially decays on the time scale of ~ 100 days (see Fig. 4.19). This resembles the behavior observed previously with no-light events. The bursts in the observed rate of these carrier-like events in the last third of the run are further evidence against a particle origin of these events and point more toward mechanical disturbances.

Since the rate of these events is orders of magnitude higher than usual carrier events, special effort has to be made to efficiently remove these events. In particular, any cut to remove these events needs to have a very low false positive rate which has to take preference over a high acceptance. A simple cut on the rise-time or the RMS ratio, which is usually sufficient to remove carrier events, would in this case have to be very aggressive, leading to very low acceptance at lowest energies. Instead, significant improvements can be made by taking multiple parameters into account. Machine learning methods, such as neural networks, support vector machines or decision trees, are perfectly suited to tackle such a binary classification problem. An introduction to machine learning methods can be found e.g. in [93].

In this work, a Random Forest (RF) classifier is used to discriminate carrier-like events and particle events. A RF is an ensemble classifier which uses the

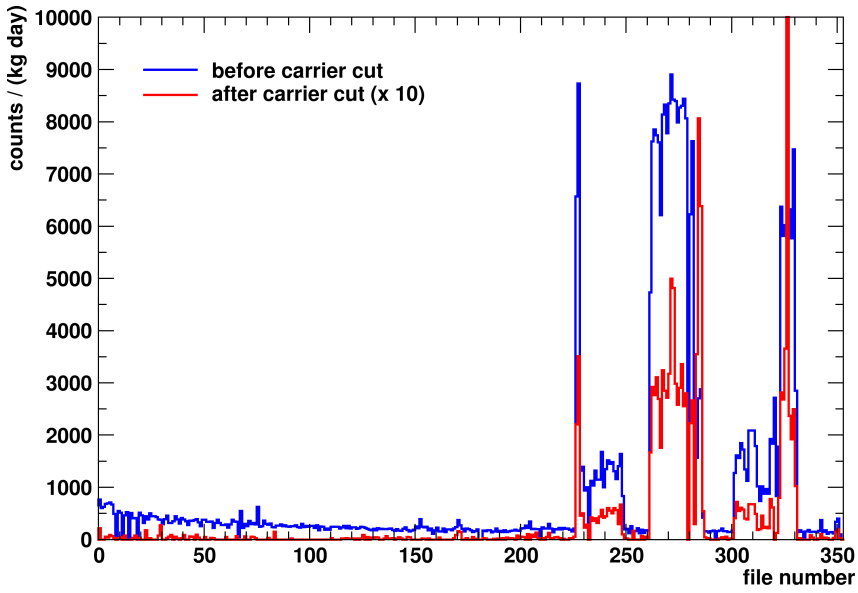

Figure 4.19: Rate of all events between 0.4 and 1.0 keV passing data quality cuts before (blue) and after (red) the RF cut to remove carrier like events for each file. The rate of events after the carrier cut is scaled by a factor of 10. The rate before carrier cut decreases exponentially until around file 200, which is when the threshold is reduced to 400 eV. Afterwards, several spikes in the count rate occur. During these spikes also the rate after carrier cut is exceptionally high.

output of an ensemble of classifiers to reach a decision. The idea behind using the combination of several classifiers is, that although each individual classifier might not be particularly good at classifying all the events, their combination might actually be more powerful than a single good classifier, since different classifiers might pick up different features in the data. Another advantage is that it can be computationally more efficient to train a large number of *weak* classifiers than one *strong* classifier, especially if parallelization is taken into account.

In the case of a RF the base classifiers are decision trees (hence the name forest). Decision trees employ a series of simple threshold cuts. At each step, one of the data features which are fed into the classifier is chosen at random and a threshold is set to divide the data in two classes. This is repeated after each step with all subsets. This causes the number of branches to double with each step, leading to a structure which resembles a tree. To achieve optimal classification, the classifier is trained with labeled data, i.e. data for which the correct classification is known. For this data, the selection of features and the different threshold values are varied so that the resulting classification matches the preassigned labels as closely as possible. In addition, some parameters of

the decision tree can be adjusted, e.g. the number of branches or the number of features used. These parameters can be used to find a compromise between computing power and accuracy. The same holds for the RF classifier, where e.g. the number of decision trees can be adjusted.

The RF implementation used in this work is included in *scikit-learn* [94], an open source package for Python which provides a unified framework for a variety of machine learning methods. To train the RF classifier, a large number of events ($\mathcal{O}$(100,000)) is generated for both carrier and particle pulses, applying the same method as for the determination of the cut acceptance (cf. Sec. 4.3.4). The carrier template used to generate these events is created from a sample of carrier-like events selected by eye. The parameters which are used to train the RF classifier are the values of the scale functions of the wavelet decomposition (cf. Sec. 4.3.5), the shift, amplitude and RMS of both the carrier and particle template fits and the rise time (peak position minus onset). Since all the parameters used for classification exhibit a rather strong dependence on energy, the energy range where the classifier is trained and applied is restricted to energies below 5 keV, where the classification with the standard methods becomes difficult. Above 5 keV the cut on the rise time (peak position minus onset) is used and efficiently removes all carrier-like events.

To assess the performance of the classifier, the artificial data set is randomly split into a training set (20 % of the data) and a testing set (80 % of the data). The classifier is trained on the training data and its performance is evaluated on the larger testing set. This is necessary to ensure that the classifier generalizes well to unseen data. Evaluating the performance on the data used for training usually gives a too optimistic picture of the performance. In the most extreme case, the classifier learns to identify each single event and fails completely to classify unseen events. This is a general problem in machine learning called *over-fitting*. To ensure that the performance does not depend on one specific split between training and testing set, one can employ so-called *cross-validation*. This entails that the random splitting in training and testing set is repeated multiple times and an average performance score is computed, which is then used to select the best classifier.

The final classifier selected after cross-validation achieves a fraction of correctly identified particle events of >99 % and a fraction of falsely classified carrier events of $< 10^{-6}$ on the testing set. The fraction of events surviving the cut for the actual data is around 1 % but can reach up to 5-30 % during the rate spikes towards the end of the run (see Fig. 4.19). Since the true ratio between carrier and absorber events in the real data is not known, it is impossible to say how many of the accepted events are absorber events and how many of them are false positives, so the two numbers can not be strictly

compared.

Since one expects the rate of particle induced events to remain approximately constant over time, it seems very likely that the increased rate of expected events during the high rate periods is caused by some kind of mechanical or electronic disturbances. If this is indeed the case, the high rate periods should be discarded for the low threshold analysis, since they would introduce a large amount of background events at low energies. On the other hand, if one wants to use these periods despite the higher background, one needs to apply additional harsh cuts which substantially reduce the overall cut acceptance at low energies. The parameters used for these cuts are the ratio of the RMS values in the particle and carrier template fits, the ratio of the amplitudes of both fits and the difference of the shift parameters obtained in both fits. The cut values are determined by comparing the respective energy-dependent parameter distributions of these parameters from the artificially generated data and from real data. The results are discussed in Sec. 5.4.

4.4 Trigger Threshold

4.4.1 Determination of the Trigger Threshold

Knowledge of the trigger threshold is crucial if one wants to analyze low energy data. The method developed within the collaboration uses low energy pulses injected in the TES heater to determine the trigger threshold. The trigger efficiency at a given injected energy is then simply the fraction of the injected heater pulses with that energy which cause a trigger. The energy of the injected pulses is cycled periodically, so for a sufficiently long period the number of injected pulses at each energy is the same. Since only pulses causing a trigger are recorded, one can simply divide the number of recorded pulses at each injected energy by the number of recorded pulses at a large injected energy, where it can safely be assumed that it will always cause a trigger.

One expects the measured fractions to follow an efficiency function based on the Gaussian error function erf:

$$f(E_{inj}) = \frac{1}{2}\left[1 + erf\left(\frac{E_{inj} - E_{thr}}{\sqrt{2}\sigma}\right)\right] \tag{4.11}$$

where E_{inj} is the injected energy, E_{thr} is the threshold energy, defined as the energy where 50 % of the injected pulses cause a trigger, and σ is the energy resolution of the trigger. This, however, neglects the fact that a particle pulse might occur at the same time a heater pulse is injected which, especially for small injected energies, causes an overestimation of the trigger efficiency. One

can model this contribution due to pile-up as a constant contribution to the trigger efficiency with a fixed pile-up probability $p_{pile-up}$:

$$f(E_{inj}) = \frac{1 - p_{pile-up}}{2} \left[1 + erf\left(\frac{E_{inj} - E_{thr}}{\sqrt{2}\sigma} \right) \right] + p_{pile-up} \tag{4.12}$$

This model can then be fitted to the measured data to extract the energy threshold. A simple estimate for the pile-up probability can be obtained from the rate of particle pulses observed in the detector and the record length of the pulses. The simple approximation for the probability $p_{\mathrm{pile-up}}$ to find a pulse in a coincidence time window ΔT, when the rate of pulses is R is simply

$$p_{\mathrm{pile-up}} = R \cdot \Delta T \tag{4.13}$$

If one takes the average rate of particle pulses which is $\sim 0.04\, s^{-1}$ and the record length of $\sim$ 330 ms as coincidence time window one ends up with a pile-up probability on the order of a few percent, which is consistent with the fit results. The actual pile-up probability varies of course with the trigger rate of the individual detector (see Tab. 4.2).

4.4.2 Longterm Stability

To obtain sufficient precision, the injected energies need to be closely spaced around the threshold energy. This is not possible during regular data taking since there, higher energy heater pulses are needed for the energy calibration. Thus dedicated files are recorded to determine the trigger thresholds. To check the longterm stability of the trigger threshold the trigger efficiency of the lowest energy heater pulse which is injected during regular data taking can be monitored. This is shown in Fig. 4.20 where, for detector Lise, the fraction of test pulses injected with an energy of ~ 0.4 keV causing a trigger is shown over a timespan of $\sim$ 200 hours. During the entire time the trigger efficiency remains high around $\sim 96\,\%$ and is always larger than $\sim 93\,\%$. This demonstrates the excellent longterm stability of the trigger threshold.

4.4.3 Systematic Effects

A possible source for systematic effects are the different pulse shapes of test and particle pulses shown in Fig. 4.5. However, since the trigger electronics shapes the pulses with a low-pass filter, one expects the trigger to be more efficient for the longer particle pulses than the shorter test pulses. This should consequently lead to conservative values for the trigger efficiency.

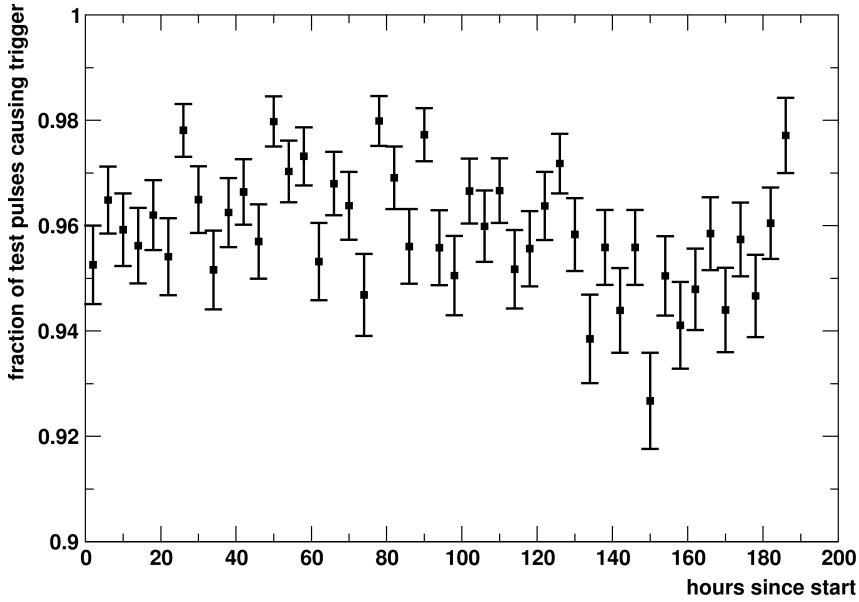

Figure 4.20: Fraction of test pulses injected with an energy of $\sim 0.4\,\mathrm{keV}$ causing a trigger over time for detector Lise. As can be seen the fraction always remains high (between 93 and 98 %), demonstrating the stability of the trigger threshold.

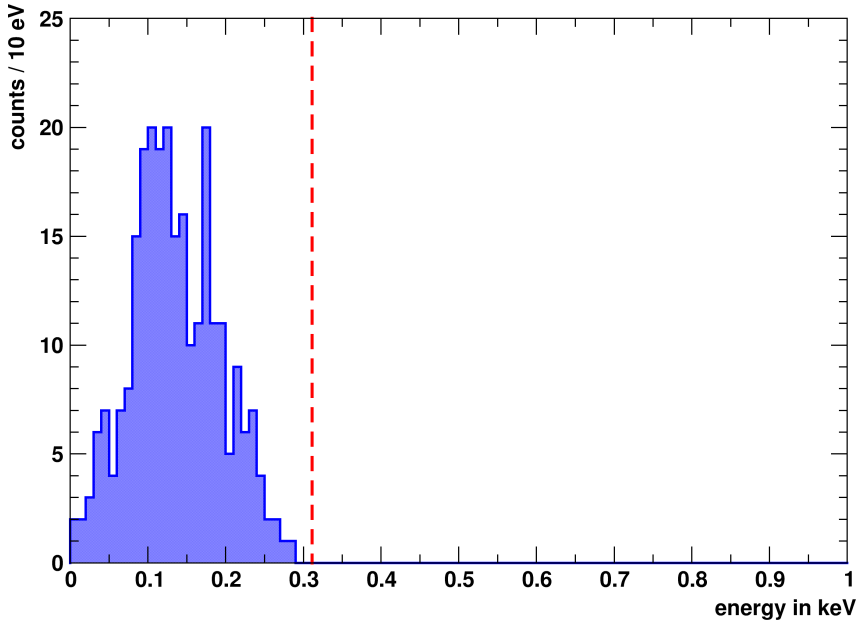

Figure 4.21: Energy spectrum of events in the phonon detector of module Lise/Enrico where only the light detector caused a trigger. As expected, no events are present above the trigger threshold of the phonon detector of 311 keV (dashed red line) validating the method of determining the trigger threshold.

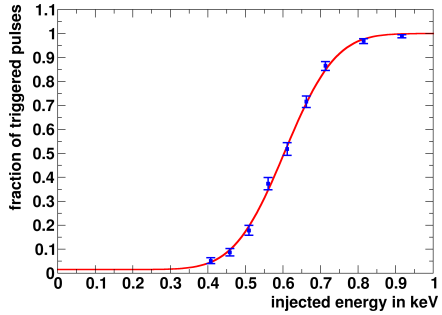

(a) TUM40 before lowering threshold.

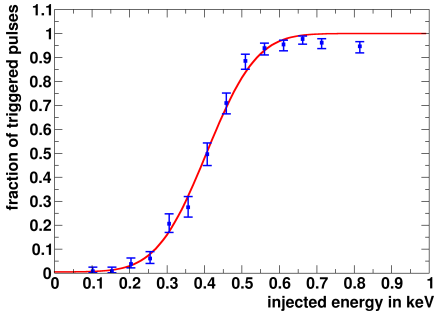

(b) TUM40 after lowering threshold.

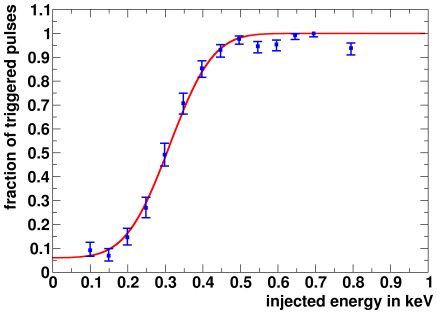

(c) Lise after lowering threshold.

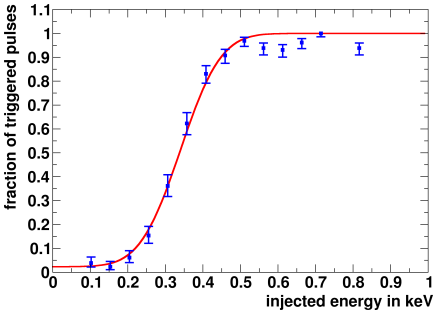

(d) Daisy after lowering threshold.

Figure 4.22: Measured trigger threshold of selected detectors. The blue dots show the fraction of test pulses causing a trigger at various injected energies. The result of the fit with the efficiency function is drawn in red.

The measured trigger efficiency can be cross-checked by looking at the phonon energy distribution of light-only events, i.e. events where only the light detector has triggered and not the phonon detector (e.g. direct hits of the light detector).[5] If the trigger efficiency measured with heater pulses corresponds to the trigger efficiency for particle pulses, one expects to see no light-only events with phonon energies above the fitted threshold energy, since for these events the phonon detector should have triggered which no longer makes them light-only events (see Fig. 4.21).

4.4.4 Results

In the past, the analysis threshold was always defined by the overlap between the nuclear recoil bands and the e^-/γ -band. In run 32 e.g. the energy above which one event from the e^-/γ -band was expected to leak into the nuclear recoil bands was chosen. These analysis thresholds have always been $\mathcal{O}(10)$ keV

[5] A sample of light-only events can be obtained by selecting only events where the trigger delay parameters of the phonon detector is at its overflow value.

and higher, far above the hardware trigger threshold of the phonon detectors, so no special care has been taken to optimize them. The only check at the beginning of this run was to see if the lowest energy test pulse ($\sim 5\,\mathrm{keV}$) was triggering efficiently. Nonetheless three detectors exhibited a trigger threshold below 1 keV. Only after the potential of a low threshold analysis has been realized and the importance of the trigger threshold became apparent, an effort was made to optimize the thresholds of all detectors. Based on the baseline energy resolution of the phonon channel, five detectors were selected and their thresholds optimized by adjusting the shaping times of the trigger electronics and lowering the threshold values. The results are compiled in Tab. 4.2. The lowest thresholds are achieved with detectors Lise ($311 \pm 7\,\mathrm{eV}$, Fig. 4.22c) and Daisy ($340 \pm 6\,\mathrm{keV}$, Fig. 4.22d), the threshold of the detector which initially had the lowest threshold TUM40 could be lowered from $605 \pm 5\,\mathrm{eV}$ (see Fig. 4.22a) to $406 \pm 6\,\mathrm{eV}$ (see Fig. 4.22b).

Table 4.2: Measured energy thresholds for phonon detectors with thresholds $\leq 1\,\mathrm{keV}$.

	at beginning			after optimization		
	E_{thr} in eV	σ in eV	$p_{pile-up}$	E_{thr} in eV	σ in eV	$p_{pile-up}$
VK32	607 ± 3	83 ± 4	0.019 ± 0.003	506 ± 5	72 ± 7	0.069 ± 0.012
TUM-40	605 ± 5	106 ± 6	0.015 ± 0.017	406 ± 6	105 ± 7	0.005 ± 0.006
VK34	> 1 keV	—	—	460 ± 7	114 ± 7	0.028 ± 0.011
Frederika	753 ± 6	135 ± 7	0.008 ± 0.002	758 ± 13	152 ± 15	0.006 ± 0.007
Lise	> 1 keV	—	—	311 ± 7	91 ± 8	0.060 ± 0.025
Daisy	> 1 keV	—	—	340 ± 6	85 ± 7	0.023 ± 0.014

4.5 Energy Resolution and Bands

The light yield of an event is used to discriminate between signal and background events. This is usually done by selecting a region in the energy-light yield plane where the expected signal is large compared to the expected background. To do so, a description for the distribution of signal and background events in the energy-light yield plane is needed. In the past such a description has been developed [73] which relies on the amount of light produced for a given interaction type as a function of energy and the energy-dependent energy resolutions of the light and phonon detector. The events fall into bands which are centered around the mean light yield (which can be energy-dependent) and have a width characterized by the energy resolutions of the detectors.

4.5.1 Energy Resolutions

For most applications the baseline energy resolution, i.e. the resolution at zero energy, is relevant, e.g. as input for the determination of the band parameters or the expected energy spectrum for the limit calculation. To extract the baseline energy resolution, a Gaussian is fitted to the distribution of the amplitudes of events from a low energy test pulse, which should only be affected by the baseline noise. For most detectors the 5 keV test pulse is used, for detectors with a particularly large resolution higher energy test pulses have to be used. This is the case for phonon detector TUM45 and light detector Enrico, where the 40 keV test pulse is used, as well as phonon detector VK27, where the 10 keV test pulse is used. From the width σ and the position μ resulting from the fit, the resolution can be obtained by multiplying the relative resolution σ/μ with the energy of the injected test pulse E_{TP}:

$$\sigma_{TP} = \frac{\sigma}{\mu} E_{TP} \tag{4.14}$$

The results for all detectors are compiled in Tab. 4.3. For the light detectors equipped with an ^{55}Fe source, the baseline resolution can also be determined in absolute energies.

4.5.2 Band Description

Since it is difficult to acquire enough statistics to measure the nuclear recoil bands directly one resorts to extracting the resolution parameters from the e^-/γ -band and then using them to calculate the nuclear recoil bands. For this purpose a maximum-likelihood fit of the full two-dimensional likelihood of the e^-/γ -band is performed. The fit is performed in the phonon energy-light energy (E-L) plane and not in the energy-light yield plane as this avoids complications due to the interplay of phonon energy resolution and light energy resolution. The results can, however, be used to calculate the bands in the energy-light yield plane. In the following the different components needed to describe the data in the E-L plane are described. This is based on previous work which can be found e.g. in [80, 73].

Center of the Bands

For an idealized scintillator the amount of light produced - or the light energy L - is simply proportional to the energy E deposited in the scintillator. For e^-/γ -events this proportionality factor turns out to be 1 due to the way the detectors are calibrated. In real scintillators there might be non-linear behavior which has to be taken into account. The main source for non-linearities

Table 4.3: Baseline energy resolution as inferred from a Gaussian fitted to test pulse events. Light detector resolutions are given in electron equivalent energy eV_{ee}. For the light detectors equipped with an ^{55}Fe source, the resolution is also given in absolute energy eV_{abs}.

	σ_{TP} in eV_{ee}		σ_{TP} in eV_{abs}
	phonon	light	
VK31/Kurt	336 ± 1	366 ± 1	—
VK32/Anders	69.7 ± 0.1	310 ± 1	—
VK33/Franz	175 ± 1	1223 ± 11	—
TUM40/Michael	97.2 ± 0.1	306 ± 1	—
TUM29Thomas	165 ± 1	319 ± 1	5.91 ± 0.01
Verena/Q	131 ± 1	618 ± 4	—
Rita/Steven	372 ± 4	—	—
VK34/Leon	124 ± 3	240 ± 1	3.83 ± 0.01
Zora/Yoichiro	229 ± 1	525 ± 3	—
TUM45/Oliver	—	330 ± 1	6.67 ± 0.01
TUM38/Petrus	126 ± 1	394 ± 1	3.35 ± 0.01
Frederika/Gabriel	121 ± 1	311 ± 1	—
Wibke/X	158 ± 1	462 ± 2	—
Lise/Enrico	77.4 ± 0.1	4213 ± 12	96.6 ± 0.2
Daisy/Donald	84.6 ± 0.1	431 ± 1	—
Anja/Claudius	145 ± 1	385 ± 3	—
VK27/Diogenes	988 ± 4	191 ± 2	7.07 ± 0.06
VK28/Zam	144 ± 1	140 ± 1	5.81 ± 0.02

for e^-/γ -events is the reduced light output of electrons for low deposited energies sometimes referred to as the non-proportionality effect. The reason for this is that for decreasing electron energies the ionization density increases, which leads to a higher probability for non-radiative recombination of the initially generated electron-hole pairs [70]. This non-proportionality effect can be described by an exponential decrease of the light output towards low energies.

In addition there can also be non-linearities at higher deposited energies. These are modeled by an additional quadratic term. The full model for e^-/γ -events thus looks like this:

$$L^{\gamma}(E) = (L_0 E + L_1 E^2)(1 - L_2 e^{-\frac{E}{L_3}}) \tag{4.15}$$

where L_0 is the proportionality constant which in our case is close to 1, L_1 describes the energy dependence at higher energies, which usually turns out

to be small, and L_2 and L_3 model the non-proportionality at low energies.

Nuclear recoils have a reduced light output compared to e^-/γ -events which is quantified by the so-called quenching factors QF. For nuclear recoils the reduced light output due to the non-proportionality is not observed. On the contrary, precision measurements of the quenching factors show that the light output increases towards lower energies [95]. Therefore the non-proportionality term is dropped for the nuclear recoil bands and the energy dependence of the light output is introduced by making the quenching factors themselves energy dependent. This leads to the following model for nuclear recoils:

$$L^A(E) = QF^A(E)(L_0E + L_1E^2) \tag{4.16}$$

where the index A indicates the type of nucleus, $QF^A(E)$ is the energy-dependent quenching factor and L_0 and L_1 are the same parameters as for the e^-/γ -band. For the parametrization of the energy-dependent quenching factors the empirical model from [95] is used:

$$QF^A(E) = QF^{A,\infty}\left(1 + ae^{-\frac{E}{b}}\right) \tag{4.17}$$

The values for the model parameters $QF^{A,\infty}$, a and b are compiled in Tab. 4.4. For the quenching factor of tungsten the energy dependence was found to be negligible, so a constant value is assumed.

Table 4.4: Values for the model parameters $QF^{A,\infty}$, a and b for the empirical model of the energy-dependent quenching factors for oxygen, calcium and tungsten taken from [95].

	$QF^{A,\infty}$	a	b
O	0.07582	0.7088	567.1
Ca	0.05704	0.1887	801.3
W	0.0196	—	—

As shown in [70], the quenching factors are influenced by the optical properties of the individual crystals, e.g. the density of defects in the crystal lattice. Thus some variation of the quenching factors can be expected between crystals. This has already been observed in [95] and a method was proposed to correct for this effect. This method assumes, that the energy-dependence remains unchanged and the entire band is shifted up or down, i.e. the asymptotic quenching factor $QF^{A,\infty}$ is modified by a constant factor ϵ. To determine this correction factor one can use data obtained with a neutron source. In the energy range between 150 and 200 keV neutrons are expected to scatter

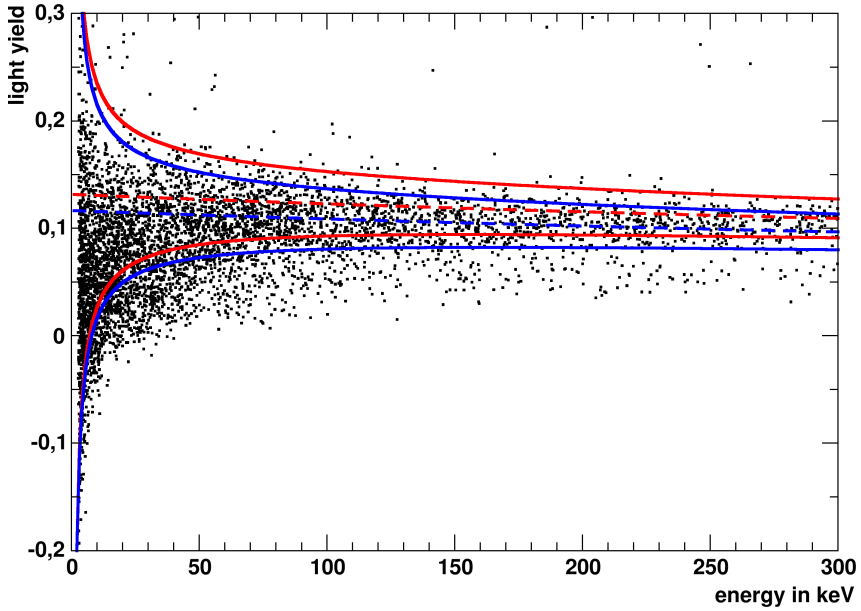

Figure 4.23: Data from module TUM38/Petrus under irradiation with neutrons from an Am-Be source displayed in the energy-light yield plane. The dashed lines show the center, the solid lines show the lower and upper 90 % contours of the oxygen band before (red) and after (blue) adjusting the quenching factor. At high energies, the population is dominated by oxygen scatters, whereas at energies below $\sim$ 50 keV a significant contribution of tungsten recoils can be observed which have a lower light yield compared to oxygen recoils. The faint population below the oxygen band extending to higher energies can be attributed to calcium recoils which have a light yield in between oxygen and tungsten recoils. Before the adjustment the calculated band is at higher light yields compared to the data, after the adjustment the calculated band and the data show good agreement.

predominantly off oxygen and the contributions from calcium and tungsten can be neglected. By looking at the average light yield observed in this energy range $\overline{QF_{obs}}$ and comparing it to the average expected light yield in this energy range $\overline{QF_{exp}}$ (as computed by the formula above) one can determine the correction factor as $\epsilon = \frac{\overline{QF_{obs}}}{\overline{QF_{exp}}}$. The values for ϵ obtained for the relevant detectors are compiled in Tab. 4.5. Fig. 4.23 shows the effect of this correction of the quenching factors by comparing the center and 90 % lower and upper contours of the oxygen band as calculated by the formula above before and after the correction in comparison to the data obtained with an Am-Be neutron source. Applying the correction improves the agreement between calculated band and data.

Table 4.5: Values for the correction factor ϵ determined for the different detectors.

	ϵ
TUM40/Michael	0.8734
TUM38/Petrus	0.8851
Lise/Enrico	0.9144
Daisy/Donald	0.9696
VK27/Diogenes	0.8545
VK28/Zam	0.8537

Width of the Bands

The width of the bands is given by the energy resolutions of the phonon and the light detectors σ_L and σ_P respectively. Since they are approximately statistically independent one can add them quadratically to obtain the combined resolution

$$\sigma(E) = \sqrt{\sigma_L(L(E))^2 + \sigma_P(E)^2} \tag{4.18}$$

where the light detector resolution σ_L depends on the light energy and the phonon detector resolution σ_P depends on the deposited energy.

The phonon detector resolution is usually small compared to the light detector resolution and only causes a small correction. Therefore it is sufficient to assume a constant energy resolution for the phonon channel. If one adds a linear term this usually turns out to be small. Since the resolution of the light channel is generally much larger it dominates the width of the bands. The light detector resolution is parametrized by three parameters:

$$\sigma_L(L) = \sqrt{S_0 + S_1 L + S_2 L^2} \tag{4.19}$$

where S_0 corresponds to the constant baseline noise, S_1 accounts for photon statistics and S_2 models position dependence of the scintillator.

Excess-Light Events

At low energies there is an additional population of events with light yields higher than expected for e^-/γ -events. They become visible as high light yield tails if one looks at the light yield distribution in a small energy slice. The origin of these events is not entirely clear. It is suspected that they are caused by electrons passing through the scintillating foil thereby creating additional light which shifts them out of the e^-/γ -band. This theory is supported by the

fact that these events are not visible in detector modules which have a beaker as light detector.

One can model the light yield distribution of the excess-light events $X(L)$ with an exponentially modified Gaussian distribution which is the result of the convolution of an exponential distribution, which represents the true distribution of the excess-light events, with the Gaussian width of the e^-/γ -band. The distribution is thus centered at the mean light yield of the e^-/γ -band $L^\gamma(E)$.

$$X(L) = \frac{1}{2\tau_{el}} \exp\left(\frac{L^\gamma - L}{\tau_{el}} + \left(\frac{\sigma^\gamma}{\tau_{el}}\right)^2\right)\left(1 - \text{erf}\left(\frac{L^\gamma - L + (\sigma^\gamma)^2}{\sqrt{2}\sigma^\gamma}\right)\right) \quad (4.20)$$

4.5.3 Full Likelihood

In addition to the light yield distribution the full likelihood requires a model for the energy spectra of the different event classes. The spectrum of the e^-/γ -events at low energies can be approximated by a linear component with slope p accounting for the continuous background due to β-decay and Compton scattering and a number of Gaussian peaks corresponding to γ-lines. The resolution of these peaks is described by the linear phonon energy resolution σ_P. One observes in the data that the mean light yield of the γ-peaks is not centered in the continuous e^-/γ -band but lies below. This reduced light yield can be attributed to the non-proportionality effect of electrons, since a γ-ray produces (at least) one electron-hole pair, so its energy is shared among multiple particles each having a reduced light output [70]. One therefore has to model each γ-line individually with a separate quenching factor as the product of the Gaussian energy distribution and the quenched light yield distribution:

$$\mathcal{L}_{peak}(E, L) = \text{Gauss}(E; \mu, \sigma) L^{QF}(L|E) \quad (4.21)$$

where $L^{QF}(L|E)$ is a conditional probability density.

The energy distribution of the excess-light events is modeled with an exponential decay, so that the full likelihood can be written as:

$$\begin{aligned} \mathcal{L}(E, L) &= (1 - \sum_i f_i - f_{el})(1 + p \cdot E) L^\gamma(L|E) \\ &+ f_{el} \frac{1}{E^{el}_{dec}} \exp\left(-\frac{E}{E^{el}_{dec}}\right) X(L|E) + \sum_i f_i \mathcal{L}^i_{peak}(E, L) \end{aligned} \quad (4.22)$$

where f_{el} is the fraction of excess-light events and f_i is the fraction of events in the i-th γ-peak.

4.6 Setting a Limit

The signal-like excess observed in the previous run 32 data (cf. Sec. 3.4) could not be confirmed with the data of run 33 analyzed in this work (cf. Sec. 5.1). The absence of a signal means that only upper limits on the dark matter-nucleon cross section can be set. The lack of a robust background model from Monte Carlo simulations requires the use of methods which make no assumptions about the observed backgrounds. One such method which has been developed in the context of direct dark matter searches is the so-called optimum interval method [96]. This method improves upon the simple method of applying Poisson statistics to the number of observed events in an arbitrarily defined signal region by taking the expected energy spectrum of the signal into account.

The basic idea behind this method is to select the region in the data which maximizes the signal expectation with respect to the observed background. But doing so after looking at the observed data introduces an unwanted bias since one could have just selected a statistical fluke. One can correct for this bias by determining how often one finds an equally good interval in a simplified Monte Carlo simulation assuming no background. These Monte Carlo simulations, however, can be computationally expensive and the main reason why this method is widely applied is that one can transform any spectrum into a uniform spectrum by taking the cumulative distribution function. This allows to re-use the results of the lengthy Monte Carlo simulations, which now only has to be performed once for a uniform spectrum, for arbitrary spectra. One only has to transform the measured quantity - in this case the energy - to a uniform spectrum.

The limit setting code developed in this work uses the original FORTRAN code which has been published alongside the paper describing the method. The original method described in [96] is only valid for small numbers of observed events (< 54.5). In [97] the method has been extended to work also with larger numbers of events. This is included in the up-to-date version of the code which is used for this work. This extension becomes important when data is analyzed close to the trigger threshold, where rather large numbers of events can be observed in the acceptance region for dark matter.

Chapter 5

Results

This chapter covers the results of the analysis of run 33 data. If not explicitly stated otherwise, all results presented here have been obtained in this work. Similar results based on the same data can be found in [83, 84].

The main goal in preparation of this run was to clarify the nature of the excess events observed in run 32. For this, limits on the dark matter-nucleon cross section are set using data recorded with the detectors, which have one of the novel designs. In contrast to the conventional detectors, these novel detectors show no signs of the backgrounds related to surface α-decays, which were present in run 32. The resulting limits exclude the dark matter interpretation of the run 32 excess, supporting the conjecture that the excess events are related to these surface α-backgrounds.

In addition, the sub-keV energy threshold and the unprecedented low e^-/γ -background of detector TUM40 motivated the development of a low threshold analysis, targeting dark matter masses below $10\,\mathrm{GeV}/c^2$. First, studies of the low energy background of this detector, which is dominated by electron capture decays of cosmogenically activated isotopes of tungsten, are shown. Then the influence of different parameters (e.g. threshold, background level, choice of acceptance region) on the sensitivity of a low threshold analysis are examined. Finally, the resulting limits for different data sets obtained with TUM40 and two other detectors (Lise and Daisy) are presented. These results led to two publications: the first one based on data from TUM40 with a threshold of 605 eV [66] and the second one based on Lise with a threshold of 307 eV [65]. Using the same data, also limits on momentum dependent scattering of dark matter could be set and published [98]. To conclude, the impact of various improvements of the detector design on the sensitivity for light dark matter is investigated.

5.1 Combined Dark Matter Limit

As outlined in Sec 3.4, there has been an excess of events observed in the previous run 32 above the modeled backgrounds, which could be interpreted as a dark matter signal. There remain, however, some uncertainties concerning the modeling of these backgrounds, especially the recoil background related to α-decays occurring on non-active surfaces facing the absorber crystals. To avoid this background, two different approaches have been pursued: firstly, reducing the contamination of the detector modules with α-emitters, mainly by preventing exposure of all parts of the detector modules to radon, and secondly making all surfaces facing the absorber crystal active, thus allowing the identification and rejection of these backgrounds (cf. Sec. 3.5).

The first approach, the background reduction, unfortunately has not been successful. All conventional detector modules show some level of recoil events around 100 keV in the nuclear recoil band. The latter approach, actively vetoing these events, however, has proven to be a success. All three novel detector designs (*beaker*, *carrier* and *stick*), show no signs of recoil events around 100 keV (see e.g. Fig. 5.2). To test the hypothesis that the excess was indeed caused by recoil events leaking into the acceptance region, only the six modules with improved design (TUM29, TUM38, TUM40, TUM45, VK27 and VK28) will be considered.

After looking at the training data, TUM45, TUM29 and VK27 have to be excluded. TUM45 could not be operated properly in the beginning of the run. In April 2014 the operating point of the detector was changed, which enabled the correct operation of the detector. However, the amplitudes of the signals turn out to be very small, resulting in a unusually high energy threshold of the phonon detector ($\sim$ 15 keV). This, together with the significantly reduced

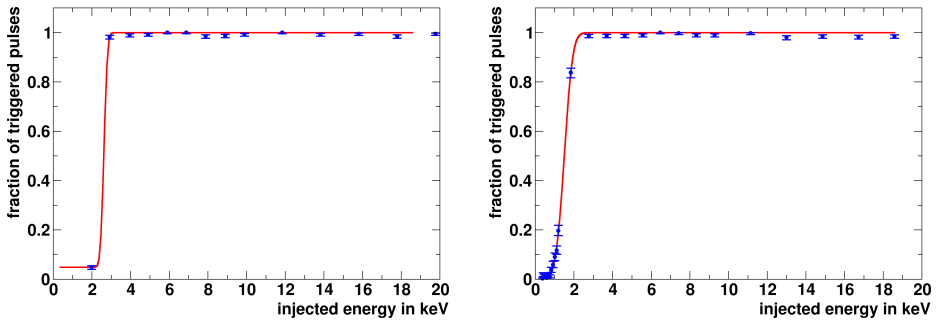

(a) TUM38/Petrus. (b) VK28/Zam.

Figure 5.1: Trigger threshold inferred by the fraction of test pulses with different injected energies causing a trigger (blue data points). The red curve shows the result of a fit with the efficiency function introduced in Sec. 4.4.

exposure compared to the other modules, led to the decision to exclude this module from the final analysis, since the contribution to the combined exposure is marginal. In TUM29 and VK27, which both have a large carrier crystal, the separation of events induced in the carrier and the main absorber could not be performed sufficiently. Since these carrier-induced events are usually reconstructed with small energies and are accompanied with less light, they are likely to fall into the acceptance region for dark matter candidates.

For the remaining three detectors (TUM40, TUM38, and VK28), data sets are defined by excluding very short files ($\lesssim 1\,\mathrm{h}$) and files with exceptionally high trigger rates or large fractions of unstable detector operation. The resulting exposures (after considering dead time from the DAQ system and the stability cut) of the three modules are compiled in Tab. 5.1, together with their mass and hardware energy threshold (see Fig. 5.1).

Table 5.1: Mass, exposure and energy threshold for the three modules selected for the combined analysis.

	mass in g	exposure in kg days	threshold in keV
TUM40/Michael	248	110.6	0.605 ± 0.005
TUM38/Petrus	299	146.8	2.62 ± 0.04
VK28/Zam	194	103.7	1.50 ± 0.02

Different possibilities to combine multiple detectors using the optimum interval method are discussed in [99]. In this work, the simple merging method is applied, which has already been used in past publications [100, 101]. It works by computing the cumulative probabilities of the accepted events for each detector individually and combining them in a single spectrum before computing the optimum interval. This method is best suited if the different detectors have similar background levels, since the number of observed counts is averaged over the combined exposure of all detectors. This means, that a single detector with exceptionally high background may spoil the limit although one would expect in the case of dark matter scattering that the events are distributed equally among the detectors. On the other hand, if the backgrounds of the different detectors are the same, the resulting limit will be the best one possible. This can be shown e.g. by splitting the data of a single detector and combining it with the method described above. The resulting limit will be identical to the one obtained with the single large dataset.

In order to obtain a result which is comparable to the one from run 32, the same definition of the acceptance region is chosen: it contains all three nuclear recoil bands from the lower 90 % contour of the tungsten band to the upper

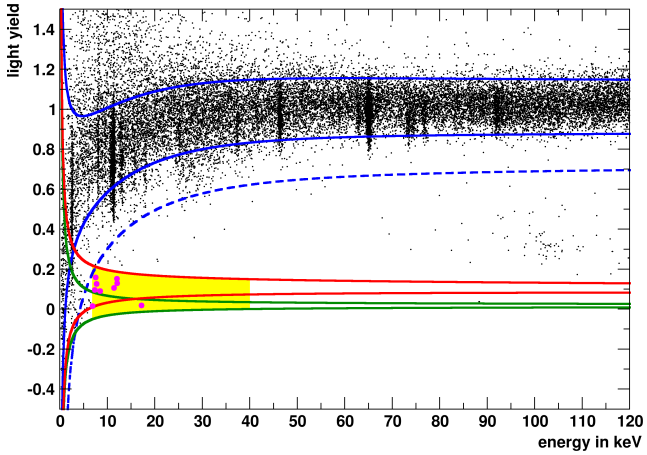

(a) TUM40/Michael.

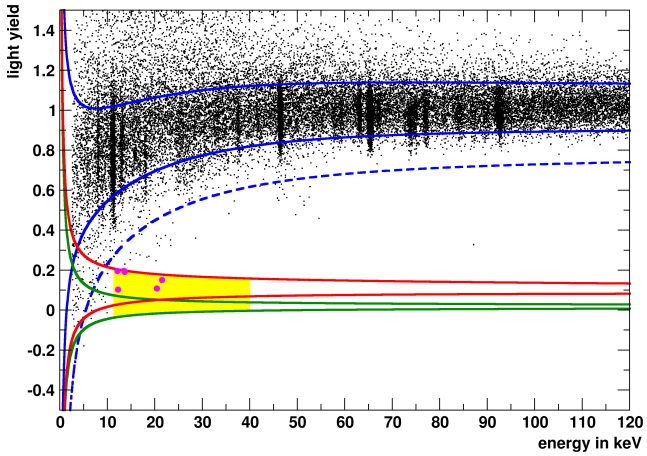

(b) TUM38/Petrus.

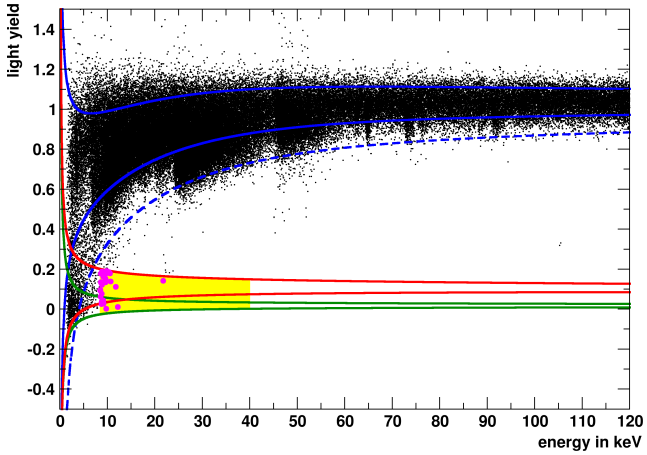

(c) VK28/Zam.

Figure 5.2: Data of the three selected detectors in the energy-light yield plane. Drawn in solid blue, red and green are the lower and upper 90 % contours of the e^-/γ -, oxygen and tungsten bands. The dashed blue line indicates the lower $3\,\sigma$ contour of the e^-/γ -band. The acceptance regions for a lower threshold where 0.1 leakage events are accepted are shaded in yellow, the events therein are highlighted in magenta.

90 % contour of the oxygen band. The upper boundary of the energy range is set at 40 keV. The lower boundary is defined for each detector individually as the energy E_1 where one e^-/γ -event is expected to leak into the acceptance region (see Tab. 5.2). The resulting limit from a combined exposure of 361.1 kg days is shown in solid blue in Fig. 5.3 and does not completely rule out the dark matter interpretation of run 32 indicated by the regions shaded in red [53] .

If one looks at the number of observed events in Tab. 5.2, which is 46 for all three detectors, it is clear that it is not compatible with the expectation of 3 events from the e^-/γ -band, especially for detector VK28/Zam, which alone is responsible for 31 events. However, most of these events are close to the analysis threshold so it might be that the leakage is underestimated. To test this hypothesis the analysis is repeated with the analysis thresholds set at the energies $E_{0.1}$ where 0.1 events are expected to leak from the e^-/γ -band (also compiled in Tab. 5.2). This reduces the number of events in the acceptance region to 13, which is of course still much higher than the 0.3 events expected from leakage. The distribution of these events among the detectors changes completely: VK28/Zam which initially had the largest amount of events with 31, now has the least events with 3, whereas TUM38/Petrus continues to observe 6 events which is now the largest amount. Although the number of observed events is still inconsistent with the expectation from e^-/γ -background, the resulting limit (dashed blue in Fig. 5.3) is much improved and now clearly rules out the M2 region and almost all of the M1 region.

Table 5.2: Analysis thresholds for the three modules. The thresholds are set such that 1 or 0.1 events are expected to leak into the acceptance region from the e^-/γ -band. Next to the threshold, the actual number of observed events is shown.

	E_1 in keV	observed	$E_{0.1}$ in keV	observed
TUM40/Michael	6.82	9	11.38	4
TUM38/Petrus	11.27	6	12.10	6
VK28/Zam	8.39	31	11.26	3

To explain the discrepancy between the observed and expected number of events one could of course still argue that the leakage is underestimated. However, 4 of the 13 events are far above the respective analysis thresholds: one at 17.2 keV in TUM40/Michael, two at 20.5 keV and 21.6 keV in TUM38/Petrus and one at 21.8 keV in VK28/Zam. The likelihood that these events can be attributed to leakage from the e^-/γ -band is very small. A possible explanation

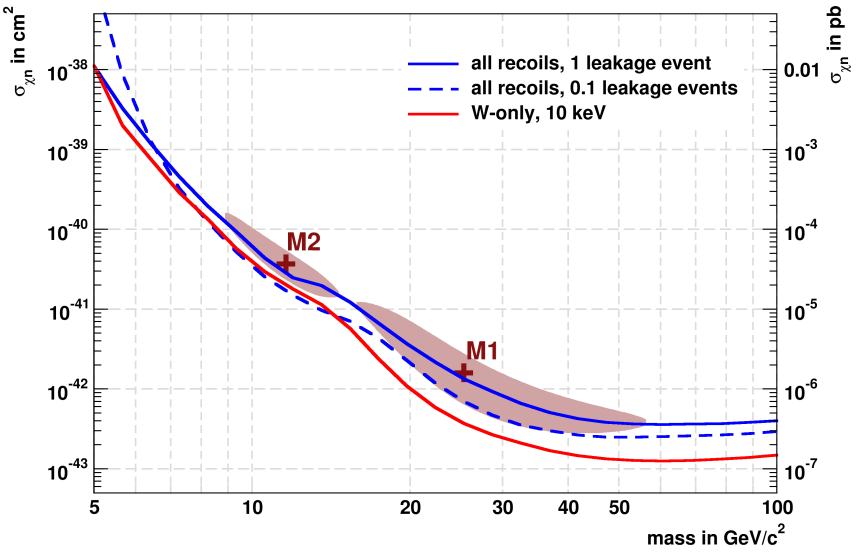

Figure 5.3: 90 % C.L. upper limits on the dark matter-nucleon cross section for different combinations of the data from modules TUM40/Michael, TUM38/Petrus and VK28/Zam. The solid (dashed) blue curve shows the limit for all three nuclear recoil bands and a threshold set where 1 (0.1) leakage event is expected from the e^-/γ -band for each detector. The red curve shows the limit from the tungsten band only and thresholds set at 10 keV for all three detectors. The red shaded regions indicate the regions in the parameter space compatible with the excess observed in run 32 at 90 % C.L., the crosses indicate the best fit points of the two likelihood maxima [53].

for these events, however, could be neutrons. If one takes the values for the neutron background from the likelihood fit in [53] at face value, one would expect between 7.5 and 9.7 neutrons for an exposure of 730 kg days. Scaling these numbers to the exposure of 361.1 kg days obtained with the three modules discussed here, one ends up with an expectation between 3.7 and 4.8 events due to neutrons, in perfect agreement with the 4 high energetic events observed. This, however, is only a very crude argument, since firstly, it assumes that the numbers for the neutron background inferred from the run 32 data are correct and secondly, it completely neglects any differences between the two runs (e.g. different number of running modules, the additional polyethylene shielding introduced in this run, etc.). To come up with a reliable estimate for the neutron background for the current run one would have to perform detailed Monte Carlo simulations of the entire setup, which is beyond the scope of this thesis.

It is, however, fruitful to explore the consequences, if one assumes that these events are indeed caused by neutrons. Since neutrons are expected to scatter predominantly off oxygen, the tungsten band should remain more or less

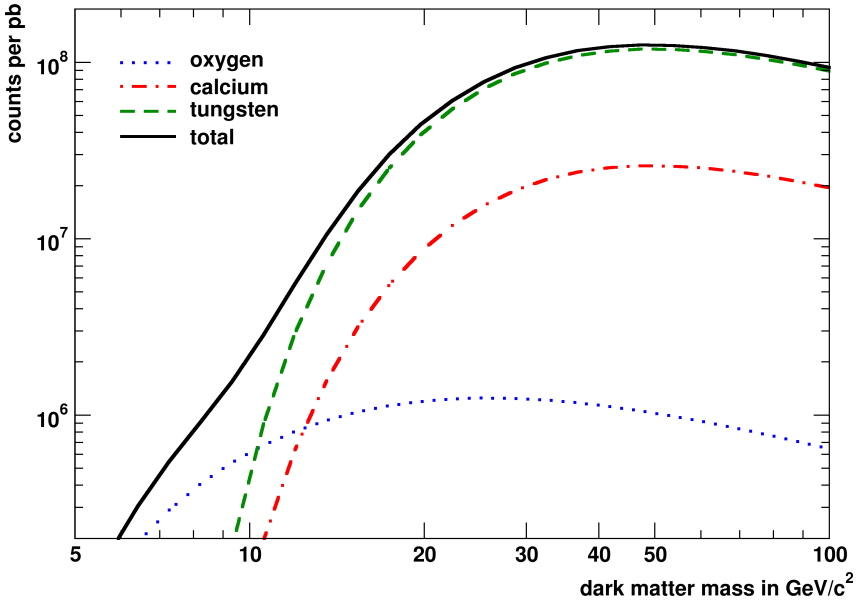

Figure 5.4: Number of counts expected from a dark matter particle with a cross section of 1 pb ($10^{-36}\,\mathrm{cm}^2$) for the different nuclei. For masses above $\sim 10\,\mathrm{GeV}/c^2$ the majority of events are expected to be tungsten recoils.

free of neutron background. In addition, if one looks at the number of events expected for different dark matter masses (see Fig.5.4), it becomes clear that above masses of $\sim 10\,\mathrm{GeV}/c^2$ the spectrum will be dominated by tungsten recoils. Since the optimum interval method is unable to take these different light yield distributions into account, the only option is to restrict the acceptance region to the tungsten band (i.e. everything between the lower and upper 90 % contours). In this case the analysis threshold is arbitrarily set at 10 keV for all three detectors, which results in a total of two events observed in the three detectors. The resulting limit (solid red in Fig. 5.3) is again improved and now completely rules out the dark matter interpretation of the excess in the run 32 data.

Although it is not possible to directly identify the source of the excess events in run 32, the absence of such an excess in the fully active modules in run 33 undermines the interpretation that the excess events are correlated with α-decays at the surfaces of the detector housing. For future iterations of the experiment, this means that only fully active modules should be used to avoid the dangerous backgrounds related to surface α-decays.

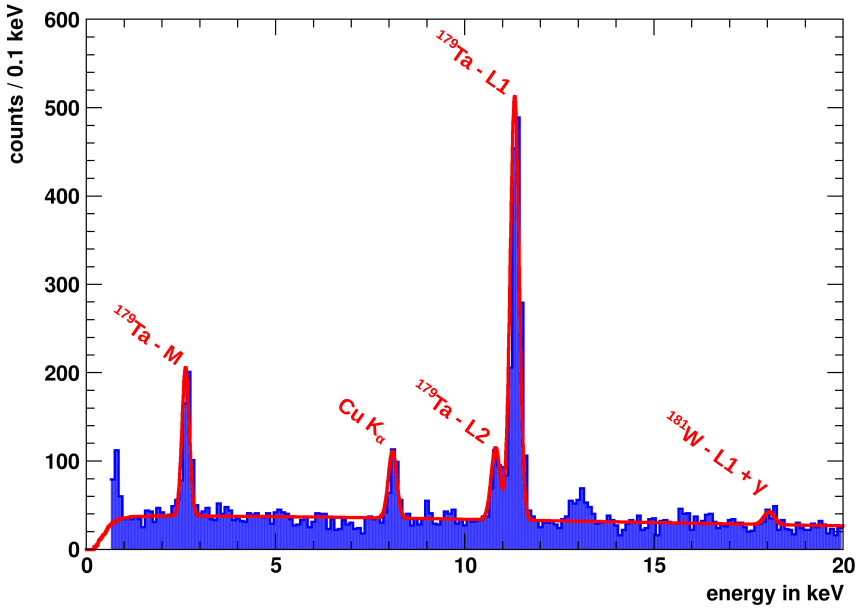

Figure 5.5: Low energy part of the energy spectrum of TUM40 (blue) shown together with a fitted background model (red). The background model includes the identified γ-lines, a linear component for the continuous background and the estimated cut acceptance.

5.2 Low Energy Background in TUM40

In the crystals grown at TUM, the continuous background at low energies due to β-decays (e.g. from ^{227}Ac) is significantly reduced compared to commercially available crystals [102]. In the low energy part of the spectra of these crystals, a series of γ-lines are visible (see Fig. 5.5). The line at 8 keV is the known fluorescence x-ray line of copper which is observed in all detectors since most of the materials surrounding the detectors is copper. The feature at 13 keV could not be identified.[1] All other lines are consistent with energies from electron capture decays of cosmogenically activated isotopes of tungsten. To confirm the origin of these lines from cosmogenically activated isotopes, the energies, relative intensities and the half-lifes of the different lines are compared to literature values.

5.2.1 Cosmogenic Activation of Tungsten Isotopes

There are 5 naturally occurring isotopes of tungsten (Tab. 5.3), only one of them (^{180}W) with an abundance of less than 1 %. These stable isotopes can be activated through nuclear reactions with protons or neutrons originating

[1] Some possible origins are discussed in [83].

from the hadronic component of cosmic rays. These activation processes occur as long as the raw materials or the grown crystals are transported or stored above ground. As soon as they are moved underground, they are effectively shielded from the hadronic component of cosmic rays and, since the activated isotopes are usually unstable, it is possible to observe their decay. As there is always a period of a few weeks between moving the detectors underground to the LNGS and the start of data taking, isotopes with half-lives shorter than ~ 1 month cannot be observed.

Most isotopes produced by cosmogenic activation decay via β-decay. Due to the rather low activity of these isotopes, the resulting continuous spectra are not discernible.[2] There are, however, two isotopes which are rather long-lived and decay via electron capture leading to low energy lines in the spectrum: ^{179}Ta, which can be produced for example via a (p,α) reaction on ^{182}W, and ^{181}W, which is produced mainly via a (p,t) reaction on ^{183}W.

Table 5.3: Naturally occurring tungsten isotopes.

Isotope	natural abundance in %
^{180}W	0.12 (1)
^{182}W	26.50 (16)
^{183}W	14.31 (4)
^{184}W	30.64 (2)
^{186}W	28.43 (19)

5.2.2 Electron Capture

Electron capture (EC) is a variant of the β^+-decay where, instead of emitting a positron, an electron from one of the inner shells of the atom is captured. Most of the decay energy is carried away by the electron neutrino and can thus not be measured. The daughter atom which is left in an excited state, de-excites via the emission of a cascade of characteristic x-rays or Auger electrons. The total energy of this cascade equals the binding energy of the captured electron. Since the timescale of this cascade is fast compared to the typical rise times of CRESST detectors and the probability for one of the x-rays to escape is negligible, usually the entire energy of the cascade is measured.

This is shown in the following equation, where X denotes the parent nucleus with mass number A and charge Z and Y is the daughter nucleus with reduced charge $Z-1$. The star indicates that the daughter atom is in an excited state.

[2] It might be possible to observe these isotopes by looking for coincident γ-rays from the β-decays in other detector modules.

Table 5.4: X-ray binding energies, observed energies and activities for ^{179}Ta.

shell	E_{lit} in keV [104]	E_{obs} in keV	activity in μBq kg^{-1}
K	65.351	65.060 ± 0.004	175.3 ± 2.8
L1	11.271	11.313 ± 0.002	147.9 ± 2.5
L2	10.739	10.82 ± 0.01	26.5 ± 2.6
M1	2.601	2.615 ± 0.004	44.8 ± 1.8
N1	0.538	—	—

$$ {}^{A}_{Z}X + e^{-} \rightarrow {}^{A}_{Z-1}\,Y^{*} + \nu_e \tag{5.1} $$

Due to the higher overlap between electron and nucleus, the innermost electron from the K-shell is captured most likely and capture from higher shells is rare. However, if the Q-value of the decay is comparable to the binding energies of the electrons, the capture from higher shells is not negligible because more energy is released when a less tightly bound electron from a higher shell is captured. A formula to calculate the ratios for capture from different shells is presented in [103]:

$$ \frac{\lambda_X}{\lambda_Y} = \frac{n_X (Q_{EC} - E_{level} - E_{b,X})^2 \beta_X^2 B_X}{n_Y (Q_{EC} - E_{level} - E_{b,Y})^2 \beta_Y^2 B_Y} \tag{5.2} $$

where X and Y are the corresponding shell indices, n_X is the filling factor of the X-shell, Q_{EC} is the Q-value of the EC process, E_{level} is the energy of the level in the daughter nucleus, $E_{b,X}$ is the binding energy of the electron in the X-shell, β_X and B_X are values for the overlap of the X-shell electron with the nucleus and are tabulated in [103].

5.2.3 Electron capture of ^{179}Ta

^{179}Ta decays exclusively via electron capture to the ground state of ^{179}Hf with a half-life of 662 days and a Q-value of 105.6 keV [104]. Data from an exposure of 117.04 kg days of detector TUM40 taken between August 2013 and May 2015 are used to extract the energies and activities of the different lines. They are compiled together with the literature values in Tab. 5.4. The lines at 65 keV and 11 keV could already be observed in previous runs of CRESST [80]. The line at 2.6 keV could be observed for the first time in run 33 (see Fig. 5.5).

The ratios for the capture of electrons from the different sub-shells can be calculated using Eq. 5.2 and are presented in Tab. 5.5 together with the observed ratios. The energies of the different lines are reconstructed with an accuracy of $\lesssim 1\,\%$ and also the observed ratios agree with the theoretical

Table 5.5: Calculated and observed ratios for EC of ^{179}Ta.

	calculated ratio	observed ratio
L1/K	0.808	0.84 ± 0.02
L2/L1	0.0565	0.18 ± 0.02
M1/L1	0.2807	0.30 ± 0.01
N1/M1	0.27	—

prediction, with the exception of the L2/L1-ratio which is significantly too high. Assuming the theoretical prediction is correct, one possible explanation might be that there is an additional line with an unknown origin at the energy of the L2 line. From the calculated capture ratios, one would expect a line at 0.538 keV with an activity of 12.1 μBq due to the capture of electrons from the N1 shell. However, this line can not be observed since it lies too close to the energy threshold and its activity is too low.

To confirm the origin of these lines from ^{179}Ta a fit of the half-life of the decay is performed. For this, the data is split in time intervals of three months and the count rates of the lines due to electron capture from the different sub-shells are extracted by fitting the lines with Gaussians (over a locally flat background). Since the exposure is not necessarily homogeneous in every time interval (due to calibrations being performed or bad files), the mean of all timestamps is selected as the center of each interval and the standard deviation is used as error for the time axis. For the L2-line, the statistics is too small to extract meaningful count rates in the individual time bins, so it is omitted. A fit is performed to the sum of the count rates of the remaining lines as well as to the count rates of each line individually.

The half-life is fitted using two different methods: a least squares fit, which takes only the errors for the count rate into account, and orthogonal distance regression (ODR), which treats also the errors on the time. The conceptual difference is that in the standard least squares fit, the distance of the fit-curve to the data in y-direction is minimized whereas in ODR the distance which is minimized is orthogonal to the fit-curve. The results are summarized in Tab. 5.6. Overall, the difference between the results of the two methods is marginal.

The resulting value of the combined fit agrees within error with the literature value of 662 days. The same is true for the individual lines, albeit with larger errors due to the lower statistics. This confirms the origin of these lines from the EC decay of ^{179}Ta.

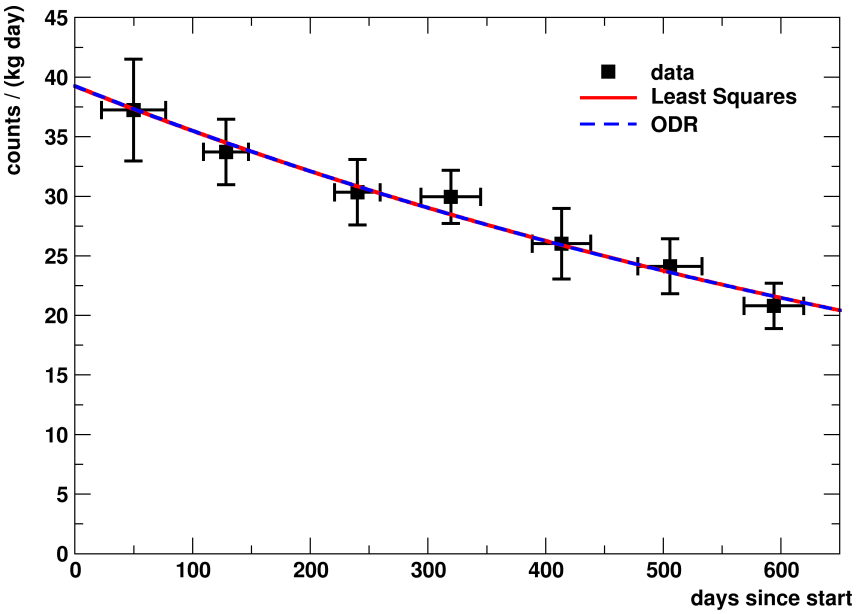

Figure 5.6: Sum of the count rates of the K-, L1- and M-shell capture of ^{179}Ta in TUM40 (black data points) over time together with a fit of an exponential decay using two different methods (solid red and dashed blue).

Table 5.6: Fitted half-lives for the EC decay of ^{179}Ta using data from detector TUM40.

	$T_{1/2}$ in days	
shell	least squares	ODR
combined	690 ± 134	689 ± 52
K	585 ± 116	584 ± 69
L1	879 ± 139	853 ± 184
M	574 ± 208	587 ± 195

5.2.4 Electron capture from ^{181}W

^{181}W decays via electron capture to ^{181}Ta with a half-life of 121 days and a Q-value of 188 keV [104]. In 75 % of all cases it decays to an excited state in the Ta nucleus and only in 25 % it decays directly to the ground state. If the electron capture decay ends in the excited state, a 6.72 keV γ-ray is emitted in addition to the x-ray cascade which leads to observable lines at 74.1 keV and 18.4 keV (see Fig. 5.5). In the data from detector TUM40, only the lines with associated γ-ray could be observed, the x-ray only lines are too weak. Since the L1-shell capture is only barely visible, the much less intense M1-shell capture is negligible. The observed energies and activities are compiled together with the

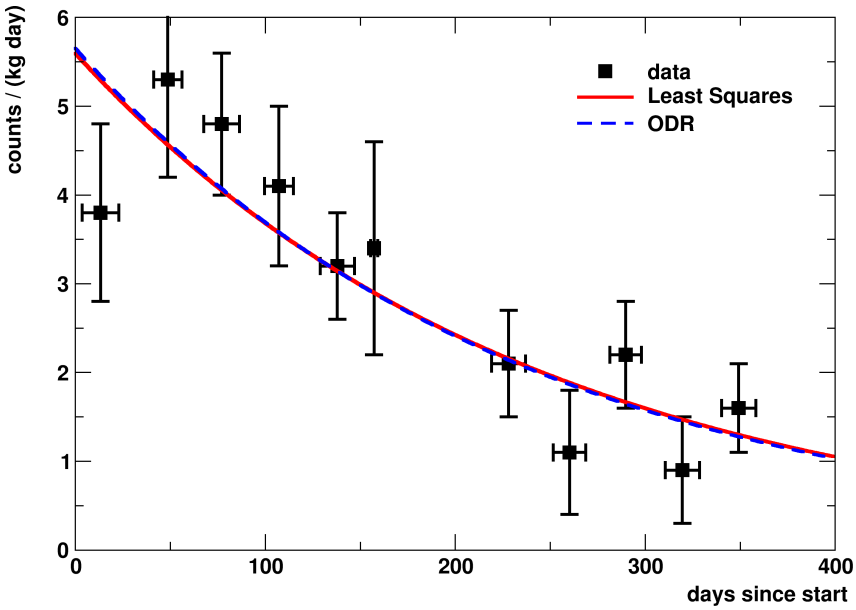

Figure 5.7: Count rate of the 74.1 keV line from K-shell electron capture with associated γ-ray emission from the EC decay of ^{181}W in TUM40 over time (black data points) together with a fit with an exponential decay using two different methods (solid red and dashed blue).

Table 5.7: X-ray binding energies, observed energies and activities for ^{181}W.

shell	E_{lit} in keV [104]	E_{obs} in keV	activity in μBq kg^{-1}
K + γ	74.136	73.7	34.7 ± 8.1
L1 + γ	18.402	18.0	6.9 ± 2.3
M1 + γ	9.428	—	—

literature values of the energies in Tab. 5.7. Again the reconstructed energies agree within a few percent with the theoretical predictions.

The capture ratios can be calculated as in the case of Hafnium above and are shown together with the observed ratios in Tab. 5.8. Here only the L1/K ratio could be observed which agrees within error with the calculated ratio.

The relatively short half-life of 121 days can be observed when looking at the K-shell peak with the associated γ-ray at 74 keV. Due to the shorter half-life compared to the ^{179}Ta decay discussed above, the data is split into time intervals spanning $\sim$ 1 month. The peak is then again fitted with a Gaussian in each time interval to determine the count rate taking the exposure of each time interval into account. The resulting data is fit with an exponential which yields a half-life of 166 ± 47 days for the least squares fit and 163 ± 43 days for the ODR method (see Fig. 5.7). Both values agree within error with the

Table 5.8: Calculated and observed ratios for EC of ^{181}W.

	calculated ratio	observed ratio
L1/K	0.22	0.20 ± 0.08
M1/L1	0.25	—

literature value quoted above.

In conclusion, the agreement of the fitted energies with the literature values, of the observed capture ratio with the predicted one and the extracted half-life with the literature value confirms the presence of ^{181}W in TUM40.

5.3 Sensitivity to Low Mass Dark Matter

First data obtained with the detector module TUM40/Michael, which uses an absorber crystal grown at the TU Munich, showed an unprecedented background level of $\sim 3-4\,\mathrm{cts\ keV^{-1}\ kg^{-1}\ d^{-1}}$ at low energies. Together with the low hardware trigger threshold of $\lesssim 1\,\mathrm{keV}$, this spurred interest in the sensitivity of this detector to dark matter masses below $10\,\mathrm{GeV}/c^2$, when performing a low threshold analysis taking into account all data down to the hardware threshold.

To assess the potential of such an analysis a series of toy Monte Carlo simulations have been performed. To simplify the calculations, a flat e^-/γ -background is assumed. This is justified since the optimum interval method used to calculate the resulting limits is rather insensitive to background from γ-lines because the recoil spectrum expected from dark matter has a different shape. Also, for the lowest masses only a small energy region above the threshold is relevant for the limit and such a small energy region can always be described locally by a flat background.

In this model, different parameters like energy threshold (0.3 keV, 0.6 keV and 1.0 keV), background level ($1\,\mathrm{ct\ keV^{-1}\ kg^{-1}\ d^{-1}}$, $3\,\mathrm{cts\ keV^{-1}\ kg^{-1}\ d^{-1}}$ and $10\,\mathrm{cts\ keV^{-1}\ kg^{-1}\ d^{-1}}$) and exposure (10 kg days, 20 kg days and 100 kg days) are varied and their effect on the resulting limits are studied.

One additional problem of analyzing low energy events is that the discrimination between electronic and nuclear recoils becomes harder for lower energies, since even for e^-/γ -events the light signal becomes very small. Thus the fraction of leakage from the e^-/γ -band is very large for the lowest energies. To soften the impact of leakage from the e^-/γ -band, different choices for the acceptance region in the energy-light yield plane have been studied in order to find a good compromise between accepting a large fraction of nuclear re-

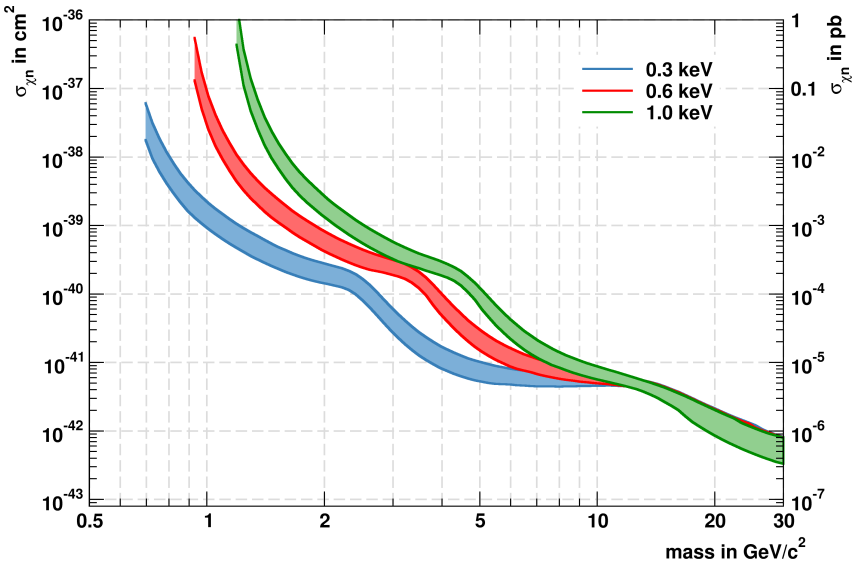

Figure 5.8: Central 90 % intervals of 10,000 simulated limits assuming a flat background of 3 cts keV^{-1} kg^{-1} d^{-1} an exposure of 100 kg days and thresholds of 0.3 keV, 0.6 keV and 1.0 keV.

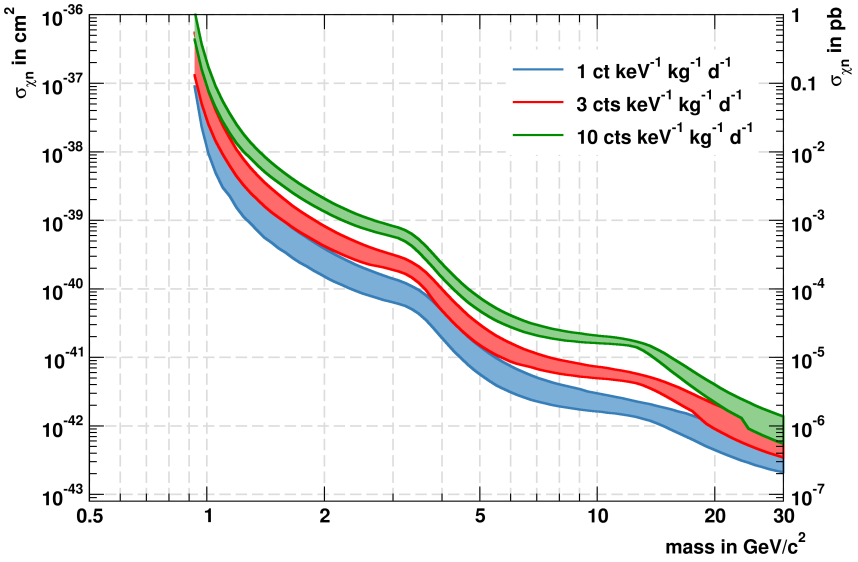

Figure 5.9: Central 90 % intervals of 10,000 simulated limits assuming a threshold of 0.6 keV an exposure of 100 kg days and a flat background with 1 cts keV^{-1} kg^{-1} d^{-1}, 3 cts keV^{-1} kg^{-1} d^{-1} and 10 cts keV^{-1} kg^{-1} d^{-1}.

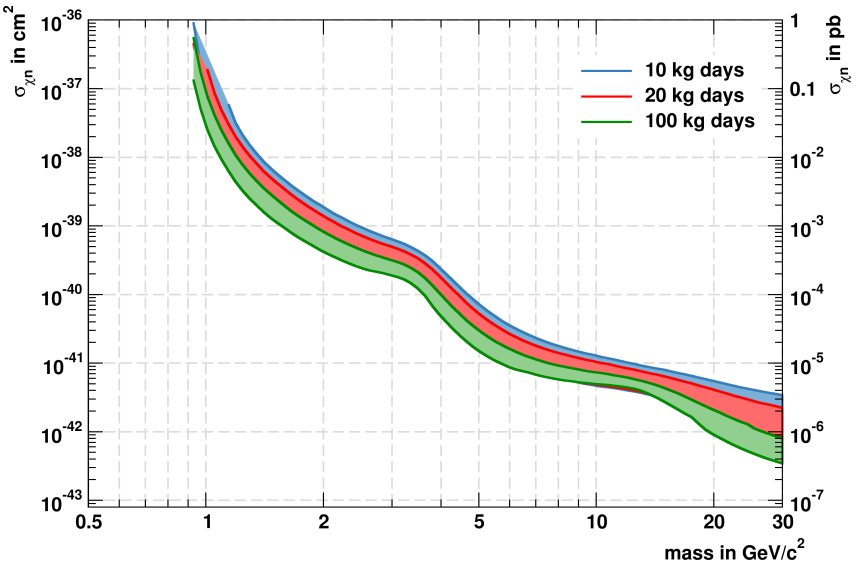

Figure 5.10: Central 90 % intervals of 10,000 simulated limits assuming a flat background of 3 cts keV^{-1} kg^{-1} d^{-1} a threshold of 0.6 keV and exposures of 10 kg days, 20 kg days and 100 kg days.

coils and reducing the amount of leakage. For the lower light yield bound the lower 99.5 % contour of the tungsten band was chosen. For the upper light yield bound three different choices have been investigated: the center of the oxygen band, the center of the tungsten band and the upper 90 % contour of the oxygen band.

For each set of parameters, 10,000 datasets were simulated taking the Poisson statistics of the number of expected events into account and the central 90 % interval of the resulting optimum interval limits was computed. Varying the threshold from 0.3 keV to 1.0 keV has the most drastic effect on the sensitivity to masses below $\sim 10\,\mathrm{GeV}/c^2$ (see Fig. 5.8) as one expects already from the shape of the recoil spectra. Variations of the background level have a marginal effect on the overall shape of the exclusion curves, a lower background level, however, results in an improved sensitivity across the entire mass range (see Fig. 5.9).

For low masses, the sensitivity does not scale proportionally to the increased exposure (see Fig. 5.10). This is because the sensitivity at low masses is limited by the number of e^-/γ -events leaking into the acceptance region. For the considered background level of 3 cts keV^{-1} kg^{-1} d^{-1} this number is already limiting the sensitivity at an exposure of a few 10 kg days. Lowering the background level allows for higher exposures thus increasing the sensitivity.

Finally the influence of the choice of the acceptance region has been studied (see Fig. 5.11). The acceptance region was defined to include energies between

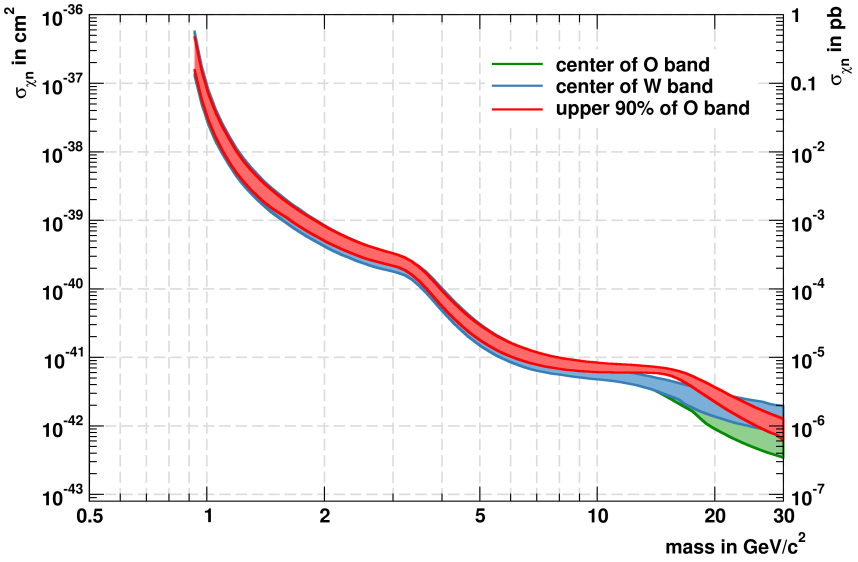

Figure 5.11: Central 90 % intervals of 10,000 simulated limits assuming a flat background of 3 cts keV^{-1} kg^{-1} d^{-1} an exposure of 100 kg days and a threshold of 0.6 keV for three different upper light yield bounds: center of the tungsten band, center of the oxygen band and the upper 90 % contour of the oxygen band.

the chosen threshold (0.6 keV for Fig. 5.11) and 40 keV. The lower light yield bound was kept fixed as the lower 99.5 % contour of the tungsten band. The influence of the three different upper light yield bounds on the sensitivity below 10 GeV/c^2 is negligible. This can be understood, because the sensitivity in this mass range is mainly limited by the residual background at low energies which in turn is given by the overlap of the e^-/γ -band with the acceptance region. Shrinking the acceptance region reduces this overlap, but since the overlap between e^-/γ -band and the recoil bands is close to 100 % at these energies, the expected number of signal counts is reduced by approximately the same amount as the number of background counts. This means the signal to background ratio, and thus the sensitivity, remains almost the same. Only for larger masses, when also higher energies become relevant, a small difference in sensitivity between the different light yield bounds can be observed, because at those higher energies the separation between the e^-/γ -band and the recoil bands can be exploited to improve the signal to background ratio. As a result, the best compromise between a high coverage of all three recoil bands and limiting leakage from the e^-/γ -band can be achieved by choosing the center of the oxygen band as the upper light yield bound.

As a conclusion, the studies show that the prospects for a low threshold analysis are promising and competitive sensitivities can be achieved with moderate

exposures of a few 10 kg days. The key parameters to achieve a high sensitivity are a low energy threshold and a low background level.

5.4 Limits on Low Mass Dark Matter

Following the encouraging results of the sensitivity studies presented in Sec. 5.3, a first result on low mass dark matter particles has been published using the initial non-blind training set data from detector TUM40 which contains an exposure of $\sim$ 30 kg days [66]. This detector has been chosen because it had the lowest energy threshold of all detectors at that time and additionally it showed the lowest level of e^-/γ -background.

As discussed in Sec. 4.4, the threshold of several detectors could be lowered during the run. Since the sensitivity studies show that a lower energy threshold has the potential to significantly increase the sensitivity, data from the detectors with the lowest thresholds (Lise, Daisy and TUM40) are used to improve on the first low threshold limit. The exposure of this second dataset amounts to $\sim$ 25 kg days for the conventional modules Lise and Daisy, which have a mass of $\sim$ 300 g and $\sim$ 20 kg days for TUM40, which has a mass of 249 g.

For all limits, the acceptance region begins at the measured trigger threshold and extends up to 40 keV and includes all events with light yields below the center of the oxygen band and above the lower $5\,\sigma$ contour of the tungsten band.

5.4.1 Results obtained with TUM40

The initial results obtained with TUM40 are based on the *training set* data, which were obtained between July 2013 and January 2014. The exposure of this data set is 29 kg days. As shown in Sec. 4.3.5, the rate of events passing the cuts to remove carrier-like events based on the random forest classifier (RF cut) is correlated with the trigger rate of low energy events. Since this rate steadily decreases, a second data set is defined (*low rate set*) which comprises data taken between December 2013 and July 2014 and contains a slightly larger exposure of 35 kg days. Finally, a third data set (*low threshold set*) is defined, consisting of data taken after lowering of the hardware energy threshold from 650 eV to 405 eV in September 2014 and before the end of the run in May 2015. For this data set, files during the bursts of the trigger rate at low energies (from file 200 onwards in Fig. 4.19) are discarded, leaving an exposure of 30 kg days.

Fig. 5.12 shows the data of detector TUM40 from each of the three data sets in the energy-light yield plane. All events lying in the respective acceptance

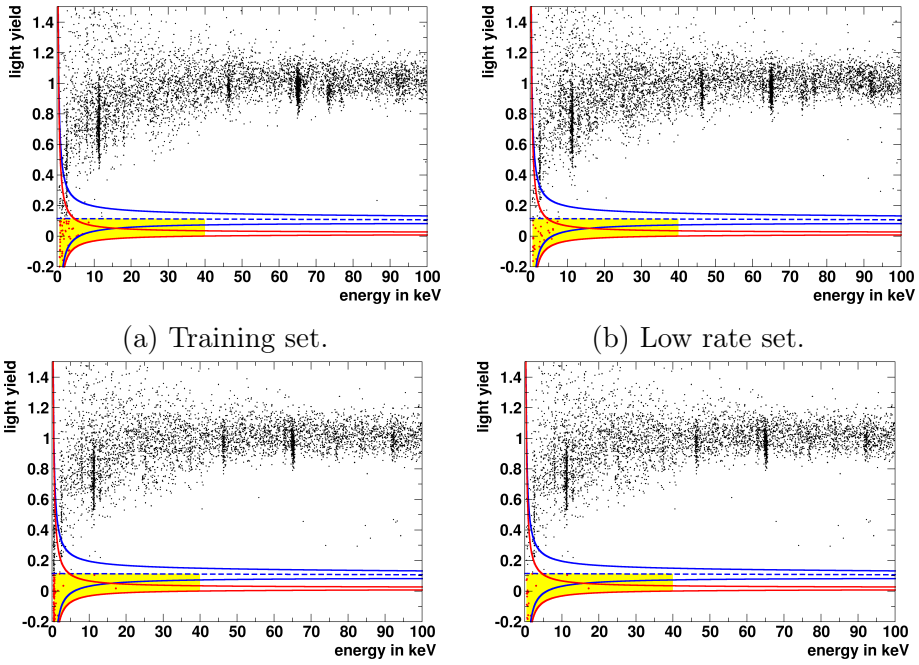

(a) Training set.

(b) Low rate set.

(c) 400 eV RF cut only.

(d) 400 eV additional cuts.

Figure 5.12: Data from various data sets of module TUM40/Michael displayed in the energy-light yield plane. The solid blue (red) curves indicate the upper and lower 90 % contours of the oxygen (tungsten) band. The dashed blue line corresponds to the center of the oxygen band. The events in the acceptance region (shaded in yellow) are highlighted in red.

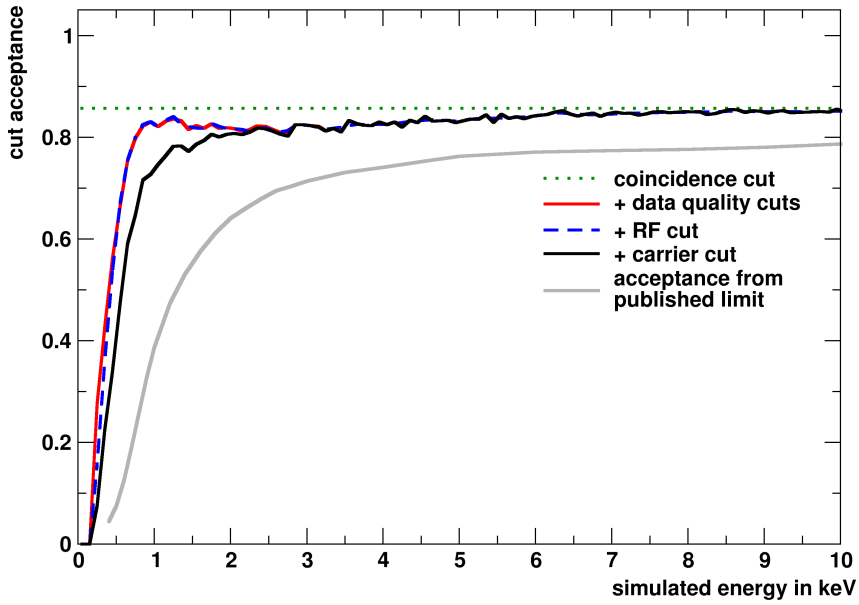

Figure 5.13: Cut acceptance for nuclear recoil events for detector TUM40 after successive application of the different selection criteria. The gray curve shows the final cut acceptance for the limit published in [66].

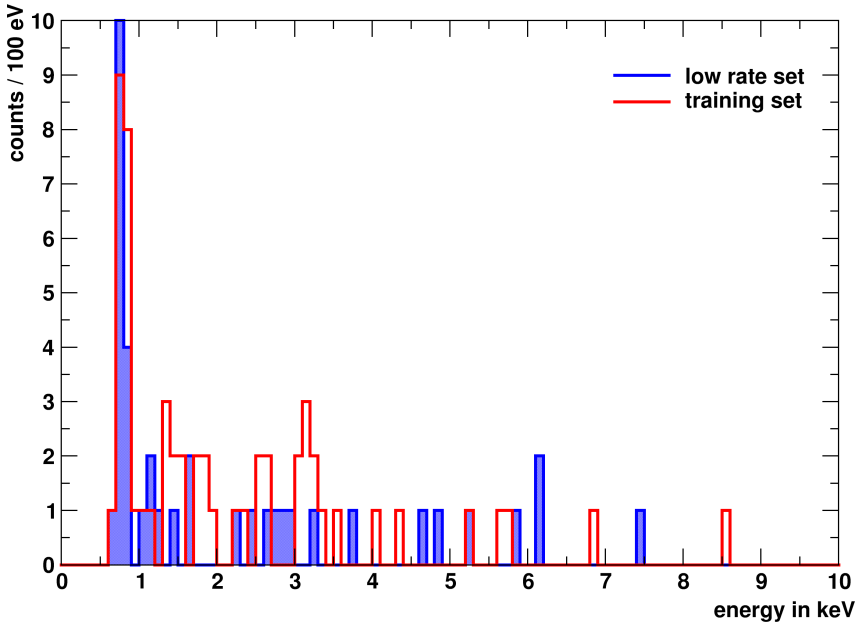

Figure 5.14: Histogram of the energies of all events in the acceptance region for the data sets with a threshold of 605 eV from detector TUM40.

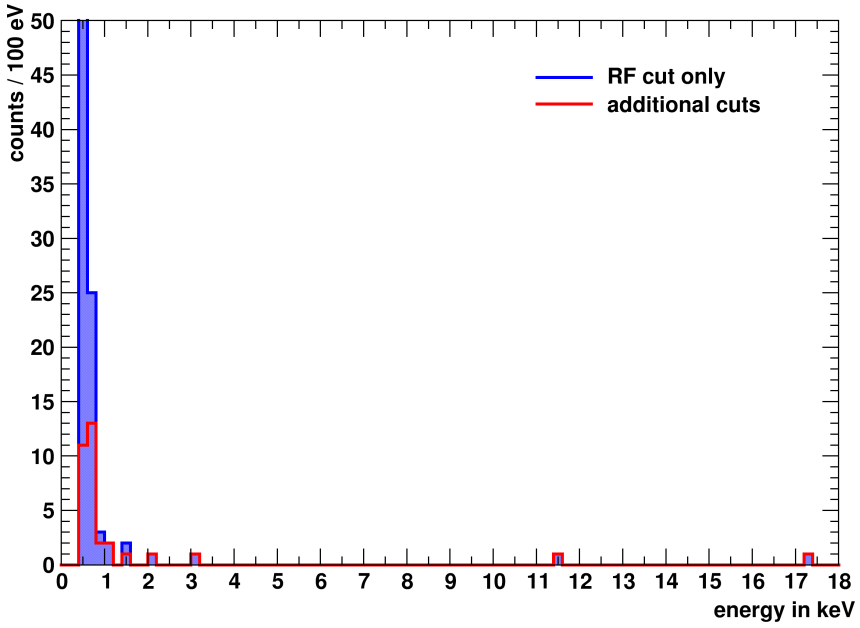

Figure 5.15: Histogram of the energies of all events in the acceptance region for the data set with lowered threshold from detector TUM40 before (blue) and after (red) applying additional cuts on carrier-like events.

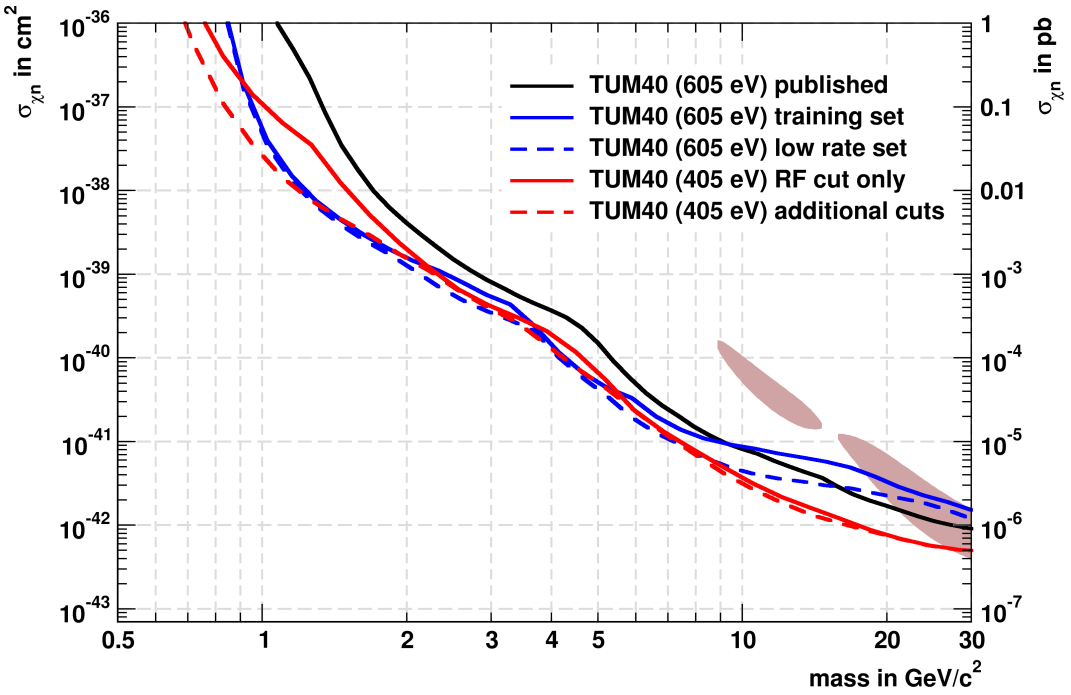

Figure 5.16: 90 % C.L. upper limits on the dark matter-nucleon cross section obtained with detector TUM40. The solid black line corresponds to the limit published in [66] which is based on the training set data. The solid blue curve shows the limit obtained from the identical training set data in this work with a threshold of 605 keV, the dashed blue curve shows the limit from the data set before lowering the threshold with a cut on the total rate. The solid red curve corresponds to the limit obtained in this work after lowering the threshold to 405 eV using only the RF cut to remove carrier-like events, the dashed red curve shows the limit based on the same data set as the solid red curve but with additional cuts to remove carrier-like events. The regions shaded in light red correspond to the parameter space compatible with the excess observed in run 32 [53].

regions (shaded in yellow) are conservatively considered as dark matter candidates. Fig. 5.14 shows histograms of the energies of all accepted events from the two data sets with a threshold of 605 eV. The main difference between the training set and the low rate set lies in the number of counts above ~ 1 keV which is somewhat lower in the low rate set.

Histograms of the energies of accepted events from the low threshold set are shown in Fig. 5.15. The difference between the two histograms are the cuts applied on the data: for the blue histogram, only the RF cut is applied to remove carrier-like events, for the red histogram also additional cuts (as described in Sec. 4.3.5) are applied. Without the additional cuts the number of counts below 1 keV is more than a factor of 10 larger. The additional cuts, however, also lead to a decrease in the cut acceptance at low energies. This is illustrated in Fig. 5.13, which shows the energy dependent survival probability as determined from artificially generated events (cf. Sec 4.3.4) after the successive application of the different selection criteria. It shows, that the RF cut introduces almost no additional loss in acceptance over the data quality cuts while the additional carrier cuts lead to a significant reduction of the acceptance starting at energies below 2 keV.

For all four sets of accepted events shown in Figs. 5.14 and 5.15, the optimum interval method described in Sec. 4.6 is used to calculate an upper limit on the dark matter-nucleon cross section, taking into account the respective cut acceptance (see Fig. 5.13) and exposure. The resulting limit curves are drawn in Fig. 5.16 (red and blue curves) together with the limit published in [66] (black). The published limit is also based on the training set data but comes from a different analysis where the main difference to this work are the different selection criteria and thus also the cut acceptance. The limits drawn in blue are based on the training set (solid blue) and the low rate set (dashed blue). The two curves only differ at higher masses, where the low rate set gives a higher sensitivity, which is related to the lower number of events observed at energies above 1 keV (see Fig. 5.14). Both of these limits result in a significantly higher sensitivity at low dark matter masses compared to the published limit which is a direct consequence of the higher cut acceptance of the RF cut developed in this work (cf. Sec. 4.3.6) with respect to the carrier cut used in [66].

The limits obtained with detector TUM40 from the data taken after lowering the threshold are drawn in red in Fig. 5.16. They are based on the data shown in Fig. 5.15. The limit obtained with the RF cut only (solid red) is significantly worse at low masses than the limit using additional carrier cuts (dashed reds), which reflects the higher number of events at low energies. This shows that for this data set the RF cut is not sufficient to remove carrier-like events. If one applies the additional cuts, the lower threshold compared to the training

set and low rate set limits extends the sensitivity to lower masses. At higher masses, the different cuts lead to almost identical limits which are better than the ones obtained with the training set or low rate set which is due to the lower amount of events observed above 1 keV.

In summary, the higher cut acceptance of the RF cut developed in this work leads to an improved limit compared to the one published in [66] which is based on the identical data. For the data obtained with the lowered threshold, the RF cut is not sufficient to remove all carrier-like events and needs to be supplemented by additional cuts. Although these cuts lead to a lower cut acceptance, the resulting limit improves and extends the sensitivity to masses as low as $0.7\,\mathrm{GeV}/c^2$.

5.4.2 Results obtained with Lise and Daisy

The lowest threshold of all detectors in run 33 (311 keV) could be achieved with detector Lise. The data obtained just after lowering the threshold is shown in Fig. 5.17, a histogram of the energies of all accepted events is shown in Fig. 5.18. In both of these plots the contamination around 6 keV due to the accidental illumination with an ^{55}Fe source is clearly visible. Another thing which stands out is the significantly larger width of the bands compared to TUM40 for example. This is caused by the exceptionally low energy resolution of the light detector of this module, which leads to a large overlap between the e^-/γ -band and the nuclear recoil bands up to $\sim 20\,\mathrm{keV}$. The resulting limit, shown in red in Fig. 5.23, however, does not suffer too much from the large number of leakage events in the acceptance region. This can be understood if one looks at the shape of the spectrum of accepted events shown in Fig. 5.18, which is relatively flat down to the threshold energy, whereas a dark matter signal at these low masses would rise very steeply towards low energies. The contamination due to the ^{55}Fe-source does not affect the sensitivity for masses below $\sim 5\,\mathrm{GeV}/c^2$, which can be seen by comparing the limit to the one obtained with TUM40.

The discrepancy to the published limit (black curve in Fig. 5.23), which is based on the same data, comes from the different data selection. The analysis chosen for the publication [65] uses a much more aggressive cut on the rise time of the pulses. This leads to a reduced acceptance at low energies (see Fig. 5.21) but also a much lower number of accepted events at low energies.

Detector Daisy has the second lowest threshold in run 33 (340 keV), the data of this detector is shown in Fig. 5.19. Fig. 5.20 shows a histogram of the energies of all accepted events. The better separation between nuclear recoils and e^-/γ -events of detector Daisy compared to detector Lise results in much less events in the acceptance region of detector Daisy. Especially above 1 keV,

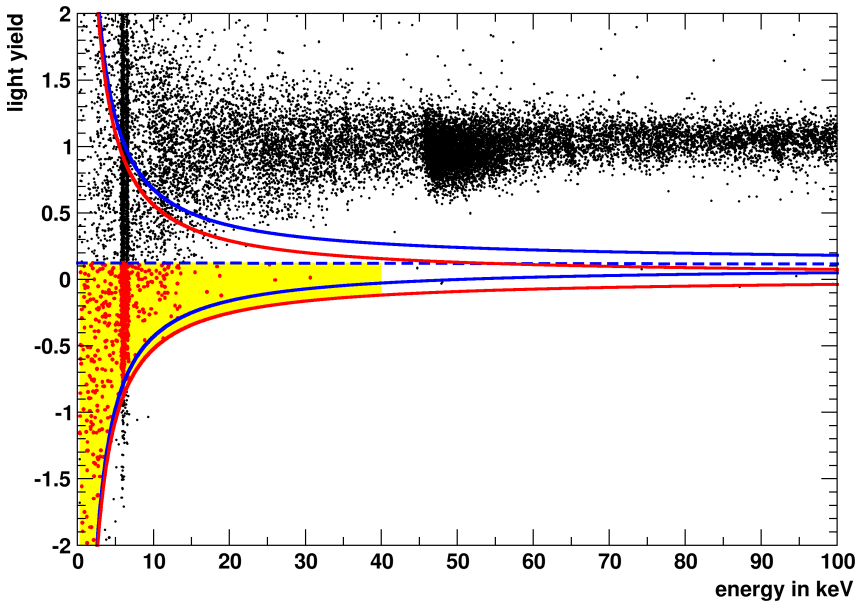

Figure 5.17: Data from detector Lise displayed in the energy-light yield plane. The solid blue (red) curves indicate the upper and lower 90 % contours of the oxygen (tungsten) band. The dashed blue line corresponds to the center of the oxygen band. The events in the acceptance region (shaded in yellow) are highlighted in red.

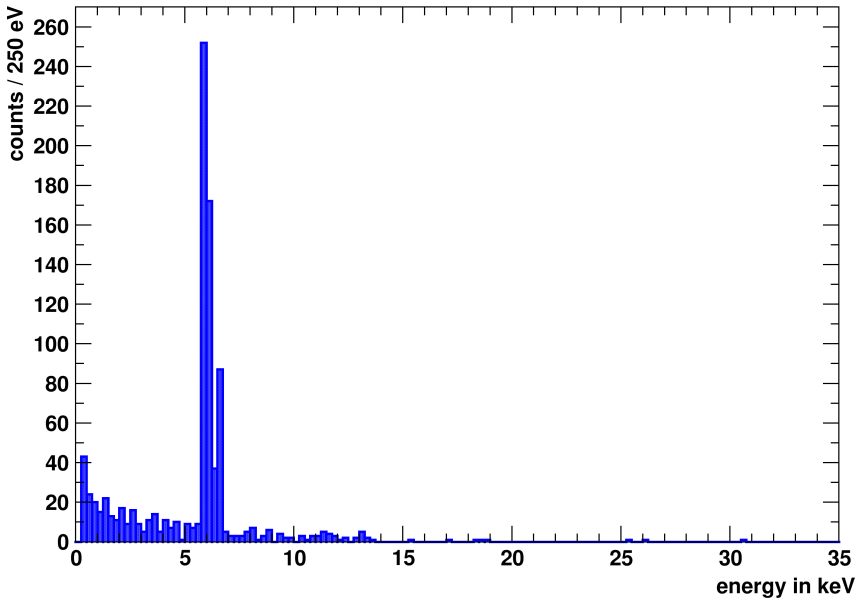

Figure 5.18: Histogram of the energies of all events in the acceptance region of detector Lise.

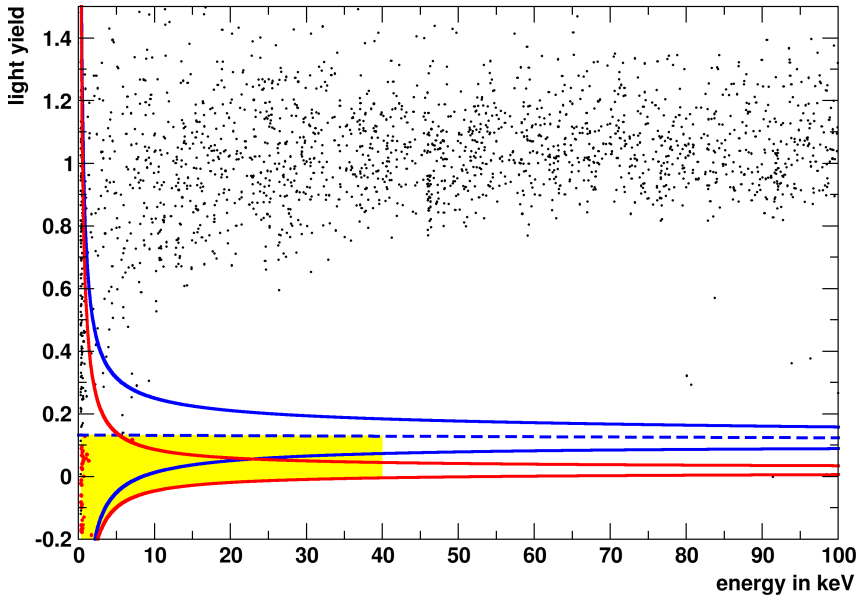

Figure 5.19: Data from detector Daisy displayed in the energy-light yield plane. The solid blue (red) curves indicate the upper and lower 90 % contours of the oxygen (tungsten) band. The dashed blue line corresponds to the center of the oxygen band. The events in the acceptance region (shaded in yellow) are highlighted in red.

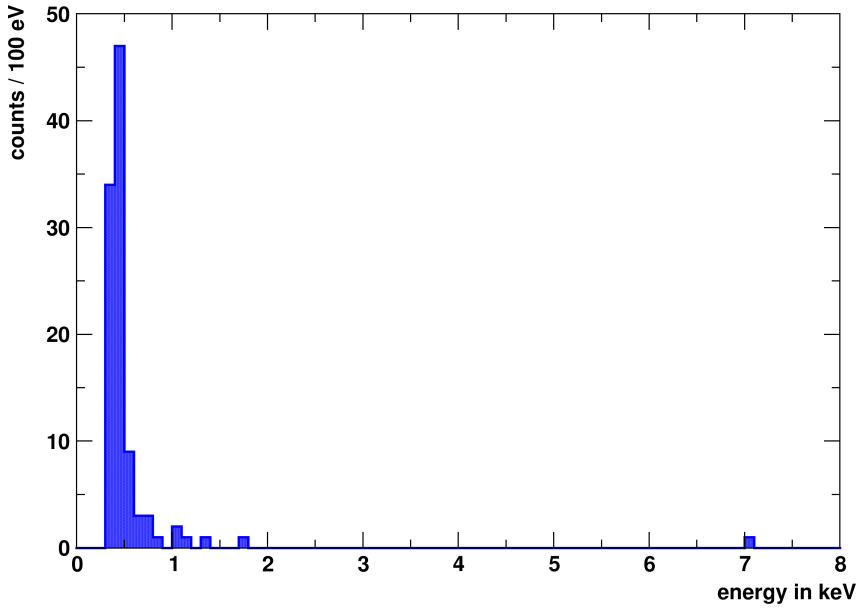

Figure 5.20: Histogram of the energies of all events in the acceptance region of detector Daisy.

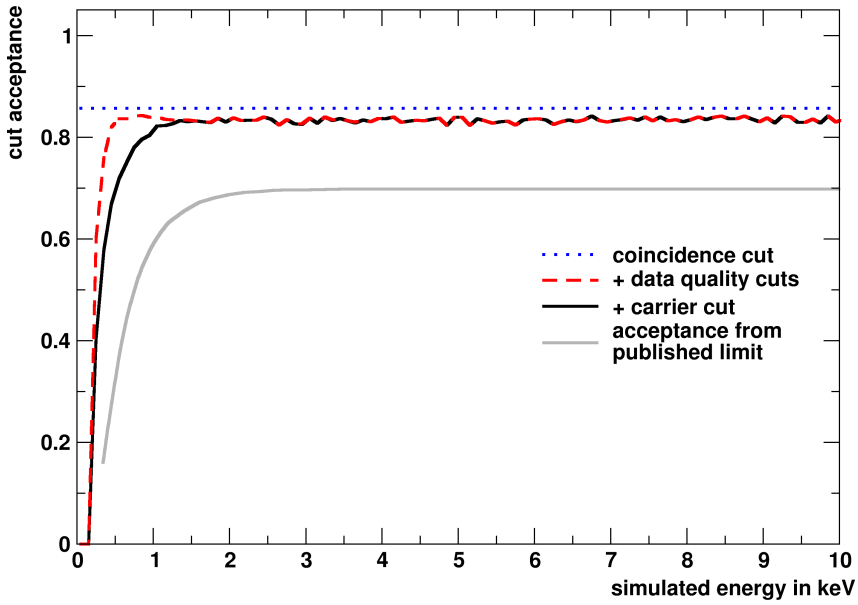

Figure 5.21: Cut acceptance for nuclear recoil events for detector Lise after successive application of the different selection criteria. For comparison, the final acceptance from the published analysis [65] is shown in gray.

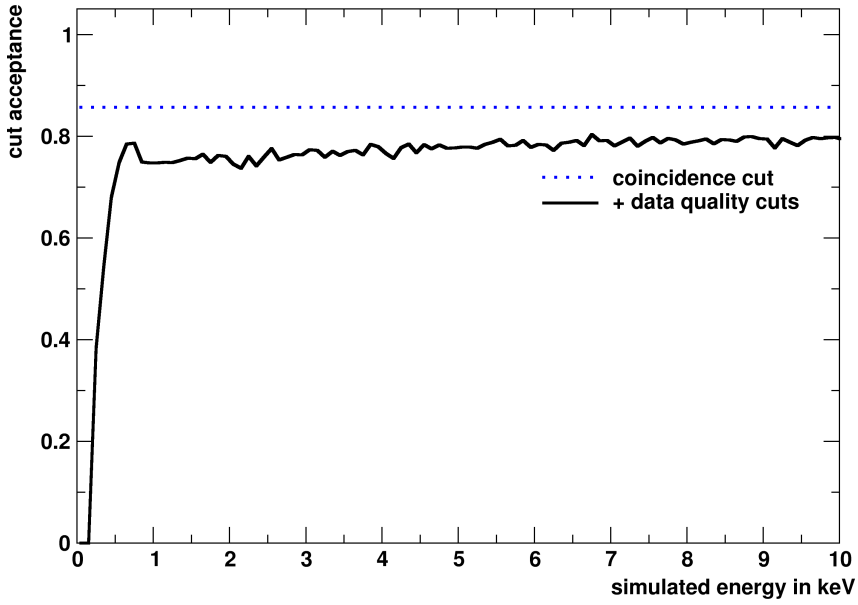

Figure 5.22: Cut acceptance for nuclear recoil events for detector Daisy after successive application of the different selection criteria.

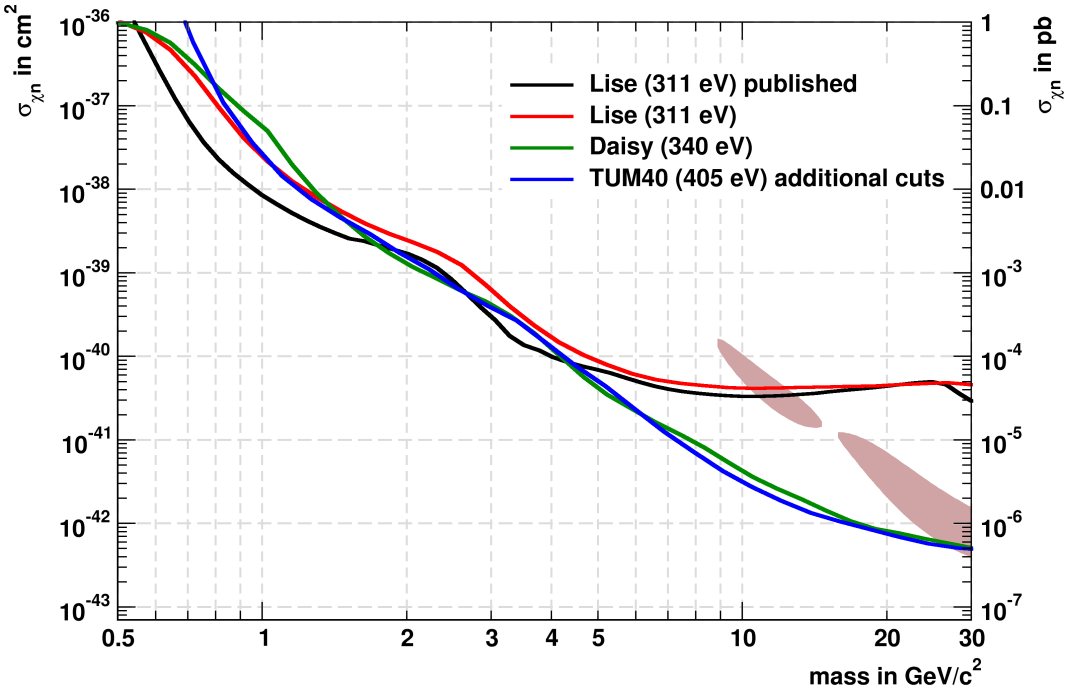

Figure 5.23: 90 % C.L. upper limits on the dark matter-nucleon cross section obtained with detectors Lise, Daisy and TUM40. The red curve shows the limit from detector Lise obtained in this work, the black line corresponds to the limit published in [65] which is based on the same data. The green curve shows the limit obtained from detector Daisy obtained in this work. The blue curve corresponds to the limit obtained with TUM40 after lowering the threshold with additional cuts to remove carrier-like events applied. The regions shaded in light red correspond to the parameter space compatible with the excess observed in run 32 [53].

where there are very few events. This leads to a superior sensitivity (green curve in Fig. 5.23) for masses above $5\,\mathrm{GeV}/c^2$ compared to Lise. Although the absolute number of accepted events below 2 keV is less than in Lise, the steep rise of the energy spectrum towards low energies prevents a better sensitivity.

5.4.3 Conclusions

These results show, that due to their low energy threshold for nuclear recoils, CRESST-II detectors have a great potential to detect light dark matter particles below $\sim 10\,\mathrm{GeV}/c^2$. To achieve competitive sensitivities in this mass range, already moderate exposures ($\mathcal{O}(10)$ kg days) are sufficient. Much more important than a large exposure are a low energy threshold and a low level of residual background at lowest energies. Since discrimination of nuclear recoils and e^-/γ -events becomes increasingly harder at low energies, this essentially means that the overall e^-/γ -background has to be reduced.

The results obtained with detector Lise, however, show, that under certain circumstances some level of background can be tolerated without affecting the sensitivity too much. The region in the spectrum which has the biggest impact on the sensitivity is of course the one just above the threshold. If the the background level is rising towards the threshold, this can drastically reduce the sensitivity, since this behavior mimics the effect expected in the presence of a dark matter signal. A flat background in this region leads to a higher sensitivity even if the number of counts might be slightly higher.

In the same vein, γ-lines have limited impact on the sensitivity, even if they are rather intense (such as the ^{55}Fe contamination in detector Lise), as long as their energies are sufficiently far above the threshold.

For the future it will be important to develop a detailed understanding of the backgrounds, especially in the sub-keV region. This would enable the use of maximum likelihood techniques, which promise higher sensitivities and are essential for a possible discovery, since the optimum interval method used in this work can only be used to set limits.

5.5 Momentum Dependent Dark Matter

For the results discussed so far, it has been assumed that the interaction between dark matter and nuclei is scalar and spin-independent. Although this is the most general interaction one can imagine, there exist other types of interactions which might be realized in nature. The exact nature of the coupling between dark matter and nuclei is only defined for a specific dark matter model. There are, however, several attempts to treat dark matter scattering

in an effective field theory approach [105, 106, 107], which allows to constrain all possible couplings between normal matter and dark matter. Models with alternative couplings are also put forward by theorists in attempts to reconcile conflicting experimental results, e.g. the positive indications of DAMA, CoGeNT, etc. with the null results from Xenon100 and LUX [108, 109].

More recently, dark matter with a coupling which depends on the exchanged momentum q between the dark matter particle and the nucleus has been invoked to resolve a conflict between helio-seismological data and the standard solar model [110, 111]. In particular, observables like the depth of the convection zone, the sound speed profile, the surface helium abundance, and small frequency separations are in tension with predictions from solar models using updated values for the chemical composition of the sun. One possibility to alter these observables is to introduce dark matter particles, captured gravitationally in the sun, which affect energy transport processes in the sun. The build up of a significant abundance of dark matter in the sun is only possible if self-annihilation of the dark matter particles is suppressed like e.g. in asymmetric dark matter models (cf. Sec. 1.2). The study in [111] shows, that the addition of dark matter particles to the sun can indeed improve the agreement with the observed parameters. For the standard SI case, however, the region is already excluded by direct detection experiments. Therefore, also other couplings which depend on the transferred momentum q or the relative velocity of the dark matter particles v_{rel} were studied. The best agreement was found for a spin-independent coupling of the form $\sigma = \sigma_0 \left(\frac{q}{q_0}\right)^2$, with $q_0 = 40\,\mathrm{MeV}$ and $\sigma_0 = 10^{-37}\,\mathrm{cm}^2$ for a dark matter mass of $3\,\mathrm{GeV}/c^2$, which so far is not excluded by direct detection experiments.

Using the same data and cut acceptances as for the low mass dark matter limit published in [65], 90 % C.L. limits on the dark matter-nucleon cross section are obtained for the case of q^2- and q^4-dependent spin-independent scattering and published in [98]. In this work, limits obtained with the training set data of TUM40 and for detector Lise are derived. These limits are based on the same data and cut acceptances presented in Sec. 5.4.

To account for the momentum dependent coupling, only the cross section in Eq. 2.8 has to be adjusted as follows:

$$\sigma = \sigma_0 \left(\frac{q}{q_0}\right)^n \tag{5.3}$$

where σ_0 is the dark matter-nucleon cross section, q is the transferred momentum, q_0 is a normalization constant, which is set to 40 MeV in accordance with [111], and n is the order of the coupling. For $n > 0$, this causes a suppression of the rate at low energies (which correspond to small transferred

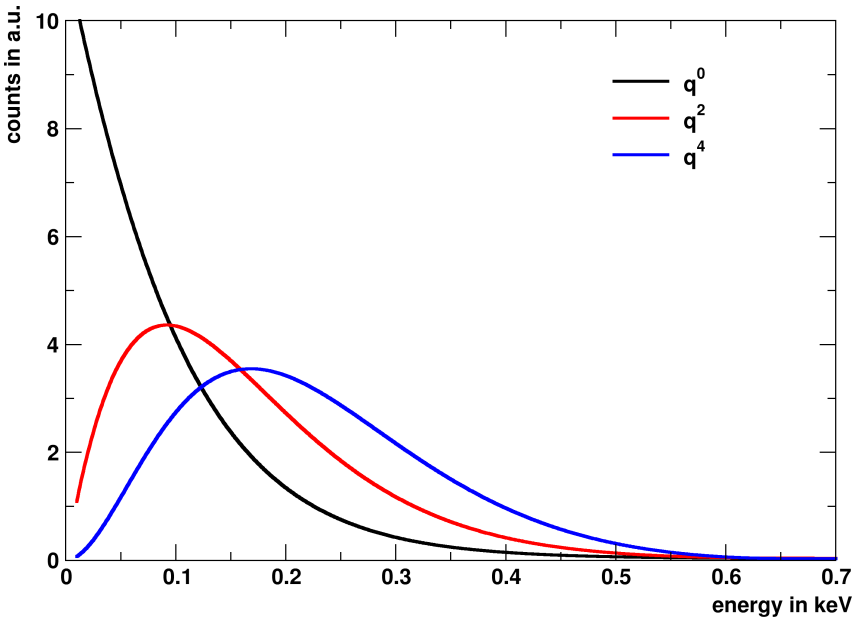

Figure 5.24: Calculated recoil spectra for dark matter particles with a mass of $3\,\mathrm{GeV}/c^2$ scattering off $CaWO_4$. The black curve corresponds to the default spin-independent spectrum. The red and blue curves show the effect of the different powers of q on the shape of the recoil spectrum. To visualize this effect, the spectra are normalized to the same number of counts. Note, however, that especially for low masses the absolute count rate for the q^2 and q^4 case are strongly suppressed.

momenta q), leading to peaked recoil spectra. Fig. 5.24 shows the different shapes of the spectra for $n = 0, 2, 4$. But not only the shape is affected, also the total rate is reduced for higher n.

The goal is to compare the limits to the results of [111]. Therefore the slightly higher value for the local dark matter density of $0.38\,\mathrm{GeV\ cm^{-3}}$ used in [111] is adopted instead of the canonical value of $0.3\,\mathrm{GeV\ cm^{-3}}$ introduced in Sec. 2.1.

The limits obtained with TUM40 and Lise are then compared to the results of [111], which are displayed using the global χ^2 as defined in [111] as a function of dark matter mass and dark matter-nucleon cross section (see Fig. 5.25). The heat maps are reproduced using data published alongside the paper. They differ slightly from the figures in the publication (Fig. 16 in [111]) as it seems that not all data points are included. This results in white areas, especially at low masses and large cross sections. The areas shaded in light blue indicate the parameter space where the authors claim that the fit did not converge properly (the areas are extracted from Fig. 16 in [111]). The best fit points are highlighted in green.

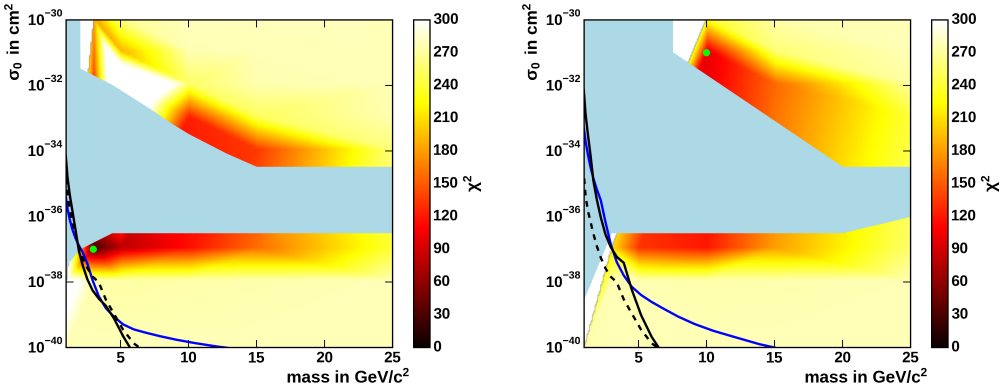

(a) Spin-independent $\propto q^2$. (b) Spin-independent $\propto q^4$.

Figure 5.25: 90 % C.L. upper limits on the spin-independent dark matter - nucleon cross section for q^2- and q^4-dependent scattering. The resulting limit from detector Lise is shown in solid blue, the limits from detector TUM40 are drawn in solid black (training set data) and dashed black (data after lowering threshold). The exclusion curves are compared to the solar models from [111]. The heat maps show the combined χ^2 value for different combinations of dark matter mass and dark matter-nucleon cross section (reproduced with data from [111], cf. Fig. 16 therein). The respective best fit points are indicated in green and are excluded by the limits obtained with both detectors.

Both the q^2- and the q^4-dependent best fit points are excluded by the limits obtained with TUM40 and Lise, ruling out the proposed model. For the future it will be interesting to also investigate the other couplings discussed in [111], or directly employ the EFT formalisms presented in [105, 106, 107].

5.6 Sensitivity Studies for the Future Strategy

In Sec. 5.4 unprecedented sensitivities for dark matter masses around $1\,\mathrm{GeV}/c^2$ and below are presented. Each result is obtained with a single detector and very limited exposure ($\mathcal{O}(30)$ kg days). The achievable sensitivity in this mass range is, however, ultimately limited by the e^-/γ -background leaking into the acceptance region. So, with the current performance of the detectors, the sensitivity at these low masses can not be further increased by simply acquiring more exposure. One thing to keep in mind is, that this kind of low threshold analysis was not foreseen in the preparation for this run, so the detectors which are used in this work are in no way optimized for low mass dark matter particles. The goal of these sensitivity studies is to find out which parameters have the most influence on the sensitivity at low masses to help guiding the design of a detector optimized for low dark matter masses.

The results of the sensitivity studies outlined in Sec. 5.3 already show, that the most crucial parameters which influence the sensitivity are the energy threshold and the residual background level at low energies which both have to be as low as possible. Reducing the residual background level can be done in two ways: by reducing the overall level of e^-/γ -background or by improving the discrimination between e^-/γ - and nuclear recoil events. To study the interplay between these three parameters (energy threshold, background level and discrimination power), a series of simplified Monte Carlo simulations (analogous to Sec. 5.3) are performed. For each combination of parameters, 10,000 limits are calculated and the central 90 % interval is extracted.

5.6.1 Improved Performance

The performance of TUM40 (cf. Sec. 5.4) is taken as a baseline, based on which different possible improvements are investigated. To simplify the calculations, the e^-/γ -background is assumed to be flat, with a level of 4 cts kg^{-1} keV^{-1} d^{-1}. To validate this approach, the result of this simulation is shown in Fig 5.26 (red band) and is compared to the limit obtained with TUM40 in Sec. 5.4 (black line). At low masses the background only simulation overestimates the sensitivity, which is somewhat expected, since the cut acceptance in the simulation is assumed to be independent of the energy, whereas the actual acceptance for the TUM40 result decreases below 1 keV (see Fig. 5.13). In addition, the simulation does not account for the additional background due to carrier-like events, which make the energy spectrum of accepted events rise towards the energy threshold. Although both of these effects are straightforward to implement in the simulation, it has been chosen to stick to the simplified version, since the modeling of the cut acceptance for a lowered energy threshold in particular would introduce an additional degree of freedom. Thus one needs to keep in mind that these simulations have the tendency to result in somewhat optimistic sensitivities at the low mass end.

As already mentioned above, the biggest impact on the sensitivity to low dark matter masses can be achieved by lowering the energy threshold. The easiest way to do this with a cryogenic detector is to reduce the mass of the absorber, thereby reducing the heat capacity and increasing the signal height. The downside to lowering the mass of the absorber is that one needs more individual modules to achieve the same total mass, requiring a larger number of readout channels which can become prohibitively expensive. In addition, the ratio of surface to volume of the absorber increases, which may lead to a higher rate of surface related backgrounds per unit mass. However, since a lower threshold is much more important than a high exposure, it is possible to reduce the mass of each module from 250-300 g to $\sim$ 25 g and still be able

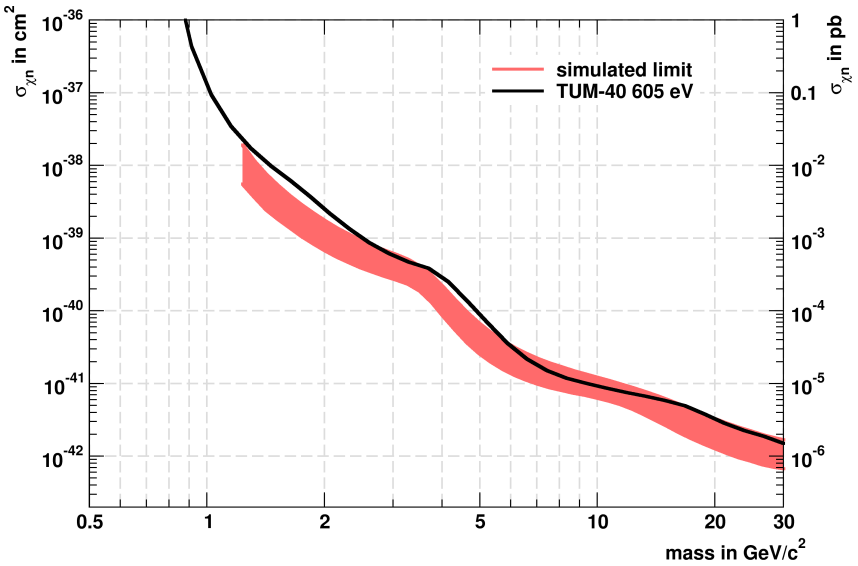

Figure 5.26: 90 % C.L. upper limit on the dark matter-nucleon cross section obtained with detector TUM40 (black line), compared with the result of the simplified Monte Carlo model (red band).

to acquire enough exposure. By doing so one expects to reach thresholds of 100 eV or even lower. This has already been confirmed by test measurements with prototype detectors [112]. For the sensitivity studies, two scenarios are studied: a conservative threshold of 100 eV and a more optimistic value of 50 eV.

Reducing the dimensions of the absorber also allows to reduce the dimensions of the light detector, which should lead to similar gains in sensitivity of the light detector. In addition, there will be less scattering and self-absorption of scintillation light in the absorber, which leads to a higher light output. Together, this causes a reduced width of the e^-/γ - and nuclear recoil bands and thus a higher discrimination power. For the sake of these simulations, the following assumptions are made: the amount of light detected is increased by a factor of two with respect to TUM40 and the signal to noise ratio of the corresponding light detector is increased by a factor of two as well (again with respect to the corresponding light detector Michael). This is implemented by adjusting the relevant parameters of the band description introduced in Sec. 4.5.2. As a reminder, the width of the bands as a function of detected light is parameterized as follows:

$$\sigma_L(L) = \sqrt{S_0 + S_1 L + S_2 L^2} \tag{5.4}$$

where S_0 describes the baseline noise, S_1 corresponds to the photon statistics and S_2 models an eventual position dependence. The increased light output

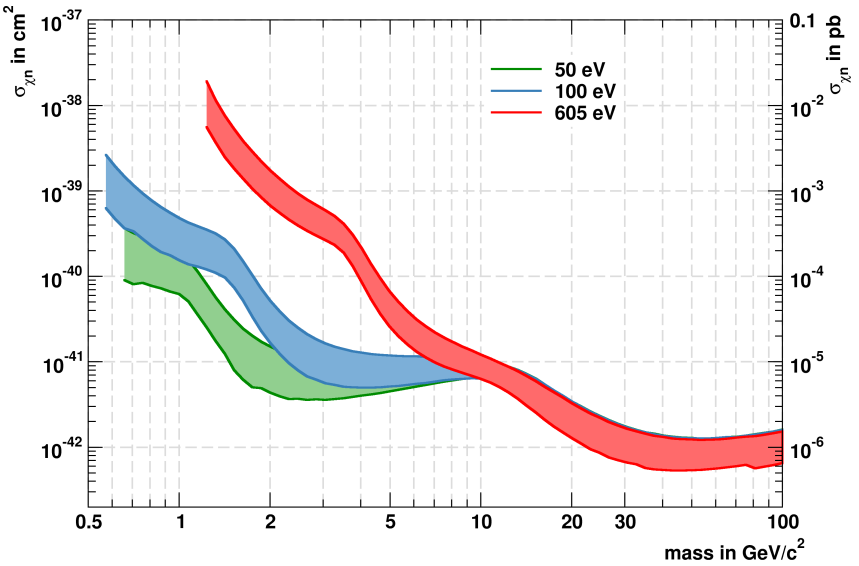

Figure 5.27: Results of the simplified Monte Carlo model for three different energy thresholds.

affects both S_0 and S_1, since a larger signal reduces the influence of the baseline noise and reduces the uncertainty due to the photon statistics, whereas the increased sensitivity of the smaller light detector only affects S_0. Thus, for the assumed improved performance the S_0 parameter is reduced by a factor of four (a factor of two each for the higher light output and the increased sensitivity) and the parameter S_1 is divided by two.

The majority of the observed e^-/γ -background is believed to be caused by radioactive impurities introduced to the crystal during the production process. In recent years, a lot of effort was put in the production of radio-pure $CaWO_4$ crystals at TU Munich. First crystals grown from radio-pure starting materials were installed during run 33 showing unprecedented levels of radio-purity. In order to further reduce radioactive contaminations, a dedicated cleaning procedure for the raw materials has been developed, targeting mainly uranium and thorium isotopes. First crystals produced from this purified powder are ready to be installed in the upcoming run 34. For the simulations an improvement of the background level of a factor of 10 (with respect to TUM40) is assumed. In addition to the improved background, also the current background of TUM40 and, as a worst case scenario, a 10 times higher background is considered (e.g. significant impact of surface backgrounds due to the higher surface to volume ratio of the smaller crystals).

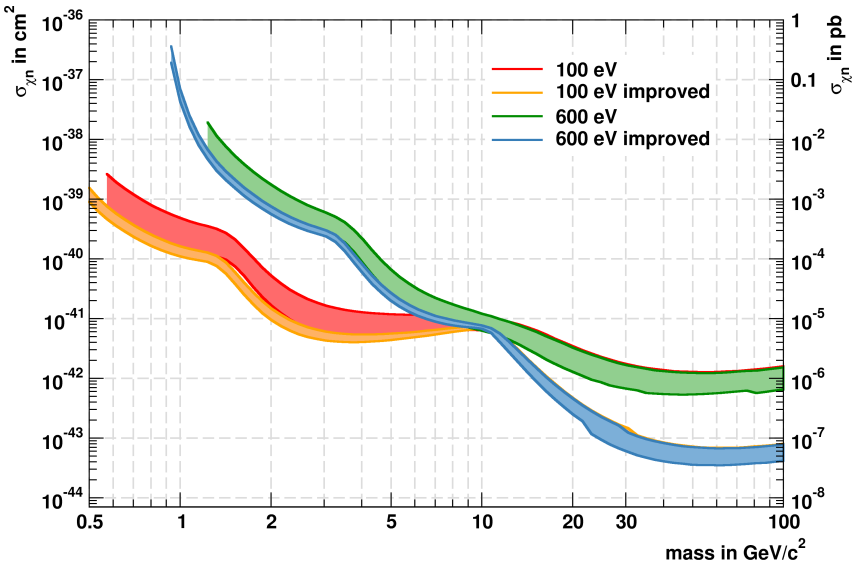

Figure 5.28: Result of the simplified Monte Carlo model comparing the existing performance of the light channel to the improved model for two different energy thresholds.

5.6.2 Results

Fig. 5.27 shows again the effect of lowering the energy threshold from 605 eV to either 100 eV or even 50 eV, while assuming the background level and discrimination power as in run 33. It can be seen that the sensitivity below 10 GeV/c^2 is significantly improved by the lower thresholds, whereas the sensitivity above 10 GeV/c^2 remains unaffected. This can be understood in conjunction with Fig. 5.28, where the effect of the improved discrimination (as defined above) is studied for two different energy thresholds (100 eV and 600 eV). These plots show that the improvements in energy threshold and discrimination power are independent of each other. The energy threshold only affects the sensitivity below 10 GeV/c^2, whereas the improved discrimination affects only the sensitivity at higher masses. The reason for this is that the discrimination introduces a second energy threshold, which is higher than the hardware threshold, above which the acceptance region for dark matter candidates remains essentially free from e^-/γ -leakage. This discrimination threshold becomes lower, the higher the discrimination power and thus leads to an improved sensitivity for dark matter masses which mainly cause recoils above this threshold. For lower dark matter masses, the sensitivity is reduced due to the leakage of events from the e^-/γ -band, and the lowest mass to which the experiment is sensitive is given by the hardware energy threshold.

Since the improved discrimination does not affect the sensitivity in the relevant mass range ($\lesssim 5$ GeV/c^2), the question can be raised if the additional light

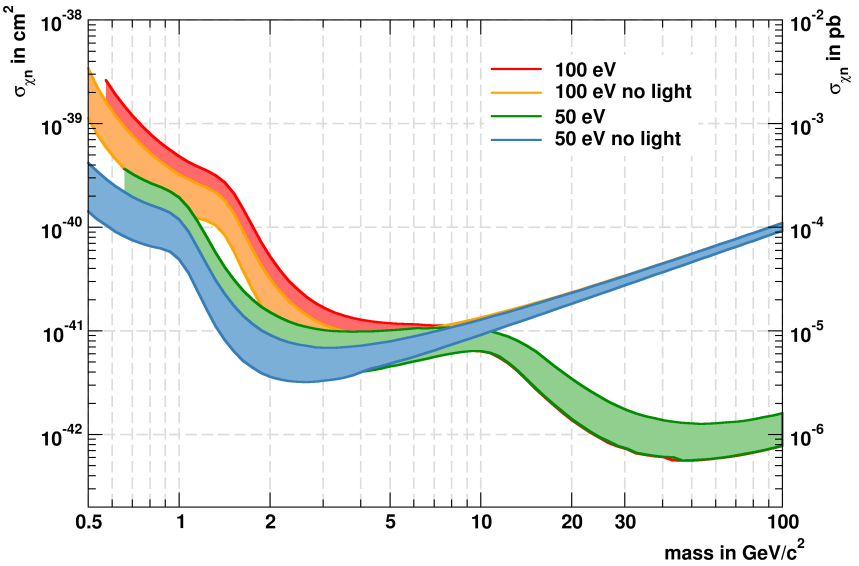

Figure 5.29: Results of the simplified Monte Carlo model comparing the different choices for the acceptance region for to different energy thresholds.

signal is needed at all. To study this, the limits obtained with and without a cut on the light yield are compared for two different energy thresholds (see Fig. 5.29). At low masses, omitting the light signal has almost no effect on the sensitivity. This is of course obvious, since the amount of light detected at the energies relevant for this mass range ($\mathcal{O}(100\,\mathrm{eV})$) is very low. Assuming that 1-5 % of the total energy are detected as light, this means only $\mathcal{O}(1)$ photons are detected for e^-/γ -events and even less for nuclear recoils. This makes it almost impossible to discriminate events based on different light yields.

The fact that the light signal loses its importance for low mass dark matter searches means that alternative target materials which do not scintillate or are poor scintillators might become interesting again. One could for example focus on materials with especially light nuclei to extend the sensitivity to even lower masses, nuclei with high spin like ^{19}F to investigate spin-dependent couplings, materials with better phonon properties like sapphire which was used in the early stages of CRESST or more radio-pure materials to achieve a lower background. Also, this would remove the need for a light detector, which would reduce cost and complexity of the detector modules. On the other hand, the light signal is still valuable at higher energies as it helps in understanding the different types of background events and their possible origin, so it might still be worthwhile to include the light signal.

Another scenario which is interesting to study, is what would happen if for some reason the background would be worse than in run 33. This is shown in Fig. 5.30, where the sensitivity of TUM40 in run 33 (with a threshold of

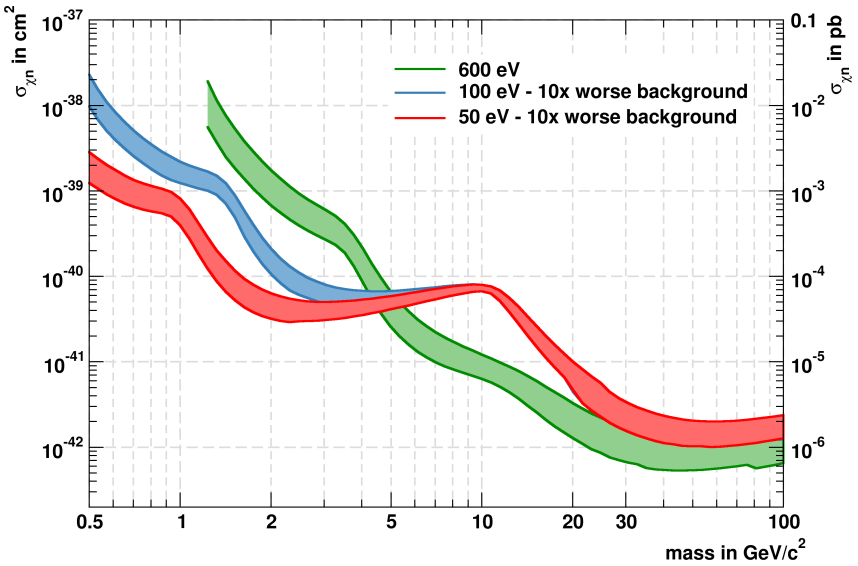

Figure 5.30: Results of the simplified Monte Carlo model comparing the current background level and energy threshold to an increased background level but lower energy thresholds.

605 keV) is compared to the sensitivity expected for a 10 times higher background, but with thresholds of 100 eV or 50 eV respectively. It shows, that the sensitivity between 5 and 20 GeV/c^2 decreases strongly, while it remains practically unaffected at higher masses and even improves at lower masses due to the lower threshold. So even if the background of the detectors installed in run 34 would turn out to be higher than the one of TUM40 in run 33, one can still expect some improvements at low masses.

5.6.3 Conclusions

The studies presented here show again that a low energy threshold and a low background level are the most important parameters to achieve a high sensitivity for light dark matter particles. Improvements in the light channel are only relevant for higher masses (above $\sim$ 10 GeV/c^2). It could even be shown that omitting the light signal altogether does not affect the sensitivity below 10 GeV/c^2. This could lead to new approaches in the design of future detectors which are optimized for low masses.

A more detailed study investigating the sensitivity of planned upgrades to the experiment are published in [113]. Although it uses slightly different assumptions for some of the parameters and a more sophisticated method, the results and conclusions are in general agreement.

Chapter 6

Conclusions and Outlook

This work describes the analysis of data obtained during run 33 of the CRESST experiment. The main goal of this run has been to clarify the nature of the excess events observed in the previous run 32. Since it has been pointed out that the excess events might be connected to backgrounds originating from α-decays close to the surfaces facing the detectors, three different module designs have been developed which enable to identify and reject these backgrounds. Analysis of the data obtained with these detectors shows no significant excess of events above the known e^-/γ -background. This leads to the conclusion that the excess observed in run 32 is most likely connected to the surface related α-backgrounds and invalidates the dark matter interpretation of the excess. There is, however, a hint of a neutron background which at first glance seems compatible with previous runs of the experiment. The lack of Monte Carlo simulations for the setup used in run 33 prevents a detailed investigation, which will be an important task for the near future.

The unprecedented radiopurity of detector TUM40, which features an absorber crystal grown at TU Munich, together with the low energy thresholds for nuclear recoils achievable with CRESST detectors (below 1 keV) spurred interest in performing a low threshold analysis searching specifically for light dark matter particles. In previous runs, only data with energies above $\sim 10\,\mathrm{keV}$, where it is possible to discriminate e^-/γ -background from nuclear recoils based on the different light yields, have been analyzed. Analyzing data down to the trigger threshold, where the discrimination power becomes very limited due to the small amount of light produced, introduces new challenges.

One of them is that some of the selection criteria rejecting unphysical events remove a larger fraction of valid events at lower energies compared to higher energies. This energy dependent acceptance has to be modeled and taken into account when data are compared with the expectation from a potential signal. A method based on artificially generated pulses obtained by superim-

posing template pulses and randomly triggered baseline data is successfully established in this work.

Another challenge are events originating from the small carrier crystals used to connect the TES to the actual absorber crystal. These events usually have a slightly different pulse shape (depending on the geometry of carrier and absorber), which may cause these events to be reconstructed at lower energies and thus to be shifted to the acceptance region for dark matter candidates. The established methods to identify these events have been developed at higher energies and are based e.g. on the different rise times of the pulses. At low energies these methods fail to distinguish between the two classes of events. In this work a random forest classifier is used to separate carrier and absorber events. The classifier has multiple input parameters which are sensitive to the different pulse shapes and is trained using artificially generated carrier and absorber events. It is shown that this method leads to a higher acceptance at energies close to the energy threshold which results in superior limits on the dark matter-nucleon cross section at low dark matter masses. In the upcoming run 34, the TES will be evaporated directly onto the absorber crystals. This eliminates the carrier crystal and thus the need to identify carrier events.

Finally, since the discrimination between e^-/γ -background and nuclear recoils breaks down at low energies it is imperative to understand the origin of the e^-/γ -background at these low energies. In the crystals grown at TU Munich, several γ-lines are observed which could be linked to electron capture decays of cosmogenically activated isotopes of tungsten by determining the energies and relative intensities of the lines as well as the half-lives of the respective decays. Since these half-lives are rather long ($\mathcal{O}(100)$ days), greater care has to be taken to avoid exposure of the raw materials and finished crystals to cosmic rays, e.g. by storing them underground whenever possible. For the future, a more detailed understanding of low energy backgrounds will be needed to guide the development of detectors optimized for light dark matter searches and also to improve the data analysis by enabling the use of maximum likelihood techniques which are essential in the case of a possible discovery.

Since no reliable background model exists yet, it was only possible to set limits on the spin-independent dark matter-nucleon cross section. The results obtained with different data sets and different detectors extend the parameter space covered by direct dark matter searches to masses below $1\,\mathrm{GeV}/c^2$. In this mass range, already limited exposures of a few 10 kg days are sufficient to attain competitive sensitivity with a low threshold analysis. This finding changes the future strategy of the CRESST experiment which is now focusing on light dark matter by improving the performance of the detectors (e.g. lowering the energy threshold) instead of increasing the total target mass. To help guide

the design of future CRESST detectors a series of Monte Carlo studies with a simplified data model are performed to study the influence of several detector parameters on the achievable sensitivity to light dark matter particles. These studies conclude that the most important parameters for the sensitivity at low masses are a low energy threshold and a low background level, whereas the light signal has no influence on the sensitivity for masses below $10\,\mathrm{GeV}/c^2$ and could in principle be ignored.

For the upcoming run 34, the dimensions of the detectors will be reduced, lowering the mass of the detectors by a factor of ~ 10 from $\sim 300\,\mathrm{g}$ to $\sim 25\,\mathrm{g}$ with the goal of achieving energy thresholds of 100 eV or lower. Also, new procedures have been developed to remove radioactive impurities like uranium or thorium from the raw materials used to grow the absorber crystals and first crystals where these methods have been applied will be installed. With 10 such modules to be installed with a total mass of 250 g, it is expected to significantly improve the sensitivity to dark matter particles with masses of $\lesssim 1\,\mathrm{GeV}/c^2$.

Bibliography

[1] J. H. Oort, "The force exerted by the stellar system in the direction perpendicular to the galactic plane and some related problems," *Bulletin of the Astronomical Institutes of the Netherlands* **6** (1932) 249.

[2] F. Zwicky, "Die Rotverschiebung von extragalaktischen Nebeln," *Helvetica Physica Acta* **6** (1933) 110–127.

[3] V. C. Rubin and W. K. Ford, Jr., "Rotation of the Andromeda Nebula from a Spectroscopic Survey of Emission Regions," *The Astrophysical Journal* **159** (1970) 379.

[4] T. S. van Albada, J. N. Bahcall, K. Begeman, and R. Sancisi, "Distribution of dark matter in the spiral galaxy NGC 3198," *The Astrophysical Journal* **295** (1985) 305–313.

[5] E. Regener, "Der Energiestrom der Ultrastrahlung," *Zeitschrift für Physik* **80** no. 9-10, (1933) 666–669.

[6] R. A. Alpher and R. Herman, "Evolution of the Universe," *Nature* **162** (1948) 774–775.

[7] A. A. Penzias and R. W. Wilson, "A Measurement of Excess Antenna Temperature at 4080 Mc/s.," *The Astrophysical Journal* **142** (1965) 419–421.

[8] M. Bucher, "Physics of the cosmic microwave background anisotropy," *International Journal of Modern Physics D* **24** no. 02, (2015) 1530004, `arXiv:1501.04288`.

[9] **Planck** Collaboration, P. A. R. Ade *et al.*, "Planck 2015 results. XIII. Cosmological parameters," *Astronomy & Astrophysics* **594** (2016) A13, `arXiv:1502.01589`.

[10] **Planck** Collaboration, R. Adam *et al.*, "Planck 2015 results. I. Overview of products and scientific results," *Astronomy & Astrophysics* **594** (2016) A1, `arXiv:1502.01582`.

[11] W. Hu and S. Dodelson, "Cosmic Microwave Background Anisotropies," *Annual Review of Astronomy and Astrophysics* **40** no. 1, (2002) 171–216, arXiv:astro-ph/0110414.

[12] V. Springel *et al.*, "Simulations of the formation, evolution and clustering of galaxies and quasars," *Nature* **435** (2005) 629–636, arXiv:astro-ph/0504097.

[13] A. A. Klypin, S. Trujillo-Gomez, and J. Primack, "Dark Matter Halos in the Standard Cosmological Model: Results from the Bolshoi Simulation," *The Astrophysical Journal* **740** (2011) 102, arXiv:1002.3660.

[14] M. Vogelsberger *et al.*, "Properties of galaxies reproduced by a hydrodynamic simulation," *Nature* **509** (2014) 177–182, arXiv:1405.1418.

[15] D. G. York *et al.*, "The Sloan Digital Sky Survey: Technical Summary," *The Astronomical Journal* **120** (2000) 1579–1587, arXiv:astro-ph/0006396.

[16] P. McDonald *et al.*, "The Lyα Forest Power Spectrum from the Sloan Digital Sky Survey," *The Astrophysical Journal Supplement Series* **163** (2006) 80–109, arXiv:astro-ph/0405013.

[17] A. G. Riess *et al.*, "Observational Evidence from Supernovae for an Accelerating Universe and a Cosmological Constant," *The Astronomical Journal* **116** (1998) 1009–1038, arXiv:astro-ph/9805201.

[18] S. Perlmutter *et al.*, "Measurements of Ω and Λ from 42 High-Redshift Supernovae," *The Astrophysical Journal* **517** (1999) 565–586, arXiv:astro-ph/9812133.

[19] K. Petraki and R. R. Volkas, "Review of Asymmetric Dark Matter," *International Journal of Modern Physics A* **28** (2013) 30028, arXiv:1305.4939 [hep-ph].

[20] R. Catena and P. Ullio, "A novel determination of the local dark matter density," *Journal of Cosmology and Astroparticle Physics* **8** (2010) 4, arXiv:0907.0018.

[21] J. I. Read, "The local dark matter density," *Journal of Physics G Nuclear Physics* **41** no. 6, (2014) 063101, arXiv:1404.1938.

[22] R. H. Helm, "Inelastic and Elastic Scattering of 187-Mev Electrons from Selected Even-Even Nuclei," *Physical Review* **104** no. 5, (1956) 1466–1475.

[23] F. Giuliani and T. A. Girard, "Model-independent limits from spin-dependent WIMP dark matter experiments," *Physical Review D* **71** no. 12, (2005) 123503.

[24] J. Lewin and P. Smith, "Review of mathematics, numerical factors, and corrections for dark matter experiments based on elastic nuclear recoil," *Astroparticle Physics* **6** no. 1, (1996) 87 – 112.

[25] M. C. Smith *et al.*, "The RAVE survey: constraining the local Galactic escape speed," *Monthly Notices of the Royal Astronomical Society* **379** (2007) 755–772, arXiv:astro-ph/0611671.

[26] T. Piffl *et al.*, "The RAVE survey: the Galactic escape speed and the mass of the Milky Way," *Astronomy & Astrophysics* **562** (2014) A91, arXiv:1309.4293 [astro-ph.GA].

[27] A. K. Drukier, K. Freese, and D. N. Spergel, "Detecting cold dark-matter candidates," *Physical Review D* **33** (1986) 3495–3508.

[28] D. N. Spergel, "Motion of the Earth and the detection of weakly interacting massive particles," *Physical Review D* **37** (1988) 1353–1355.

[29] F. Mayet *et al.*, "A review of the discovery reach of directional Dark Matter detection ," *Physics Reports* **627** (2016) 1 – 49. A review of the discovery reach of directional Dark Matter detection.

[30] **XMASS** Collaboration, K. Abe *et al.*, "XMASS detector," *Nuclear Instruments and Methods in Physics Research A* **716** (2013) 78 – 85.

[31] **DEAP** Collaboration, M. G. Boulay *et al.*, "DEAP-3600 Dark Matter Search at SNOLAB," *Journal of Physics Conference Series* **375** no. 1, (2012) 012027, arXiv:1203.0604 [astro-ph.IM].

[32] **DEAP/CLEAN** Collaboration, R. Hennings-Yeomans *et al.*, "Direct Detection of Dark Matter with MiniCLEAN," *Journal of Physics Conference Series* **315** no. 1, (2011) 012010.

[33] **XENON100** Collaboration, E. Aprile *et al.*, "The XENON100 dark matter experiment," *Astroparticle Physics* **35** (2012) 573–590, arXiv:1107.2155 [astro-ph.IM].

[34] **LUX** Collaboration, D. S. Akerib *et al.*, "The Large Underground Xenon (LUX) experiment," *Nuclear Instruments and Methods in Physics Research A* **704** (2013) 111–126, arXiv:1211.3788 [physics.ins-det].

[35] **PandaX** Collaboration, G. et al., "PandaX: a liquid xenon dark matter experiment at CJPL," *Science China Physics, Mechanics & Astronomy* **57** no. 8, (2014) 1476—1494.

[36] **DarkSide** Collaboration, T. Alexander *et al.*, "DarkSide search for dark matter," *Journal of Instrumentation* **8** (2013) C1021.

[37] **EDELWEISS** Collaboration, E. Armengaud *et al.*, "First results of the EDELWEISS-II WIMP search using Ge cryogenic detectors with interleaved electrodes," *Physics Letters B* **687** (2010) 294–298, arXiv:0912.0805 [astro-ph.CO].

[38] **CDMS** Collaboration, Z. Ahmed *et al.*, "Dark Matter Search Results from the CDMS II Experiment," *Science* **327** (2010) 1619–, arXiv:0912.3592.

[39] **SuperCDMS Collaboration** Collaboration, R. Agnese *et al.*, "Search for Low-Mass Weakly Interacting Massive Particles Using Voltage-Assisted Calorimetric Ionization Detection in the SuperCDMS Experiment," *Physical Review Letters* **112** no. 4, (2014) 041302, arXiv:1309.3259 [physics.ins-det].

[40] B. Neganov and V. Trofimov *Otkrytia i Izobretenia* **146** (1985) 215.

[41] P. N. Luke, "Voltage-assisted calorimetric ionization detector," *Journal of Applied Physics* **64** (1988) 6858–6860.

[42] C. Isaila *et al.*, "Low-temperature light detectors: Neganov-Luke amplification and calibration," *Physics Letters B* **716** (2012) 160–164, arXiv:1106.0167 [physics.ins-det].

[43] **DAMIC** Collaboration, J. Barreto *et al.*, "Direct search for low mass dark matter particles with CCDs," *Physics Letters B* **711** no. 3-4, (2012) 264 – 269.

[44] **DAMA** Collaboration, R. Bernabei *et al.*, "Final model independent result of DAMA/LIBRA-phase1," *European Physical Journal C* **73** (2013) 2648, arXiv:1308.5109.

[45] **KIMS** Collaboration, H. S. Lee *et al.*, "Search for low-mass dark matter with CsI(Tl) crystal detectors," *Physical Review D* **90** no. 5, (2014) 052006.

[46] **DM-Ice** Collaboration, J. Cherwinka *et al.*, "First data from DM-Ice17," *Physical Review D* **90** no. 9, (2014) 092005, `arXiv:1401.4804 [astro-ph.IM]`.

[47] **CoGeNT** Collaboration, C. E. Aalseth *et al.*, "CoGeNT: A search for low-mass dark matter using p-type point contact germanium detectors," *Physical Review D* **88** no. 1, (2013) 012002.

[48] **CoGeNT** Collaboration, C. E. Aalseth *et al.*, "Search for An Annual Modulation in Three Years of CoGeNT Dark Matter Detector Data," `arXiv:1401.3295 [astro-ph.CO]`.

[49] J. H. Davis, C. McCabe, and C. Bœhm, "Quantifying the evidence for dark matter in CoGeNT data," *Journal of Cosmology and Astroparticle Physics* **8** (2014) 14, `arXiv:1405.0495 [hep-ph]`.

[50] **DAMA** Collaboration, R. Bernabei *et al.*, "First results from DAMA/LIBRA and the combined results with DAMA/NaI," *The European Physical Journal C* **56** no. 3, (2008) 333–355.

[51] C. Savage, G. Gelmini, P. Gondolo, and K. Freese, "Compatibility of DAMA/LIBRA dark matter detection with other searches," *Journal of Cosmology and Astroparticle Physics* **4** (2009) 10, `arXiv:0808.3607`.

[52] **CDMS** Collaboration, R. Agnese *et al.*, "Silicon Detector Dark Matter Results from the Final Exposure of CDMS II," *Physical Review Letters* **111** no. 25, (2013) 251301.

[53] **CRESST** Collaboration, G. Angloher *et al.*, "Results from 730 kg days of the CRESST-II Dark Matter search," *The European Physical Journal C* **72** no. 4, (2012) .

[54] **LUX** Collaboration, D. S. Akerib *et al.*, "Improved Limits on Scattering of Weakly Interacting Massive Particles from Reanalysis of 2013 LUX Data," *Physical Review Letters* **116** no. 16, (2016) 161301.

[55] **PandaX-II** Collaboration, A. Tan *et al.*, "Dark Matter Results from First 98.7 Days of Data from the PandaX-II Experiment," *Physical Review Letters* **117** no. 12, (2016) 121303.

[56] **XENON100** Collaboration, E. Aprile *et al.*, "Dark Matter Results from 225 Live Days of XENON100 Data," *Physical Review Letters* **109** no. 18, (2012) 181301.

[57] **DarkSide** Collaboration, P. Agnes *et al.*, "First results from the DarkSide-50 dark matter experiment at Laboratori Nazionali del Gran Sasso," *Physics Letters B* **743** (2015) 456 – 466.

[58] **EDELWEISS** Collaboration, E. Armengaud *et al.*, "Final results of the EDELWEISS-II WIMP search using a 4-kg array of cryogenic germanium detectors with interleaved electrodes," *Physics Letters B* **702** no. 5, (2011) 329 – 335.

[59] **SuperCDMS** Collaboration, R. Agnese *et al.*, "Search for Low-Mass Weakly Interacting Massive Particles with SuperCDMS," *Physical Review Letters* **112** no. 24, (2014) 241302.

[60] A. Brown, S. Henry, H. Kraus, and C. McCabe, "Extending the CRESST-II commissioning run limits to lower masses," *Physical Review D* **85** no. 2, (2012) 021301.

[61] A. Gütlein *et al.*, "Impact of coherent neutrino nucleus scattering on direct dark matter searches based on CaWO4 crystals ," *Astroparticle Physics* **69** (2015) 44 – 49.

[62] **LUX** Collaboration, D. S. Akerib *et al.*, "First Results from the LUX Dark Matter Experiment at the Sanford Underground Research Facility," *Physical Review Letters* **112** no. 9, (2014) 091303.

[63] **SuperCDMS** Collaboration, R. Agnese *et al.*, "New Results from the Search for Low-Mass Weakly Interacting Massive Particles with the CDMS Low Ionization Threshold Experiment," *Physical Review Letters* **116** no. 7, (2016) 071301.

[64] **EDELWEISS** Collaboration, E. Armengaud *et al.*, "Search for low-mass WIMPs with EDELWEISS-II heat-and-ionization detectors," *Physical Review D* **86** no. 5, (2012) 051701.

[65] **CRESST** Collaboration, G. Angloher *et al.*, "Results on light dark matter particles with a low-threshold CRESST-II detector," *European Physical Journal C* **76** no. 25, (2016) , `arXiv:1509.01515 [astro-ph.CO]`.

[66] **CRESST** Collaboration, G. Angloher *et al.*, "Results on low mass WIMPs using an upgraded CRESST-II detector," *The European Physical Journal C* **74** no. 12, (2014) .

[67] M. Moszyński *et al.*, "Characterization of $CaWO_4$ scintillator at room and liquid nitrogen temperatures," *Nuclear Instruments and Methods in Physics Research A* **553** (2005) 578–591.

[68] V. B. Mikhailik, H. Kraus, S. Henry, and A. J. B. Tolhurst, "Scintillation studies of $CaWO_4$ in the millikelvin temperature range," *Physical Review B* **75** no. 18, (2007) 184308.

[69] M. v. Sivers *et al.*, "Low-temperature scintillation properties of $CaWO_4$ crystals for rare-event searches," *Journal of Applied Physics* **118** no. 16, (2015) .

[70] S. Roth, *The Potential of Neganov-Luke Amplified Cryogenic Light Detectors and the Scintillation-Light Quenching Mechanism in CaWO4 Single Crystals in the Context of the Dark Matter Search Experiment CRESST-II.* Ph.D. Thesis, Technische Universität München, 2013.

[71] M. Kiefer, *Improving the light channel of the CRESST-II-dark matter detectors.* Ph.D. Thesis, Technische Universität München, 2012.

[72] S. Bandler *et al.*, "Performance of TES X-ray Microcalorimeters with a Novel Absorber Design," *Journal of Low Temperature Physics* **151** no. 1-2, (2008) 400–405.

[73] J. M. Schmaler, *The CRESST Dark Matter Search - New Analysis Methods and Recent Results.* Ph.D. Thesis, Technische Universität München, 2010.

[74] J. M. Carmona *et al.*, "Neutron background at the Canfranc underground laboratory and its contribution to the IGEX-DM dark matter experiment," *Astroparticle Physics* **21** (2004) 523–533, `hep-ex/0403009`.

[75] S. Agostinelli *et al.*, "Geant4 – a simulation toolkit," *Nuclear Instruments and Methods in Physics Research A* **506** no. 3, (2003) 250 – 303.

[76] S. M. Scholl, *Neutron Background Simulation for the CRESST-II Experiment.* Ph.D. Thesis, 2011.

[77] J. F. Ziegler, M. D. Ziegler, and J. P. Biersack, "SRIM - The stopping and range of ions in matter (2010)," *Nuclear Instruments and Methods in Physics Research B* **268** (2010) 1818–1823.

[78] M. Kuźniak, M. Boulay, and T. Pollmann, "Surface roughness interpretation of 730 kg days CRESST-II results ," *Astroparticle Physics* **36** no. 1, (2012) 77 – 82.

[79] **CRESST** Collaboration, R. Strauss *et al.*, "A detector module with highly efficient surface-alpha event rejection operated in CRESST-II Phase 2," *The European Physical Journal C* **75** no. 8, (2015) .

[80] R. F. Lang, *Search for dark matter with the CRESST experiment.* Ph.D. Thesis, Technische Universität München, 2008.

[81] R. McGowan, *Data Analysis and Results of the Upgraded CRESST Dark Matter Search.* Ph.D. Thesis, University of Oxford, 2008.

[82] S. E. Pfister, *Suche nach Dunkler Materie mit dem CRESST-II-Experiment.* Ph.D. thesis, Technische Universität München, 2010.

[83] A. J. Zöller, *Artificial Neural Network Based Pulse-Shape Analysis for Cryogenic Detectors Operated in CRESST-II.* Ph.D. Thesis, Technische Universität München, 2016.

[84] F. Reindl, *Exploring Light Dark Matter With CRESST-II Low-Threshold Detectors.* Ph.D. Thesis, Technische Universität München, in preparation.

[85] The HDF Group, "Hierarchical data format version 5," 2000-2010. `http://www.hdfgroup.org/HDF5`.

[86] F. Alted *et al.*, "PyTables: Hierarchical datasets in Python," 2002–. `http://www.pytables.org/`.

[87] J. Kiefer, "Sequential minimax search for a maximum," *Proceedings of the American Mathematical Society* **4** (1953) 502–506.

[88] M. Avriel and D. J. Wilde, "Optimality proof for the symmetric Fibonacci search technique," *The Fibonacci Quarterly. Official Organ of the Fibonacci Association* **4** (1966) 265–269.

[89] **CRESST** Collaboration, M. Kiefer *et al.*, "In-situ study of light production and transport in phonon/light detector modules for dark

matter search," *Nuclear Instruments and Methods in Physics Research Section A* **821** (2016) 116 – 121.

[90] S. Yousefi and L. Lucchese, "A wavelet-based pulse shape discrimination method for simultaneous beta and gamma spectroscopy," *Nuclear Instruments and Methods in Physics Research A* **599** no. 1, (2009) 66 – 73.

[91] C. S. Burrus, R. A. Gopinath, and H. Guo, *Introduction to wavelets and wavelet transforms : a primer*. Prentice Hall, Upper Saddle River, N.J., 1998.

[92] F. Wasilewski, "PyWavelets," 2006-2010. `http://http://www.pybytes.com/pywavelets`.

[93] B. S. Clarke, E. Fokoué, and H. H. Zhang, *Principles and theory for data mining and machine learning*. Springer, Dordrecht; New York, 2009.

[94] F. Pedregosa *et al.*, "Scikit-learn: Machine learning in Python," *Journal of Machine Learning Research* **12** (2011) 2825–2830.

[95] **CRESST** Collaboration, R. Strauss *et al.*, "Energy-dependent light quenching in $CaWO_4$ crystals at mK temperatures," *European Physical Journal C* **74** (2014) 2957, `arXiv:1401.3332 [astro-ph.IM]`.

[96] S. Yellin, "Finding an upper limit in the presence of an unknown background," *Physical Review D* **66** no. 3, (2002) 032005, `arXiv:physics/0203002`.

[97] S. Yellin, "Extending the optimum interval method," `arXiv:0709.2701`.

[98] **CRESST** Collaboration, G. Angloher *et al.*, "Limits on Momentum-Dependent Asymmetric Dark Matter with CRESST-II," *Physical Review Letters* **117** no. 2, (2016) 021303.

[99] S. Yellin, "Some ways of combining optimum interval upper limits," `arXiv:1105.2928 [physics.data-an]`.

[100] **CRESST** Collaboration, G. Angloher *et al.*, "Limits on WIMP dark matter using sapphire cryogenic detectors," *Astroparticle Physics* **18** no. 1, (2002) 43 – 55.

[101] **CRESST** Collaboration, G. Angloher *et al.*, "Commissioning run of the CRESST-II dark matter search," *Astroparticle Physics* **31** no. 4, (2009) 270 – 276.

[102] **CRESST** Collaboration, R. Strauss *et al.*, "Beta/gamma and alpha backgrounds in CRESST-II phase 2," *Journal of Cosmology and Astroparticle Physics* **2015** no. 06, (2015) 030.

[103] W. Bambynek *et al.*, "Orbital electron capture by the nucleus," *Review of Modern Physics* **49** no. 1, (1977) 77–221.

[104] R. B. Firestone, C. M. Baglin, and S. Chu, *Table of isotopes*. No. Bd. 4. Wiley, 1999.

[105] A. L. Fitzpatrick, W. Haxton, E. Katz, N. Lubbers, and Y. Xu, "The effective field theory of dark matter direct detection," *Journal of Cosmology and Astroparticle Physics* **2013** no. 02, (2013) 004, arXiv:1203.3542.

[106] R. Catena, "Prospects for direct detection of dark matter in an effective theory approach," *Journal of Cosmology and Astroparticle Physics* **2014** no. 07, (2014) 055, arXiv:1406.0524.

[107] J. Fan, M. Reece, and L.-T. Wang, "Non-relativistic effective theory of dark matter direct detection," *Journal of Cosmology and Astroparticle Physics* **2010** no. 11, (2010) 042, arXiv:1008.1591.

[108] S. Chang, A. Pierce, and N. Weiner, "Momentum dependent dark matter scattering," *Journal of Cosmology and Astroparticle Physics* **2010** no. 01, (2010) 006, arXiv:0908.3192.

[109] B. Feldstein, A. L. Fitzpatrick, and E. Katz, "Form factor dark matter," *Journal of Cosmology and Astroparticle Physics* **2010** no. 01, (2010) 020, arXiv:0908.2991.

[110] A. C. Vincent, P. Scott, and A. Serenelli, "Possible Indication of Momentum-Dependent Asymmetric Dark Matter in the Sun," *Physical Review Letters* **114** no. 8, (2015) 081302.

[111] A. C. Vincent, A. Serenelli, and P. Scott, "Generalised form factor dark matter in the Sun," *Journal of Cosmology and Astroparticle Physics* **2015** no. 08, (2015) 040, arXiv:1504.04378.

[112] **CRESST** Collaboration, R. Strauss *et al.*, "The CRESST-III low-mass WIMP detector," *Journal of Physics: Conference Series* **718** no. 4, (2016) 042048.

[113] **CRESST** Collaboration, G. Angloher *et al.*, "Probing low WIMP masses with the next generation of CRESST detector," arXiv:1503.08065 [astro-ph.IM].

Danksagung

An dieser Stelle möchte ich die Gelegenheit nutzen mich bei all jenen zu Bedanken, die zum Entstehen dieser Arbeit beigetragen haben.

Zunächst gilt mein Dank Prof. Josef Jochum für die Möglichkeit die Arbeit an seinem Lehrstuhl anzufertigen sowie für die Unterstützung und das entgegengebrachte Vertrauen. Danke auch an Prof. Tobias Lachenmaier für das Interesse an meiner Arbeit und die vielen hilfreichen Kommentare und Anregungen.

Ein besonderer Dank geht an Dr. Franz Pröbst, der mit seinem Detailwissen über CRESST stets all meine Fragen zum Experiment und zur Datenanalyse beantwortet hat.

Danke auch an alle aktuellen und ehemaligen Mitgliedern der CRESST Kollaboration die zum Gelingen des Experiments beigetragen haben. Insbesondere an diejenigen die an den Vorbereitungen und Einbau für Run 33 beteiligt waren und durch ihre unermüdliche Arbeit bei Schichten und Reparatureinsätzen das Experiment am laufen gehalten haben.

Besonders möchte ich mich bei der Analysegruppe (Franz, Florian, Andi, Achim, ...) für die fruchtbare Zusammenarbeit bedanken.

For their support during my shifts at Gran Sasso I would like to especially thank Karo and Marco as well as the entire d'Archivio family for making my stays in Italy pleasant, even during cold an rainy winter months.

Darüber hinaus bedanke ich mich bei allen mit denen ich während meiner Zeit als Doktorand am PIT zusammenarbeiten durfte für die angenehme Arbeitsatmosphäre, zahlreiche Diskussionen und die ein oder andere Anregung für meine Arbeit. Speziell bei allen CRESSTlern (Marcel, Stephan, Gerhard, Klemens, Christof, Igor, Martin, Jurek) für die Unterstützung bei Fragen zum Experiment, gemeinsame Reisen zu Kollaborationstreffen, etc. und hilfreichen Tipps für die Schichten am Gran Sasso. Besonderer Dank auch an Roland für die Hilfe bei Rechnerproblemen aller Art.

Am Ende gilt mein großer Dank meiner Frau und meinen beiden Kindern, die es immer wieder geduldig ertragen haben wenn der Papa mal wieder unterwegs war sowie meinen Eltern und Schwiegereltern für ihre Unterstützung insbesondere bei der Kinderbetreuung.